

Reorganisation ~~The organisation~~ of subglacial drainage processes during ~~rapid melting~~ ~~the demise~~ of the Fennoscandian Ice Sheet ~~Finnish Lake District Ice-Lobe~~

Adam J. Hepburn^{1,2*}, Christine F. Dow¹, Antti Ojala³, Joni Mäkinen³, Elina Ahokangas³, Jussi Hovikoski⁴, Jukka-Pekka Palmu⁴, and Kari Kajuutti³

¹Department of Geography and Environmental Management, University of Waterloo, Waterloo, ON, Canada

²European Space Astronomy Centre, European Space Agency, Madrid, Spain

³Department of Geography and Geology, University of Turku, Turku, Finland

⁴Geological Survey of Finland, Espoo, Finland

Correspondence: Adam J. Hepburn, now at Aberystwyth University, Aberystwyth, Wales, UK (adam.hepburn@aber.ac.uk)

Abstract. Unknown basal characteristics limit our ability to simulate the subglacial hydrology of rapidly thinning contemporary ice sheets. Subglacial water is typically conceptualised as being routed through either distributed, inefficient, and ~~high-pressure~~ ~~high pressure~~ systems, or channelised, efficient, and ~~low-pressure~~ ~~lower pressure~~ systems, transitioning between the two as a function of discharge. ~~Understanding the spatiotemporal transition in drainage modes is critical to modelling future~~

5 ~~ice mass loss.~~ Sediment-based landforms generated beneath Pleistocene ice sheets, together with detailed digital elevation models, offer a valuable means of ~~parameterising and testing models of subglacial hydrology~~ ~~testing basal hydrology models~~, ~~which describe the flow and dynamics of water in the subglacial system~~. However, previous work using ~~geomorphology to inform modelling~~ ~~geomorphological techniques together with models of subglacial hydrology~~ has concentrated on landforms relating to channelised drainage (e.g., eskers) while using inherently channelised models, ~~which are~~ unable to capture transi-

10 tions in drainage state. Landscapes relating to the distributed drainage system, and the hypothesised transitional zone of drainage between distributed and channelised drainage modes have therefore been largely ignored. To address this, we use the Glacier Drainage System model (GlaDS), ~~a 2D finite element model capable of capturing the transition between distributed and channelised drainage, to explore the genesis of~~ ~~to compare modelling output against predictions regarding the genesis conditions associated with~~ ‘murtoos’, a distinctive triangular landform found ~~in murtoo fields~~ throughout Finland and Sweden.

15 Murtoos are hypothesised to form 40–60 km from the former Fennoscandian ~~ice~~ ~~Ice Sheet~~ margin at the onset of channelised drainage ~~in a ‘semi-distributed’ system, in small cavities~~ where water pressure is ~~at equal to~~ or exceeds ice overburden pressure. Concentrating within a specific ice lobe of the former Fennoscandian Ice Sheet and ~~parameterised~~ using digital elevation models with a simulated former ice surface geometry, we ~~carried out a range of sensitivity testing to explore murtoo genesis and drainage transitions beneath the palaeo-ice sheet. Our modelling supports forced GlaDS with transient surface melt and~~ explored the sensitivity of our model outcomes to parameter decisions such as the system conductivity and bed topography. Our model outputs support many of the predictions for murtoo origin, including the location of water ~~pressures~~ ~~pressure~~ equal to ice overburden, the onset of channelised drainage, ~~the transition in drainage modes~~, and the predicted ~~water depths in terrain~~

surrounding murtoo fields cavity size. Modelled channels also closely match the general spacing, direction and complexity of eskers and mapped meltwater routes. assemblages of features related to subglacial drainage in ‘meltwater routes’. Further, 25 these conclusions are largely robust to a range of parameter decisions. Our results demonstrate that examining palaeo basal topography alongside subglacial hydrology model outputs holds promise for the mutually beneficial analyses of palaeo and contemporary ice sheets to assess the controls of hydrology on ice dynamics and subglacial landform evolution.

1 Introduction

Surface melt delivered

30 Climatic warming is promoting more widespread and prolonged surface melting on both the Greenland and Antarctic Ice Sheets (van den Broeke et al., 2023). This surface meltwater is routed to the bed of glaciers and ice through crevasses and moulins where it is supplemented by meltwater generated at the base of the ice through geothermal heat or friction (Davison et al., 2019). Meltwater delivered to the bed of ice sheets exerts a strong but, but complex and non-linear control on ice flow and mass loss (Schoof, 2010; Meierbachtol et al., 2013; Nienow et al., 2017; Davison et al., 2019; Wallis et al., 2023) 35 . At (Schoof, 2010; Wallis et al., 2023). In spring, at the onset of the melt-season, summer ice velocity speed-ups of melt season, individual glaciers in Greenland and the Antarctic Peninsula have been observed to accelerate by between 10–300% relative to winter averages have been observed extending 10s their winter velocity, with this signal extending tens of kilometres inland from marine (Sole et al., 2011; Joughin et al., 2008) and terrestrially terminating (Bartholomew et al., 2012) portions of the Greenland (Sole et al., 2013; Moon et al., 2014) and Antarctic ice sheets (Wallis et al., 2023; Tuckett et al., 2019). The 40 (Joughin et al., 2008; Bartholomew et al., 2012; Sole et al., 2011, 2013; Moon et al., 2014; Tuckett et al., 2019; Wallis et al., 2023) . Such speedups result in enhanced mass loss into the ocean from increased run-off and iceberg calving, contributing to an increased rate of sea-level rise.

The changing configuration of the basal hydrological system beneath ice sheets throughout the melt season is primarily responsible for modulating the velocity response of glaciers to melt and is typically conceptualised as as existing in 45 either i) response of ice flow to meltwater input (Schoof, 2010). In the winter, when meltwater production is limited, low volumes of water flow through an inefficient, highly-pressurised, distributed state in which water is transmitted through system consisting of thin films (Weertman, 1972), linked-cavities (Kamb, 1987), or as Darcian flow through a porous medium (Boulton and Jones, 1979); or ii) an efficient, channelised system in which water is routed through Nye channels eroded down into the underlying substrate (Nye, 1972) or Röthlisberger channels (R-Channels, Röthlisberger, 1972) and Hooke channels 50 (Hooke, 1989) formed within the ice itself. Below a critical threshold, increased discharge close to the ice margin (e.g., at the onset of a melt season) raises water pressure and lowers the . However, at the onset of the melt season, sudden, high-volume meltwater inputs can quickly overwhelm such a distributed system, raising water pressure over large areas of the glacier bed. Where water pressure is equal to or exceeds the pressure of ice overburden, the overlying ice is hydraulically 55 lifted, reducing the frictional resistance to ice flow motion and enhancing velocity (Schoof, 2010). However, beyond this critical threshold, sustained a critical discharge threshold (Schoof, 2010) sustained periods of high discharge and turbulent

flow leads to water flow promote channelisation, with wall-melt and channelisation (Hooke, 1989). This can lower the effective pressure, and subglacial erosion, forming Nye channels into the underlying substrate (Nye, 1972) or Röthlisberger channels (R-Channels, Röthlisberger, 1972) and Hooke channels (Hooke, 1989) within overlying ice. In the channelised system low water pressure promotes steep pressure gradients which divert water flow away from the distributed system towards channels, 60 lowering water pressure and frictional resistance to flow over wide areas of the bed, dampening the velocity response to meltwater input as water is increasingly routed through the efficient system (Iken and Bindschadler, 1986; Iverson et al., 1999; Schoof, 2005). The transition between inefficient and efficient modes of drainage throughout the melt season has important implications for ice sheet dynamics in a warming climate (see Greenwood et al., 2016; Nienow et al., 2017; Davison et al., 2019, for detailed reviews) 65 (Iken and Bindschadler, 1986; Iverson et al., 1999; Schoof, 2005). Within days velocity may slow below previous levels (Vijay et al., 2021) even as meltwater volume increases through the subsequent melt season.

An accurate representation of basal hydrology in models is, and in particular the transition between distributed and channelised drainage modes, is therefore critical in efforts to predict the rate and timing of polar ice sheet mass loss (Nienow et al., 2017). Models of basal hydrology, including those capable of resolving the transition between distributed and channelised drainage, have been widely used to investigate subglacial drainage beneath contemporary ice sheets (e.g., Schoof, 2005, 2010; Banwell et al., 2013; 70 (e.g., Schoof, 2005, 2010; Banwell et al., 2013; Werder et al., 2013; Flowers, 2018; Indrigo et al., 2021; Dow et al., 2022). However, despite recent work in both one and two-way coupling of these basal-hydrology models to ice flow models (e.g., Cook et al., 2019, 2020, 2022; Ehrenfeucht et al., 2023), detailed treatment of basal hydrology is not yet widely integrated into ice sheet system models and predicting the rate and timing of glacial mass loss remains difficult (Dow, 2023). The In part, this difficulty arises because the response of ice flow to future melt depends on not only the volume, timing and duration 75 of melt, but also, critically, on the bed characteristics including basal topography, underlying geology, and the hydraulic properties of the subsurface material (Werder et al., 2013). Yet (Chu, 2014). However, beneath contemporary ice sheets our knowledge of basal topography is limited to spatial resolutions in the order of 10^2 m (e.g., Morlighem et al., 2017, 2020) and direct observations of hydraulic connectivity are sparse, especially at the ice sheet scale (Greenwood et al., 2016). Boreholes and instrumentation placed within and beneath ice are one means of direct observation of hydraulic properties 80 (e.g., Hubbard et al., 1995; Mair et al., 2003; Meierbach et al., 2013; Doyle et al., 2018, 2022), however, these are difficult to implement and impractical to use beyond a handful of sites per field campaign. Instead, much of our insight into subglacial hydrology has come from indirect proxies for drainage efficiency including proglacial discharge (e.g., Willis et al., 1996; Cowton et al., 2016), geophysical investigation (e.g., Chu et al., 2016; Killingbeck et al., 2020), and ice surface velocity time-series analysis (e.g., Mair et al., 2017), from which the influence of channelised drainage has been inferred extending up to 50 km inland of the Greenland Ice Sheet (GrIS) 85 margin (Sole et al., 2013; Chandler et al., 2013, 2021). Without a strong control on the bed characteristics beneath In numerical models, given the absence of more detailed information, such characteristics and the processes which they govern are often reduced to parameterisations, or simplifications, of what is likely a more complex reality (e.g., Schoof, 2010; Werder et al., 2013; Flowers, 2016). In order to faithfully model the basal hydrology of contemporary ice sheets, estimating and defining an appropriate set of basal parameters remains a fundamental challenge to the accurate representation and reliably bound their future mass loss, it

90 is important that we are to utilise all available sources of data to evaluate the efficacy of basal hydrology in ice sheet models
(Dow et al., 2020; Doyle et al., 2022; Hager et al., 2022; McArthur et al., 2023).

To this end, without overlying ice-cover, fluvioglacial landforms deposited beneath

Detailed geomorphological mapping across Europe and North America has revealed a complex record of glaciofluvial landforms (e.g., Figure 1B–E), which preserve information about the basal hydrology of Pleistocene ice sheets may provide crucial information for the parameterisation of basal hydrological models during periods of rapid ice loss (e.g., Clark and Walder, 1994; Cofaigh et al., 1996; Rampton, 2000; Utting et al., 2009; Storrar and Livingstone, 2017; Lewington et al., 2019; Kirkham et al., 2022). Indeed, across both Europe and North America, eskers, tunnel valleys, and meltwater routes are nearly ubiquitous in many places (e.g., Brennand, 2000; Storrar et al., 2014; Storrar and Livingstone, 2017; Lewington et al., 2019; Kirkham et al., 2022). The during their retreat since the last glacial maximum (e.g., Clark and Walder, 1994; Cofaigh, 1996; Rampton, 2000; Utting et al., 2009; Storrar and Livingstone, 2017; Lewington et al., 2019; Kirkham et al., 2022). Comparing the spatial distribution, hypothesised genesis, and geomorphology of these glaciofluvial landforms against the predictions of basal hydrology models may provide a crucial test of basal hydrology model ability not possible beneath contemporary ice sheets. However, this glaciofluvial landform record is a complex and likely time-integrated record dominated by evidence of channelised drainage, including eskers (e.g., Figure 1D), and tunnel valleys (e.g., Brennand, 2000; Storrar et al., 2014; Storrar and Livingstone, 2017; Lewington et al., 2019; Kirkham et al., 2022). By comparison, the distributed drainage system is less commonly described in landform records (Greenwood et al., 2016), although drumlin and ribbed formation likely represents drumlins and ribbed moraine formations are thought to represent flow instabilities associated with the high effective water pressures within a distributed system (Fowler, 2010; Fowler and Chapwanya, 2014; Stokes et al., 2013). Pleistocene eskers are often (Chapwanya et al., 2011; Fowler, 2010; Fowler and Chapwanya, 2014; Stokes et al., 2013). Further, the ubiquity and scale of the channelised drainage record—Pleistocene eskers may be continuously traceable over tens to hundreds of kilometres long (Storrar and Livingstone, 2017) and although (Storrar and Livingstone, 2017)—is largely without comparison in the contemporary record and similarly large channelised systems have only been described in Antarctica (Dow et al., 2022), the ubiquity and scale of channelised drainage in the palaeo record is beyond the scale of channelised drainage typically described beneath the contemporary isolated regions of the Antarctic (Dow et al., 2022). This scale mismatch, a paucity of information about distributed drainage, and the time-integrated nature of the palaeo record (Cofaigh, 1996; Greenwood et al., 2016), presents a challenge when seeking to evaluate the ability of current models to resolve the basal hydrology of palaeo ice sheets. This, together with uncertainty surrounding their formation (Cofaigh, 1996; Greenwood et al., 2016), has largely limited the 115 use of eskers to ice-flow direction indicators in empirical ice sheet reconstructions.

Work that has combined geomorphology with basal hydrology modelling has typically done so while making As a result, existing work using basal hydrology models in the palaeo setting has largely concentrated on channelised drainage, either over large areas of former ice sheet beds, or on the process of esker/tunnel valley formation at the individual landform scale, neglecting processes associated with distributed drainage and the transition between drainage modes. To investigate channelised 120 drainage, previous work has made simplifying assumptions about the pressure water exists at, water pressure, either prescribing a fixed water pressure at or near overburden everywhere (e.g., Livingstone et al., 2013a, b, 2015; Karlsson and Dahl-Jensen, 2015; Shackleton et al., 2015). Although these assumptions are thought to hold over interannual scales, these models are inherently channelised and are pressure everywhere resulting in inherently channelised models (e.g., Livingstone et al., 2013a, b, 2015; Karlsson and Dahl-Jensen, 2015; Shackleton et al., 2015) or assuming channels form where water pressure is equal to ice overburden pressure (e.g., Boulton et al., 2007a, b, 2009).

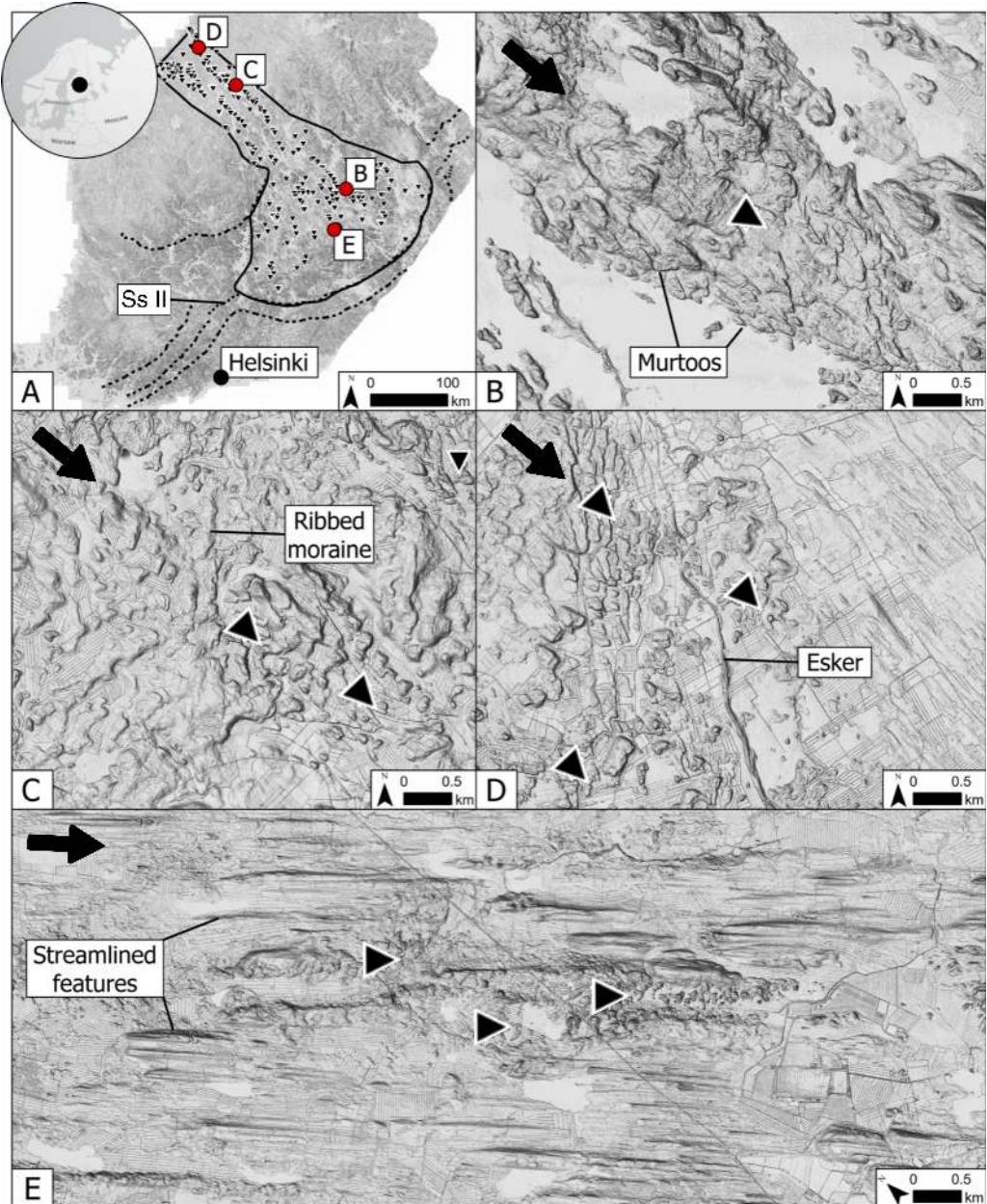


Figure 1. The study area. **A)** The extent of the GlaDS model domain (solid line) in the Finnish Lake District Ice Lobe (FLDIL) and the Salpausselkä (dashed line). Salpausselkä II (Ss II) marks the 12 cal. ka ice extent. Murtoo fields identified by Ahokangas et al. (2021) within the FLDIL are shown as inverted triangles. **B)** A murtoo field. Adjacent to the murtoos, a large esker is visible in the lake. **C)** Murtoo fields amongst ribbed moraines in the north of the FLDIL. **D)** An abrupt downstream transition from murtoo fields to a large esker. Additional murtoo fields are found directly adjacent to the esker. **E)** Three murtoo fields amongst streamlined terrain within at the centre of the FLDIL. All panels show a multi-directional oblique weighted hillshade based on 2 m LiDAR data (see Ahokangas et al., 2021, for details). In panels B-E, black arrows in the upper left corner of each panel indicate the approximate ice flow direction and the inverted triangles are aligned with the orientation of murtoos fields.

125 . These models are unable to capture dynamic changes between distributed and channelised drainage (Banwell et al., 2013)
126 . To date, no work has explored the potential for palaeo-beds to provide meaningful information regarding basal hydrological
127 processes operating, instead they are intended to represent long-term, interannual, 'steady-state' conditions (Banwell et al., 2013)
128 applicable over millennial timescales—extremely relevant timescales when investigating large, time-transgressive features such
129 as eskers and tunnel valleys (Clark and Walder, 1994; Clark et al., 2000; Mäkinen, 2003; Kirkham et al., 2022), which lack a
130 discrete age-control but were likely formed over millennia.

135 More complex, 1D process-mechanism models have also been used to investigate esker genesis (e.g., Beaud et al., 2018; Hewitt and Crey
136 , however, these idealised models also typically lack a distributed component. Further, without including a representation of any
137 specific bed topography or ice geometry, these 1D numerical process-mechanism models are difficult to compare directly to
138 mapped geomorphology. Hewitt (2011) did include modelled drainage mode transitions by describing a continuum formulation
139 of the distributed system coupled to a single channel which was allowed to evolve as a function of discharge. The length of the
140 channel and its influence on the surrounding idealised glacial bed was used to determine channel length and spacing scaling
141 relationships, finding good agreement with channel spacing predicted by Boulton et al. (2009) beneath the Fennoscandian Ice
142 Sheet (FIS). However, in representing a single channel with fixed forcing, this work stopped short of directly comparing model
143 outputs to realistic terrain data from palaeo beds. Glaciated Pleistocene terrains may provide valuable insight into subglacial
144 hydrological processes (Greenwood et al., 2016), including those variable at the sub-annual scale and across the distributed–
145 channelised transition, despite the need to better constrain hydrological models at these scales changes in which are known to be
146 critically important in understanding contemporary ice mass loss during periods of rapid climate change (Dow, 2023). Models
147 of basal hydrology capable of resolving distributed and channelised drainage are widely used to interrogate the dynamical
148 response of contemporary glaciers to increasing melt (e.g., Werder et al., 2013; Sommers et al., 2018, 2022; Ehrenfeucht et al., 2023)
149 , yet despite the critical need to evaluate and improve these models (Dow, 2023) and the potential glaciated terrains hold for
150 doing so, no work has applied a basal hydrology model capable of resolving distributed and channelised drainage to the palaeo
151 setting.

155 In this paper, we present the first application of the Glacier Drainage System model (GlaDS Werder et al., 2013), a basal
156 hydrology model capable of resolving transition between channelised and distributed drainage in the palaeo setting. To do so,
157 we specifically focus on a recently described feature landform termed 'murtoos' (singular: murtoo Mäkinen et al., 2017; Ojala et al., 2019)
158 —low (singular: murtoo, Mäkinen et al., 2017; Ojala et al., 2019)—small (30–100 m in width/length), low relief (~5 m high)
159 features with a distinctive, broadly triangular morphology (Figure 1, Ojala et al., 2019; Ahokangas et al., 2021; Peterson Becher and Johnson,
160 . Initially morphology (See Figure 1, & Ojala et al., 2019; Ahokangas et al., 2021; Peterson Becher and Johnson, 2021; Ojala et al., 2021;
161 . Murtoos were initially identified from LiDAR data in Finland (Mäkinen et al., 2017) and Sweden (Peterson Becher et al.,
162 2017), murtoos and have since been extensively mapped throughout terrain formerly occupied by the FIS (Ojala et al., 2019; Ahokangas et al.,
163 . Murtoos are hypothesised to form beneath warm-based ice during the rapid retreat of the FIS since the Younger Dryas (12.7
164 to 11.7 cal. ka), during which large volumes of meltwater were delivered to the bed in a glacial setting similar to contemporary
165 Greenland (Ojala et al., 2019). Murtoo morphometry (Mäkinen et al., 2017; Ojala et al., 2021), their sedimentological architecture
166 (Peterson Becher and Johnson, 2021; Hovikoski et al., 2023; Mäkinen et al., 2023), and close spatial association with eskers,

160 ribbed tracts, and putative subglacial lakes (Ojala et al., 2021; Ahokangas et al., 2021; Vérité et al., 2022; Mäkinen et al., 2023) suggests that murtoo formation occurs within broad and low conduits, subject to repeated short pulses of meltwater against a backdrop of increasing water discharge throughout a melt season, at water pressures close to or exceeding ice overburden pressure, and with short sediment transport distances, such as might be found at the spatial onset of channelisation in a ‘semi-distributed’ transitional drainage system (Hovikoski et al., 2023).

165 Murtoos are therefore unique glaciofluvial landforms, and their short formation time, small size, and apparent location at the spatial onset of channelisation make murtoos potentially important components of the subglacial system. Murtoos are therefore ideal geomorphic targets against which basal hydrology models can be evaluated. Accordingly, in this paper, our aims are to model the subglacial hydrological conditions at the end of the Younger Dryas in order to:

170

- Compare the subglacial hydrological conditions proposed for murtoo genesis and their associated landforms against model outputs from GlaDS.
- Sensitivity test GlaDS across a range of possible parameter values to explore the influence of these parameters on our outcomes in order to evaluate the potential of such models to be used to interrogate palaeo-hydrological systems more broadly and in turn motivate future work in this area.

2 Study area and the significance of murtoos for basal hydrology

175 Our study area (Figure 1A) is the Finnish Lake District Ice-Lobe (FLDIL) province within southern Finland described by Putkinen et al. (2017) and Palmu et al. (2021), the FLDIL contains a high density of murtoo fields (Figure 1A, Ahokangas et al., 2021). The FLDIL is one ice lobe amongst several which comprised the eastern margin of the Fennoscandian Ice Sheet (FIS) (Ojala et al., 2019; Ahokangas et al., 2021). ~~Regional mapping in~~ at its Younger Dryas (12.7 to 11.7 cal. ka) extent, and the FLDIL encompasses an area of \sim 57,600 km², with a main trunk upstream of a lobate expansion. The bedrock within the 180 FLDIL and the wider FIS is predominantly crystalline bedrock, dominated by Precambrian schists, gneisses, and granitoids (Lehtinen et al., 2005) with a thin Quaternary overburden (Lunkka et al., 2021). The distribution of esker systems, ice-marginal complexes, streamlined bedforms, and moraines in south-central Finland suggests that the continental ice sheet at this time likely consisted of relatively rapidly flowing ice-lobe provinces, such as the FLDIL, interspersed with passive interlobate regions (Punkari, 1980; Salonen, 1986; Punkari, 1997; Boulton et al., 2001; Lunkka et al., 2004; Johansson et al., 2005; Putkinen et al., 2017).

185 ~

The lobate portion of the FLDIL is particularly well demarcated at its distal margin by the first and second Salpausselkäs (Figure 1A)—large ice-marginal complexes, which mark the Younger Dryas extent of the FIS in the region (Donner, 2010; Lunkka et al., 2017). Our model domain is bound at its lateral margin by the younger, second Salpausselkä, which is the most recent ice-marginal feature in the region and marks the FLDIL extent at \sim 12 cal. ka (Putkinen et al., 2017). Shoreline data indicates that the second Salpausselkä terminated in a shallow water body ranging in depth from <5 m to \sim 50 m (Lunkka and Erikkilä, 2012). The high-density of drumlins, mega-scale glacial lineations (MSGL), eskers and hummocky moraines (Figure 1C–E) within the

FLDIL, their consistent orientation along a principal northwest–southeast axis, and the absence of ice-marginal features behind the second Salpausselkä suggest there was limited re-organisation of the major ice flow pathways during ice sheet retreat after ~12 cal. ka (Putkinen et al., 2017). Instead, the FIS is likely to have collapsed continuously and rapidly following the Younger Dryas (Kleman et al., 1997), retreating northwest towards Norway and gone by 9–10 cal. ka (Hughes et al., 2016; Stroeven et al., 2016; Reg 195 . The speed of the retreat, together with the complex and dense assemblage of glaciofluvial landforms (e.g., Palmu et al., 2021; Dewald et al., suggest that during deglaciation, the FIS was characterised by high and spatially extensive atmospheric-driven surface melting delivered to the bed, accompanied by calving into the Baltic Sea Basin (Greenwood et al., 2017; Patton et al., 2017; Boswell et al., 2019) . Conditions within the FLDIL, and the FIS more broadly, were likely comparable to conditions prevalent in land- or shallow-water 200 terminating portions of the Greenland Ice Sheet today (Greenwood et al., 2016; Ojala et al., 2019).

Regional mapping across Finland has demonstrated a preferential clustering of ~~murtoo fields~~ murtoos in fields (e.g., Figure 1B) along meltwater routes—integrated ~~networks of assemblages of multiple~~ landforms associated with subglacial meltwater (Dewald et al., 2022) (Lewington et al., 2020; Ahokangas et al., 2021; Dewald et al., 2022)—which are in turn concentrated in ~~more dynamic~~ faster flowing, ~~warm-based~~ sectors of the FIS including ~~ice-stream tracts, interlobate joints, and ice-stream~~ 205 ~~confluence zones~~ (Ahokangas et al., 2021; Palmu et al., 2021) the FLDIL (Ahokangas et al., 2021; Palmu et al., 2021; Dewald et al., 2022) . Murtoos are absent within more passive, ~~cold-based~~ regions of the FIS (Ahokangas et al., 2021). Topographically, ~~the murtoo~~ formation environment is ~~murtoos are~~ associated with subglacial lake basins, bedrock depressions, and the lee side of some 210 large bedrock protrusions (Ojala et al., 2021; Ahokangas et al., 2021).

~~Murtoos are absent within more passive, cold-based regions of the FIS (Ahokangas et al., 2021). In this way, murtoo~~ distribution mimics that of eskers, ribbed moraines, drumlins, and other lineated features in Finland (Palmu et al., 2021). ~~Murtoo fields are often closely associated~~ Meltwater routes containing murtoos, or ‘murtoo routes’ herein (Ahokangas et al., 2021) are often adjacent to or downstream of drumlin fields, ~~some are co-located amongst or downstream of~~ or ribbed moraines (e.g., Vérité et al., 2022, and Figure 1C), and murtoo ~~fields routes~~ may be located upstream of, and ~~appear to~~ transition into, eskers (Figure 1D Ahokangas et al., 2021). Murtoos are hypothesised to form in a transitional zone between inefficient, distributed 215 ~~drainage networks, and the efficient, channelised drainage networks (Ojala et al., 2019)~~ (Figure 1D, Ahokangas et al., 2021) . The close association of landforms relating to channelised drainage with murtoo routes may therefore ~~also~~ mark the spatial and/or temporal transition ~~to~~ from distributed to channelised drainage within a ‘semi-distributed drainage and an excess of meltwater in areas subject to repeated and brief pulses of meltwater delivered to the bed’ drainage system, formed during the 220 rapid deglaciation of the FIS (Ojala et al., 2019, 2021; Ahokangas et al., 2021; Peterson Becher and Johnson, 2021; Ojala et al., 2022; Vérité et al., 2022; Mäkinen et al., 2023). Crucially, murtoos

Within our specific FLDIL study area, murtoo distribution is representative of their distribution across the wider FIS. In the upstream trunk, murtoo fields occur amongst ribbed and hummocky moraines (Figure 1C) in two longitudinal bands, each bounded by a dense assemblage of streamlined forms. In the northeastern longitudinal bands, eskers are particularly clearly associated with murtoo routes (Figure 1D). Downstream, where the FLDIL broadens into a lobe, murtoo distribution is more fragmented with less clustering evident. Murtoos are sparse in the centre of the ice lobe, however, the area’s thin sediment cover (Figure A1) may limit the material for murtoo formation, and the high density of water bodies may act to mask existing murtoo 225

fields (Ahokangas et al., 2021). Crucially, in the FLDIL, as elsewhere, murtoo routes have a characteristic distribution, rarely and are rarely found closer than 40–60 km from the FIS-second Salpausselkä margin at ~12 cal. ka (Mäkinen et al., 2023), aligning well with the apparent limits of channelisation to within 50 km of the ice sheet margin in contemporary Greenland (Chandler et al., 2013, 2021) (Chandler et al., 2013, 2021; Dow et al., 2015).

The study site. **A**) The extent of the GlaDS model domain (solid line) in the Finnish Lake District Ice Lobe (FLDIL) and the Salpausselkäs (dashed line). Salpausselkä II (SS2) marks the 12 ice extent. Murtoo fields Ahokangas et al. (2021) within the FLDIL are shown as inverted triangles. **B**) A murtoo field visible in LiDAR data. Adjacent to the murtoos, a large esker is visible in the lake. **C**) Murtoo fields amongst ribbed moraines in the north of the FLDIL. **D**) An abrupt downstream transition from murtoo fields to a large esker. Additional murtoo fields are found directly adjacent to the esker. **E**) Three murtoo fields amongst streamlined terrain within at the centre of the FLDIL. Ice flow is from the upper left in all panels, with the exception of panel **E** in which ice flow is left to right.

Murtoo excavation and field study indicates that individual murtoos are composite landforms arranged parallel to ice flow, comprising a main body that is primarily depositional together with lateral margins and a lee-side head that are erosional features (Mäkinen et al., 2017, 2023; Hovikoski et al., 2023). Internal excavations within individual murtoos (e.g., Peterson Becher and Johnson, 2021; Mäkinen et al., 2023; Hovikoski et al., 2023) have revealed that murtoos consist of a core unit containing sorted sediments, overlain by a main body unit (referred to as Unit 2 by Mäkinen et al., 2023) that i) distally is comprised of alternating facies of heterogeneous diamicton, with strong fabrics interbedded with sorted gravelly and sandy sediment (Mäkinen et al., 2023) and ii) proximally, of is comprised of alternating sequences of glaciofluvial deposits, such as current ripples, with current ripples (formed in low discharge, lower flow regimes) giving way to transitional cross-bedding (transitional flow regimes), and antidunal sinusoidal laminations reflecting alternating lower and upper flow regimes (Peterson Becher and Johnson, 2021; Mäkinen et al., 2023; Hovikoski et al., 2023) sinusoidal lamination (formed in higher discharge, upper . The murtoo body is, in turn, overlain by a mantling deposit heavily modified by soil forming processes, but nonetheless exhibiting weakly stratified diamicton and gravel beds as well as large boulders deposited by at the ice-bed interface (Mäkinen et al., 2023). This sequence of sedimentological architecture suggest a murtoo body may form within a single melt season tracking the development of a semi-distributed drainage system. The sequence of murtoo formation is interpreted as follows (from Hovikoski et al., 2023):

1. In the first stage of murtoo formation, the at the end of meltwater pulses the sorted sediment dominated core develops following sediment deposition within a rapidly enlarging broad and shallow subglacial conduit—possibly associated with pre-existing till ridges or cavities in the lee-side of protrusions. Sediment within this core evidences at least partial ice contact and periodic deformation by ice, and is superposed over existing, meltwater route deposits (Mäkinen et al., 2023)
2. With the onset of spring melt, pulses of water deposit the murtoo body is deposited within an increasingly large conduit, promoting. As each pulse increases in discharge and then wanes they promote the deposition of sand lenses, sinusoidally stratified sand, and poorly-sorted gravel, with silt commonly draping ripple-scale features. In this phase of formation,

cobbles are the largest clast size, which places an upper limit on water depth of ~ 25 cm (Hovikoski et al., 2023). Subdivisions within this unit separated by muddy glaciofluvial deposits may relate to distinct peaks in meltwater input throughout the season (Mäkinen et al., 2023).

265 3. As the melt season continues through summer, an increasingly enlarged pond forms in response to higher discharge. In turn, the increasing grain size indicates higher water velocity and depth accompanying the development of an enlarged pond. Sediments and boulder size-distributions sediments on the upper slope appear consistent with high velocity, upper-flow-regime deposits in which water depth neared and the boulder size-distribution suggest a maximum flow space of 1 m (Hovikoski et al., 2023).

270 4. The development of this enlarged cavity/pond and subsequent water pressure drop encourages localised creep closure at the broadest part of the murtoo, evidenced by a disappearance of sorted sediment, and in some murtoos this is succeeded by compacted diamieton—indicating interbedded diamicton—indicating ice-bed recoupling (Mäkinen et al., 2023). Meanwhile, closer to the margins of the murtoo body, meltwater flow continued and forced to pass an enclosed space, is routed obliquely towards the tip, forming boulder-rich proto-channels. These deposits indicate that the ice-bed recoupling at the broadest part of the murtoo coincided with intense and increasingly erosional channelised flow at the murtoo margins.

275 5. Finally, murtoo deposition is abruptly terminated as evidenced by sudden appearance of laminated mud deposited via suspension settling in the top of the marginal channels in some murtoos (Hovikoski et al., 2023). The overall increase in meltwater and sudden decay suggests murtoo development within a single melt season or rapid reorganisation associated with autogenic changes within the and marginal channels are abandoned. The final sedimentation within these marginal channels is characterised by suspension settling and laminated muds, indicating that the depositional space (0.6–0.8 m) remained open and water filled but no longer hydraulically connected to the wider meltwater system (Hovikoski et al., 2023; Mäkinen (Ojala et al., 2022; Hovikoski et al., 2023).

280

Murtoo excavation indicates that murtoos are composite landforms arranged parallel to ice flow, comprising of a main body that is primarily depositional together with lateral margins and a lee-side head that are erosional forms. Together with murtoo mapping, this indicates that murtoos are formed subglacially amongst a network of low canals, conduits, or cavities in which water velocity is highly variable (Mäkinen et al., 2023). The interbedding of silt and clay poor sandy/gravelly diamictons with poorly sorted sediments are suggested to result from pulsed, sediment rich flows, and the limited evidence for glaciotectonic deformation suggests effective pressures close to zero (Mäkinen et al., 2023).

290 The short timescales over which murtoos are hypothesised to form, their small size, and their location at the onset of channelisation make them potentially important components of The sequence of murtoo deposits charts an overall increase in meltwater discharge throughout the melt season followed by an abrupt termination (Table 1), possibly within the same year (Hovikoski et al., 2023). Against this backdrop, the subglacial system, and ideal geomorphic targets against which models

of subglacial hydrology capable of resolving short timescales as well as the transition between distributed and channelised drainage can be evaluated. In this paper, we used the Glacier Drainage System model (Werder et al., 2013), *GlaDS* hereafter, to explore the basal hydrological conditions associated with murtoo formation beneath the FIS and to evaluate the potential for such models to be used to interrogate palaeo hydrological systems more broadly.

3 Study site

Following the Younger Dryas between 12.7 to 11.7, the eastern margin of the Fennoscandian Ice Sheet (FIS) was located behind the Salpausselkä ice-marginal complexes towards the southern coast of Finland. The mapped distribution of esker systems, interlobate eskers, ice-marginal complexes, streamlined bedforms, and moraines suggests that the continental ice sheet at this time likely consisted of rapidly flowing ice-lobe provinces interspersed with relatively passive interlobate regions (Punkari, 1980; Salonen, 1986; Punkari, 1997; Boulton et al., 2001; Lunkka et al., 2004; Johansson et al., 2005; Putkinen et al., 2017; Palmu et al., 2021). Ice-lobe provinces characteristically contain a marked concentration of streamlined morpho-lithogenetic units with a coherent orientation (Palmu et al., 2021) – features typically absent from interlobate regions (Ahokangas et al., 2021). Where ice lobes abut adjacent lobes or interlobate regions, alternating sequences of glaciofluvial deposits in the main body of murtoos suggests that the system was also subject to repeated pulses of meltwater and rapid changes in flow regime, marking the rerouting and periodic isolation of cavities within a developing, semi-distributed drainage system over a single melt season or during rapid reorganisation associated with autogenic changes within the wider meltwater system (Hovikoski et al., 2023; Mäkinen et al., 2023). The spatial distribution and sedimentological architecture of murtoos provides a testable set of predictions against which a basal hydrology model can be tested, including the location of a persistent area of high water pressure, the margins are often characterised by large eskers and interlobate glaciofluvial systems, and distally, ice lobes typically terminate in complex ice-marginal assemblages (e.g., the Salpausselkä) comprising glaciofluvial sandurs and deltas, as well as moraine ridges (Palmu et al., 2021). evolution of discharge through the year, and the onset of channelised drainage.

Our study site (Figure 1A) is focused on the Finnish Lake District Ice Lobe province described by Putkinen et al. (2017) and Palmu et al. (2021). Encompassing an area of ~57,600

3 Methods

To model the basal hydrology of the FLDIL, and compare this to the murtoo developmental stages, we used the Ice-sheet and Sea-Level System Model (ISSM, Larour et al., 2012, Revision 27448) (ISSM, Larour et al., 2012, Revision 27448), and the implementation of the *GlaDS* model (Werder et al., 2013) contained therein. We first generated an input ice geometry by depressing a contemporary reanalysis temperature and precipitation dataset to approximate conditions ~12 cal. ka. Then, using *GlaDS* parameterised by this input ice geometry and a modified digital elevation model (DEM) of the region (see Section 3.1.1), we explored the evolution of basal hydrology in beneath the FLDIL through time. A detailed description is provided below and model parameter values are given in Table 2.

325 **3.1 Model description**

The GlaDS model (described in full in Werder et al., 2013) is a 2D finite element model [building upon earlier work \(see Schoof, 2010; Hewitt, 2011\)](#) which has been widely applied to contemporary ice sheets in Greenland (e.g., Dow et al., 2018a; Cook et al., 2020, 2022; Ehrenfeucht et al., 2023) and Antarctica (e.g., Dow et al., 2018b, 2020; Indrigo et al., 2021; Dow et al., 2022; McArthur et al., 2023) as well as glaciers in Svalbard (e.g., Scholzen et al., 2021). The GlaDS model [includes distributed flow along linked cavities](#) 330 [operates on an unstructured mesh and includes a model of distributed flow through linked cavities \(Hewitt, 2011\)](#) represented by a continuous [sheet of ‘sheet’ of water with](#) variable thickness at mesh elements, and channelised [flow through flow—describing uniform, semi-circular](#) Röthlisberger channels (R-channels) that [form along mesh edges of a prescribed unstructured mesh are allowed to change diameter—along element edges \(Schoof, 2010\)](#). A key advantage of GlaDS lies in its ability to capture the growth and restriction of these channels entirely due to drainage dynamics, without requiring a predetermined drainage system 335 (Dow et al., 2020). Water flux, q_s , through the distributed system is driven by the hydraulic potential gradient, $\nabla\phi$, along with the sheet conductivity, k_s

$$q_s = -k_s h^\alpha |\nabla\phi|^\beta \nabla\phi, \quad (1)$$

where the first (α) and second (β) sheet flow exponents describe fully turbulent flow in the Darcy-Weishbach law, and h is the sheet thickness. [The sheet thickness evolves through time given by](#)

$$340 \quad \frac{\delta h}{\delta t} = w - v, \quad (2)$$

for functions w and v which describe the cavity opening and closing rate respectively (Walder, 1986; Kamb, 1987). Basal sliding opens cavities at a rate given by the basal sliding speed, U_b acting over basal bumps with a height, h_r through

$$w(h) = \begin{cases} U_b (h_r - h) / l_r & \text{if } h < h_r \\ 0 & \text{otherwise} \end{cases} \quad (3)$$

where l_r is the typical horizontal cavity spacing. In turn, viscous ice deformation leads to cavity closure, which is related to the 345 effective pressure, N by

$$N = \frac{h_r^2}{2h} \quad (4)$$

350 where A is the rate factor, or the rheological constant of ice, multiplied by a first order geometrical factor, and n is the Glen's flow law exponent. Sheet elements exchange water with channels ~~along element edges, and~~ the cross sectional area of ~~which these channels~~ S , ~~evolve evolves~~ through time due to the dissipation of potential energy, Π , sensible heat exchange, Ξ , and cavity closure rates due to viscous ice creep v_c

$$\frac{\partial S}{\partial t} = \frac{\Xi - \Pi}{\rho_i L} - v_c, \quad (5)$$

355 where ρ_i is the ice density and L is the latent heat of fusion. ~~Channels In GlaDS, channels~~ are able to form along all element edges ~~but only a few will reach a meaningful size (Werder et al., 2013). A key advantage of GlaDS lies in its ability to capture the growth and restriction of these channels entirely due to drainage dynamics, without requiring a predetermined drainage system (Dow et al., 2020) and channel discharge, Q_c , is always non-zero along these edges.~~ Following Werder et al. (2013), we set a threshold discharge of $Q = 1$ $Q_c = 1 \text{ m}^3 \text{ s}^{-1}$ above which an element edge is classified as a ~~channel~~ 'meaningful' channel for our subsequent analysis. Surface melt can either be routed to the bed via a series of moulin, represented as cylinders with a fixed cross sectional area, $A_m = 10 \text{ m}^2$, or delivered directly to the bed at every node. Finally, an ~~An~~ englacial void ratio term, $e_v E_w$ controls the volume of water stored in englacial aquifers to mimic the observed delay between daily maximal melt input and peak proglacial discharge (Werder et al., 2013). Finally, in the iteration used here, GlaDS is not coupled two-ways to a model of ice dynamics, and instead we prescribe an ice velocity and geometry that is not variable in response to hydrological forcing.

365 3.1.1 Boundary conditions and forcings

To model basal hydrology, GlaDS requires user inputs for ~~melt forcing~~, bed elevation, z_b and ice thickness, h ~~H~~ as well as boundary conditions and parameters (Table 2) detailed below. We anticipate that the modern ~~surface elevation-topography~~ is not representative of ~~that~~ bed elevation ~ 12 cal. ka. As ~~Therefore, as~~ the baseline boundary condition, z_b , we account for changes, particularly in terrain associated with the ~~second~~ Salpausselkä ~~ice marginal~~ ice-marginal formation, by subtracting Quaternary sediment thickness estimates (GTK, Finland, 2010) from the 25 m/pixel EU-Digital Elevation Model V1.1 (available at: <https://www.eea.europa.eu/data-and-maps/data/copernicus-land-monitoring-service-eu-dem>). Because lake bathymetry was only partially available we did not subtract this from our input DEM in the baseline model. We also did not adjust our model to account for differences in elevation due to glacial isostatic adjustment (GIA) since ~ 12 cal. ka. Available sea-level markers from Rosentau et al. (2021) and Ojala et al. (2013) suggest that uplift of ~ 80 m has occurred in the southeastern portion of our domain, and up to 200 m in the northwest since ~ 12 cal. ka. Combined with eustatic sea level rise, these differences account for a maximum of 100 m difference in elevation ~~relative to our DEM~~ and a tilting of the basin towards the southeast during glaciation, ~~which varied through time~~. Variable through time, accounting for GIA would result in a maximum increase to the

mean annual air temperature of $\sim 0.75^{\circ}\text{C}$ (based on our chosen lapse rate of $7.5^{\circ}\text{C km}^{-1}$, Section 3.1.1) across portions of our domain. To ensure the numerical stability of GlaDS the input DEM was smoothed using a low-pass filter. Finally, within steep terrain, an anisotropic mesh ($n_{\text{nodes}} \approx 19,000$) was refined based on z_b such that element edges were shortest (to a minimum edge length of 400 m) in rougher terrain and longer where terrain was flatter (to a maximum edge length of 2 km). As boundary conditions, we imposed a zero flux condition on the domain edge everywhere except at the ice terminus, where given spatial uncertainty around water depth variability in water depth (Lunkka and Erikkilä, 2012), an outlet Dirichlet condition equivalent to atmospheric pressure was prescribed in the baseline model. By enforcing zero input flux we neglect to include basal water input from beyond the model domain and we also do not account for any exchange of water between adjacent ice lobe provinces. To promote model stability, we used an adaptive timestep that was allowed to vary between one hour and ~ 90 seconds and all of our transient models were run for 10,000 days, or ~ 27 years.

An approximation for the FIS ice thickness, hH , at ~ 12 cal. ka within the FLDIL was generated using the 2D Shallow-Shelf Approximation (SSA, MacAyeal, 1989) within ISSM (Larour et al., 2012). Ice is assumed to be isothermal with a viscosity, B , equivalent to an ice temperature of -5°C (from Cuffey and Paterson, 2010, p.73; rate factor, A , listed in Table 2). In reality, ice temperature is both spatially and temporally variable, however, However, without using a more detailed thermomechanical ice model here, we follow the previous ad-hoc assumptions of Nick et al. (2013) for the GrIS Greenland Ice Sheet and Åkesson et al. (2018) for the FIS, by setting our ice temperature to -5°C . Basal motion was modelled using a viscous sliding law (Budd et al., 1979) and following Åkesson et al. (2018) we used a spatially variable basal drag coefficient, αa , proportional to bed z_b , given by:

$$\alpha a = 120 \frac{\min(\max(0, z_b + 800), 2000)}{2000}. \quad (6)$$

To reach volumetric steady state, defined for our ice sheet model as differences in ice volume between successive iterations of less than 10^{-6} km^3 , we ran the ice sheet model for 20,000 years with an adaptive timestep, allowed to vary between 1 day and 1 year. An initial estimate of ice surface elevation was given using a parabolic profile as a function of distance from the terminus, and initialisation values for velocity were calculated using a stress balance solution for this ice surface. Dirichlet conditions were imposed at the mesh edges along the boundary with zero inflow.

We used climatic forcing both for our ice sheet model and for GlaDS. The 12 cal. ka climate was estimated using a modern (1981-2010) reanalysis dataset (see Abatzoglou et al., 2018). Precipitation was kept at the contemporary monthly value, but we depressed monthly temperature by 15°C , approximately the temperature differential indicated by NGRIP $\delta^{18}\text{O}$ records (Johnsen et al., 1997). In simply depressing the climate we are neglect the complex seasonality (short, warm summers with extreme winters) that characterised the Younger Dryas cold reversal in Fennoscandia (Schenk et al., 2018; Amon et al., 2022). However in fixing our domain to the second Salpausselkä our model is representative of the end of the Younger Dryas at which time this extreme seasonality rapidly gave way to a markedly warmer climate with similar seasonality to the present day (Mangerud et al., 2023). To calculate surface mass balance efficiently in our long term ice sheet model we used a simple positive degree day (PDD) model (as in Cuzzone et al., 2019) allowed to vary about a fixed Gaussian distribution with standard

deviation, $\sigma_{PDD} = 5.5^\circ \text{C}$ around the monthly mean and a lapse rate of $7.5^\circ \text{C km}^{-1}$. However, our focus here is on the basal hydrology and we used a modified PDD scheme to estimate meltwater production for our GlaDS simulations.

It is commonly assumed that the total monthly positive degree days can be represented by a fixed Gaussian distribution with $\sigma_{PDD} \approx 5.5^\circ \text{C}$ (e.g., Braithwaite and Olesen, 1989). However, field measurements suggest that this does not hold for the [GIS](#) [Greenland Ice Sheet](#) (Wake and Marshall, 2015), particularly at temperatures $\geq -5^\circ \text{C}$. Instead, Wake and Marshall (2015) suggest monthly variability in temperature, σ_M , is more accurately described by a quadratic function:

$$\sigma_M = -0.0042T_M^2 - 0.3T_M + 2.64, \quad (7)$$

where T_M is the mean monthly temperature. This function accounts for the observation that variability in temperature decreases with increasing temperatures (Gardner et al., 2009; Marshall and Sharp, 2009; Fausto et al., 2011) due to heat buffering, which

promotes a more stable boundary layer (Wake and Marshall, 2015). We used the calculated σ_M to add Gaussian noise to a daily temperature record estimated by linearly interpolating our depressed MAT record. The number of positive degree days per month, PDD_M was taken as $PDD_M \geq -5^\circ \text{C}$. We used -5°C as our threshold (rather than the more commonly used 0°C threshold) to account for melt which may occur even for days with an average temperature of 0°C (see van den Broeke et al., 2010). Finally, we used melt rate factors $\gamma_{ice} = 17.22 \text{ mm per PDD}$ and $\gamma_{snow} = 2.65 \text{ mm per PDD}$ following Cuzzone et al. (2019) keeping these consistent between our ice sheet model and GlaDS model. Monthly melt was kept fixed annually for each run. Melt varied in absolute terms between individual simulations but the mean melt and standard distribution remained identical throughout.

Total monthly melt was then converted to yearly melt rates and routed to the bed via a series of moulin. Without detailed [ice sheet](#) surface topography and following Werder et al. (2013) we divided our domain using Voronoi tessellation [around](#) on a randomly distributed series of points. Within each Voronoi cell, acting as a ‘catchment zone’, the lowest elevation node was identified and used as the location for a moulin towards which all [other melt from all other catchment](#) nodes flow. Surface melt rate was integrated over each catchment and converted to instantaneous moulin discharge, Q_m^k .

3.1.2 Steady state and sensitivity testing

To avoid overwhelming our initial system with sudden meltwater inputs and to approximate a wintertime hydrology configuration, we first The GlaDS model has been extensively sensitivity tested for contemporary ice sheets where model results can be compared with geophysical evidence to determine the most plausible model output (e.g., Werder et al., 2013; Dow et al., 2018b, 2020, 2022). We set the parameters in our baseline model (default values listed in Table 2) following the default values in these studies which provide a reasonable approximation of contemporary ice sheet subglacial conditions. We then explored the sensitivity of our specific model outcomes to the available parameters (e.g., conductivity terms) in GlaDS throughout the range of values listed in Table 2, as well as the dependence of our results on our choice of forcing and boundary conditions (Section 4.2).

Before all model runs, we ran GlaDS to steady state with no surface melt and fixed basal meltwater input. Informed by sensitivity testing and previous work (e.g., Werder et al., 2013; Dow et al., 2018b, 2020; Indrigo et al., 2021), the values listed

in Table 2 were used as input parameters to GlaDS. To ensure but no surface melt. We did this to avoid overwhelming an unpressurised initial system with sudden surface meltwater inputs and to approximate a wintertime hydrology configuration 445 characterised by a distributed system with high water pressures. To guarantee the majority of nodes pressurised elements were pressurised at the end of our each steady state run, we used a low fixed velocity of $30\text{--}1\text{ m yr}^{-1}$ to limit the rate of cavity expansion (see Equation 3). Given uncertainty regarding the spatial variability of basal melt rates, which vary as a function of geothermal heat and frictional heating, we used a spatially and temporally constant basal water input (as in Dow 450 et al., 2018a, c, 2020; Poinar et al., 2019). Basal melt rates beneath the GrIS–Greenland Ice Sheet typically range between $1\text{--}7 \times 10^{-3}\text{ m yr}^{-1}$ (see Karlsson et al., 2021) and we used $5 \times 10^{-3}\text{ m yr}^{-1}$ for our steady state configuration and the majority of the subsequent transient runs. To test the influence of basal melt rates on our system we ran an additional low basal melt rate ($1 \times 10^{-3}\text{ m yr}^{-1}$) and high basal melt rate scenario ($7 \times 10^{-3}\text{ m yr}^{-1}$) to steady state. Here, steady state was reached once the median difference in water depth–sheet thickness between two successive steps was less than 10^{-6} m . All three basal melt scenarios reached this by 20,000 days, and nodes reached ~water pressures 90% of overburden pressure, or overburden% $\approx 90\%$ 455¹ with no channel formation.

For the default baseline transient model run, we used the end-member final configuration of our steady state run as an initialisation state with the addition of transient surface melt routed to the bed via ~ 2500 moulin, a density of 0.04 moulin per km^2 . Measured moulin density varies between 0.02 to 0.09 moulin per km^2 in Greenland (Yang and Smith, 2016). To test the sensitivity of our system to moulin density we also ran models with ~ 1000 (0.02 per km^2), ~ 4000 (0.06 per km^2), and two 460 further randomly generated configurations of the default ~ 2500 (0.04 per km^2). We also tested an additional configuration in which melt at every node was routed directly to the bed. Further sensitivity testing (parameters listed in bold in Table 2) was carried out for several poorly constrained parameters in GlaDS (listed in bold in Table 2), as well as for the basal geometry 465 and moulin density. The conductivity of both the sheet, k_s and channels, k_c are the key controls on the extent and spacing of channels, with the basal bump height, h_r , and basal velocity also important. For basal velocity, we tested values between 100–200 m yr^{-1} chosen to be comparable to GPS measurements of surface velocity across land-terminating sectors of the Greenland Ice Sheet (e.g., Tedstone et al., 2015). We tested both a temporally fixed and temporally variable velocity, with the transient velocity varying between 85% and 140% of the mean to approximate speed-ups at the onset of the melt season and winter slowdowns commonly observed in Greenland (e.g., Sole et al., 2013). Without a more detailed understanding of past 470 dynamics, ice dynamics, the magnitude of velocity was kept spatially uniform throughout.

Although the default configuration describes a terrestrial margin, we also tested the influence of a shallow body of water at the ice margin by prescribing Dirichlet conditions at the ice margin where water pressure is equivalent to that of a uniform 30 m water depth–m water depth (a simplification of the variable 5–50 m water depth from Lunkka and Erikkilä, 2012). To explore the influence of our modified topography boundary condition, we ran tests with a uniformly flat bed, one representing contemporary terrain (without Quaternary sediment thickness removed), and one with the available partial lake bathymetry removed. 475 Finally, we also explored the dependency of our results on mesh geometry, including using a coarser mesh (maximum edge

¹Borehole measurements of overwinter water pressure in the distributed drainage system have been measured at 80–90% of overburden pressure (e.g., Harper et al., 2021)

length of 5 km), a mesh not refined by elevation in any way, and a mesh in which a coarse mesh (edge length between 5–8 km) was prescribed >80 km from the ice margin and a much finer mesh (edge length \approx 300 m) was prescribed <80 km from the ice margin.

3.2 Model validation from geomorphological datasets

480 Finally, we compared the GlaDS output to ~~geomorphological evidence. We first masked model nodes falling within 40–60 km of the subglacial hydrological conditions proposed for murtoo genesis. We anticipate that our domain contains a time-integrated record of landforms formed throughout the retreat of the FIS since the end of the Younger Dryas. With a fixed domain bound at the second Salpausselkä, we are effectively representing a single time slice \sim 12 cal. ka. As such, we expect that much of the landform record will not be well-represented by our model outputs, particularly those landforms further from the ice margin.~~

485 ~~However, closer to the ice margin (within 0–50 km of the ice margin), where work in Greenland would suggest the basal hydrological system is more likely to be channelised during summer (e.g., Chandler et al., 2013), we made visual comparison of modelled channel spacing, length, and complexity against esker deposits mapped by Palmu et al. (2021).~~

490 ~~Similarly, and assuming that the mapped murtoo distribution is also representative of a time-transgressive mode of origin, we examine the performance of our model within the hypothesised range zone of murtoo formation (e.g., Ojala et al., 2019) (e.g., Ojala et al., 2019; Ahokangas et al., 2021) by specifically isolating model nodes falling within 40–60 km of our ice margin representative of the FLDIL extent \sim 12 cal. ka. We then queried these nodes according to whether they occurred within a mapped meltwater route (as mapped by Ahokangas et al., 2021); sub-dividing these routes based on the presence or absence of murtoo fields into murtoo routes (meltwater routes with murtoos) and meltwater routes (meltwater routes without murtoos). Using 500 m buffers, we approximated the lateral extent of murtoo/meltwater routes along 2D polylines representing their central long-axis from Ahokangas et al. (2021). In total, 1205–244 nodes occur in murtoo hosting meltwater routes, 951 nodes in murtoo-free meltwater routes, and 244 nodes that 1205 nodes are not associated with any meltwater routes but are between 40–60 km of the ice margin. Visual comparison was also made to esker deposits within the FLDIL mapped by Palmu et al. (2021). Ahokangas et al. (2021) mapped eskers separately to meltwater routes, including these as “channelised routes” in their dataset. However, Ahokangas et al. (2021) go on to note that many channelised routes fall within or intercept meltwater routes and likely postdate meltwater routes. Without age-control, we do not make a distinction between murtoo/meltwater routes and channelised routes here.~~

4 Results

500 In total, 30 simulations ~~were run~~ are reported on here, all of which successfully converged. In Section 4.1 we discuss our baseline test, and in Section 4.2 we report the parameter and forcing dependencies. For each model run, we examined the subglacial water pressure, expressed as a percentage of the overburden pressure (~~overburden %~~, $\overline{overburden\%}$) sheet discharge, q_s on element faces; channel discharge Q_c on element edges (~~where $Q \geq 1$~~), and water velocity, V_w .

4.1 Baseline scenario

4.1.1 Model behaviour

After an initial adjustment from steady state to transient forcing over 40–50 years, the baseline model reached a quasi-steady state configuration in which the system responded seasonally to summer meltwater input (Figure A2). Figure 3 shows the median summer and winter state (excluding the initial adjustment time) of the baseline run in terms of pressure expressed as a percentage of overburden, Q_s (Figure 3A), discharge within sheet elements, q_s (Figure 3B), water velocity, V_W (Figure 3C), and channel discharge, Q_c (Figure 3D) as well as mapped murtoo fields from Ahokangas et al. (2021). In summer, modelled channels, shown as black solid lines (Figure 3A–C) typically extend up to 40 km from the ice margin creating valleys of low overburden% (Figure 4A). Between 40 km and up to 60–70 km from the ice margin, in the transitional area between inefficient and efficient modes of drainage, overburden% approaches and exceeds 100% of overburden. Beyond 70 km from the ice margin, with zero channelisation and widespread inefficient drainage, overburden% modelled channels, overburden% is uniformly at ~80%. Towards the ice margin

Throughout the year, q_s sharply increases decreases 60 km from the margin in both summer and winter (Figure 3B). In summer, as areas of high q_s (approaching $10^{-1} \text{ m}^2 \text{ s}^{-1}$) are found between channels 30–40 km from the ice margin which we interpret as arising due to channels draw down water from surrounding areas, q_s approaches 10^{-1} between channels. In winter, with limited channel discharge, the highest sheet discharge is found within 40–60 km, q_s is lower throughout the domain, and the highest values of q_s ($\sim 1 \times 10^{-2} \text{ m}^2 \text{ s}^{-1}$ Figure 3B) are found in patchy areas within 60 km of the ice margin ($\sim 1 \times 10^{-3}$ Figure 3B). Throughout the year, V_W remains high ($\sim 1.5 \times 10^{-3} \sim 15 \times 10^{-4} \text{ m s}^{-1}$) at the ice margin. During summer, V_W in the sheet reflects the concentration of drainage into channelised systems 0–40 km from the ice margin, with velocities $\sim 8 \times 10^{-4} \text{ m s}^{-1}$ persisting up to 50 km from the ice margin. In winter, the drop in velocity away from the ice margin is sharper more pronounced, and higher water velocities ($> 5 \times 10^{-4} \text{ m s}^{-1}$) are limited to less than 50 km from the margin. Finally, Figure 3D shows Q_c with ~ 35 parallel–sub-parallel channels visible in summer, during which median discharge reaching Q_c reached a maximum of $100 \text{ m}^3 \text{ s}^{-1}$. A number of channels have an anabranching structure as well as small tributaries. In winter, a number of channels persist the winter, ~10 channels persist in the winter median system with a maximum median discharge of $3 \text{ m}^3 \text{ s}^{-1}$ (Figure 3D).

Figure 4C shows the system state during September of model year 19, arbitrarily chosen as a representative example of the model state at the end of a melt season. As in Figure 3, Beyond 100 km, upglacier of any significant surface melt inputs to the bed, only limited seasonal evolution of the hydrological system is evident (e.g., Figure 4A). Here, the system is effectively inert, with overburden% remaining $\approx 80\%$ with only small periodic perturbations in q_s , Q_c , and V_W . Closer towards the ice margin, a sub-parallel pattern of channels emerges in summer months (Figure 4C), with channels arranged perpendicular to, and extending up to ~ 50 km inland of the ice margin and comparable in structure and spacing to the location of esker deposits in the FLDIL (Figure 2 Palmu et al., 2021). Approximately 40 main channels are evident in late summer (Figure 4), evenly spaced every ~ 5 km laterally, each of which is also fed by one to two levels of anabranching lower-order tributaries. Following the initial period of adjustment to transient forcing, peak discharge for these channels is $200 \text{ m}^3 \text{ s}^{-1}$ during summer

(~June) each year with a maximum cross-sectional channel area of 42 m^2 (equivalent to a half-circle with radius, $r \approx 5 \text{ m}$). Many channels exhibit a biannual pattern of growth and decay (e.g., Figure 4B) persisting throughout the winter between two consecutive summers. Following initial channel growth after the onset of the melt season (preceded by a sharp increase in ~~overburden pressure~~^{overburden%}), Q_c ~~of~~ⁱⁿ these persistent channels ~~trends~~^{drops} towards $1 \text{ m}^3 \text{ s}^{-1}$ but does not fall below 545 the channelisation threshold before the following summer. As a result, subsequent meltwater input through these persistent channels is quickly accommodated with only a small increase in ~~overburden%~~^{overburden%} and ~~little change in~~^{q_s} (Figure 4B). An alternating spatial pattern of overwinter ~~channel~~ persistence is evident. ~~Channels in~~^{In} any given year, channels will persist through winter in either the central third of the lobe or in the centre of the FLDIL lobe persist through winters in which no channels persist nearer to the lateral margins, and vice versa the following winter, with no overwinter channels evident during 550 winters in which lateral margin channels persist overwinter remaining two thirds of the lobe (Movie A1).

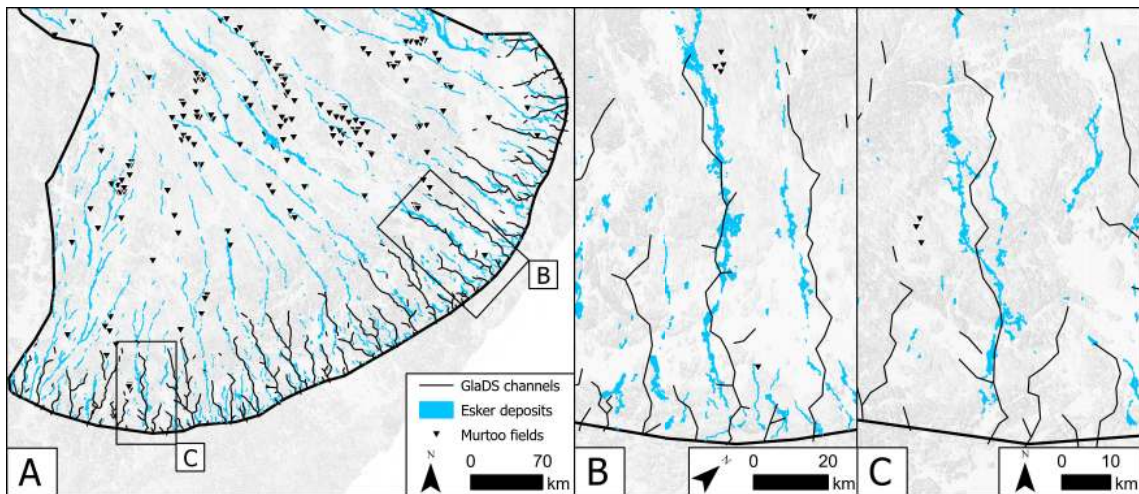


Figure 2. Modelled channel location compared to esker deposits mapped by Palmu et al. (2021) at the ice margin of the FLDIL. **A)** Modelled channels in the baseline run (black lines) across the full width of the domain compared to esker deposits (blue polygons). **B & C)** Detailed comparison of two large esker systems against model channels.

In the ice interior, at the head of modelled channels, a persistent area of ~~low effective pressure (where the overburden percentage, overburden%, approaches and exceeds 100%)~~ ~~high overburden% ≈ 100%~~ develops each melt season (Figure 3A) following the onset and migration up-glacier of surface meltwater inputs. Figure 4D–E demonstrates the seasonal evolution of two nodes in this area, each ~~associated with~~^{nearby to} channel systems. ~~Each node undergoes~~^{Both nodes undergo} a rapid 555 seasonal increase in ~~overburden pressure to~~^{overburden%} up to a maximum of approximately 120% with a more gradual decrease thereafter. At node 3,842, ~~chosen to be representative of surrounding nodes at the onset of a channel~~ (Figure 4E), this pattern repeats annually—every year the ~~decrease in overburden following an initial increase~~ ~~increase and decrease in overburden%~~ is accompanied by peaks in q_s , Q_c , and V_W and the development of channels throughout the meltwater season. However, a more complex biannual signal is evident at node 16,402 (Figure 4D), which is located $\sim 0.7 \text{ km}$ from a murtoo field

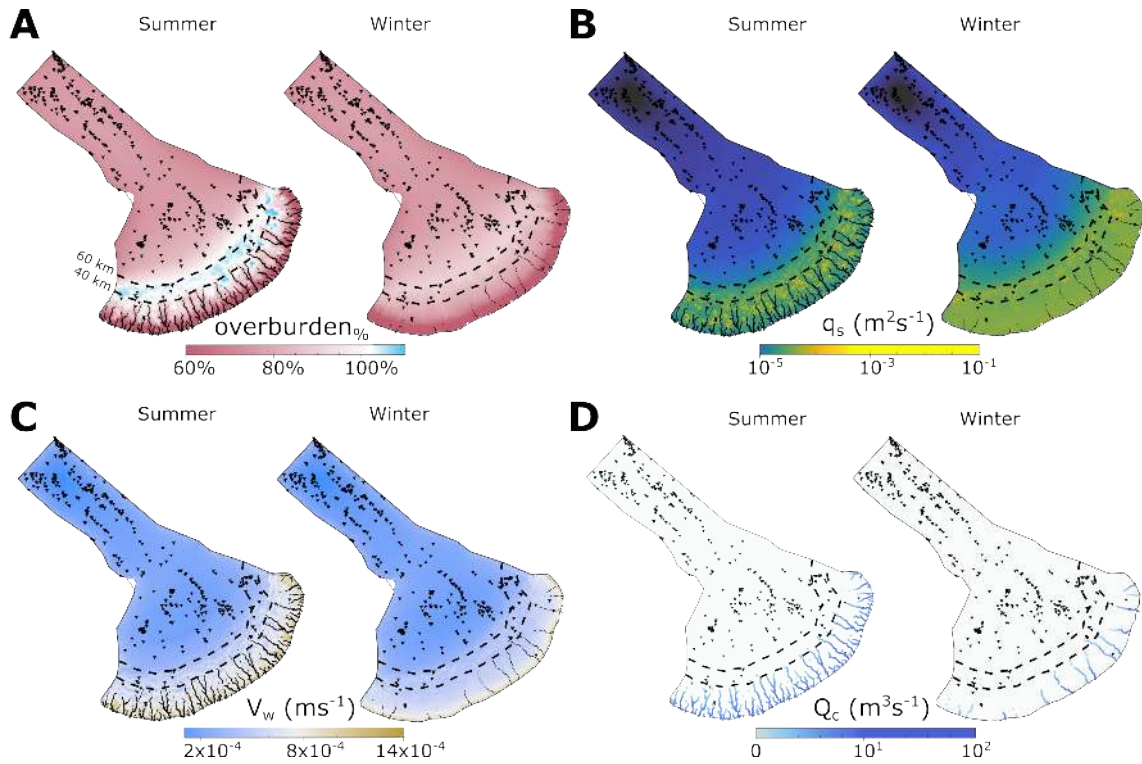


Figure 3. Median summer and winter system states in the baseline model run. **A)** Water pressure expressed as a percentage of overburden pressure, overburden%. In summer and winter, channels, shown as black solid lines (here and in panels **B** & **C**) **B)** Sheet discharge, q_s . **C)** Water velocity, V_w . **D)** Channel discharge, Q_c . For each output, we took the median from model years 5–27 disregarding the initial period of adjustment to transient forcing. Summer extends from May to September, all other points fall into winter. Note that the scales for panels **B** and **D** are logarithmic. Dashed lines in all panels indicate contours of 40 and 60 km from the ice margin. Murto fields (Ahokangas et al., 2021) are shown as inverted triangles in all plots. Channels are shown as black solid lines in panels **A–C**.

560 –between the onset of adjacent modelled channels. Here, every other year, the evolution of overburden% and Q_c follow the expected model outcomes described in Table 1. Each year, there is a sharp increase in overburden% at the start of the melt season to $\geq 100\%$, however, the subsequent drop in overburden% varies every other year. Either the overburden% spikes and then drops rapidly over 1–2 months to the winter value ($\sim 80\%$) until the following melt season, or the drop in overburden% is initially shallower before quickly dropping to an elevated pressure overburden% ($\sim 90\%$) relative to the previous winter. Years in which the drop in overburden% is more gradual are also associated with low values of lower Q_c and higher q_s . In contrast, years that have a rapid drop in overburden pressure overburden% after the melt season are associated with larger channels, with values of Q_c approaching 10^0 . Beyond 100, upglacier of any significant surface melt inputs to the bed, only limited seasonal evolution of the hydrological system is

evident (e.g., Figure 4A). Here, the system is effectively inert, remaining at $\rho_O \approx 80\%$ with only small periodic perturbations

570 in q_s , Q_c , and $V_W \cdot \text{m}^3 \text{s}^{-1}$.

Focusing

4.1.2 Hydrology in the hypothesised zone of murtoo formation

We explored behaviours potentially associated with murtoo formation by focusing on nodes 40–60 km from the ice margin, within the distance zone thought to be associated with murtoo formation at this time period (Ojala et al., 2019), we grouped

575 nodes according to whether they fall ~12 cal. ka (Ojala et al., 2019). We grouped all nodes within 40–60 km by their relation to meltwater routes mapped by Ahokangas et al. (2021). The three groups included nodes i) within the boundary of a mapped meltwater route and that route also hosts a murtoo field murtoo route (a meltwater route containing murtoos $n = 241$), ii) within the boundary of a mapped meltwater routes meltwater routes (that *does not* contain a murtoo field $n = 955$), and iii) beyond any mapped meltwater routes (all other nodes, $n = 1205$) (Figures 5 & 6). As noted in Section 3.2, group i and ii may also

580 include eskers ('channelised routes' in Ahokangas et al., 2021) as these are often coincident with meltwater routes.

Nodes that fall within a murtoo or meltwater route (Groups i, $n = 955$ & ii, $n = 244$ and iii) show strong seasonal variation and at every point throughout the year have higher overburden% overburden%, q_s , V_W , and Q_c than nodes that do not fall within a mapped murtoo/ meltwater route. The median signal of nodes within murtoo and meltwater routes is one of sharp increases at or just following the onset of the melt season, followed by a more gradual decline into winter (Figure 5). One-way

585 ANOVA analysis in which the values of overburden% overburden%, q_s , V_W , and Q_c between groups i–iii were considered without respect to time, indicates that there is a statistically significant difference in the population marginal means (or the mean within each grouping) of the three categories ($p < 0.05$ at the 95% confidence interval).

Additionally, we grouped each node observation within calendar months (Figure A32). Comparison of groups i–iii within each month—using two-way ANOVA analysis and the Tukey-Kramer HSD Test for multiple comparisons of unequal group sizes—indicate that there are significant differences ($p < 0.05$) between the population marginal means throughout the year for each of the four parameters discussed here (Tables A1–A4). In terms of overburden%, both groups of overburden%, both murtoo routes and meltwater routes are significantly higher (10–30%) than nodes outside of murtoo/ meltwater routes during every month. However, both murtoo and meltwater route groups are also significantly different from each other every month. Between January and April, overburden% overburden% is significantly higher by 1–3% in murtoo-hosting meltwater routes 595 nodes than in murtoo-free meltwater routes. Following the onset of the melt season, during June and July, overburden% is lower in group i overburden% is lower by 1–5% in murtoo route nodes than in group ii meltwater route nodes, before again returning to higher overburden% in group i overburden% (1–3%) in murtoo route nodes relative to group ii meltwater nodes between August–December. In terms of q_s (Table A2) both groups of murtoo and meltwater routes are higher than nodes beyond murtoo/ meltwater routes all year by $\sim 1 \times 10^{-5} \text{ m}^2 \text{s}^{-1}$. Between January and May there are no significant differences 600 between murtoo hosting, and murtoo-free, routes and meltwater routes. However, between June and December, q_s is significantly lower in murtoo hosting meltwater routes than in murtoo-free meltwater routes meltwater routes by $\sim 1 \times 10^{-5} \text{ m}^2 \text{s}^{-1}$. There is no significant difference between any group in terms of Q_c with the exception of between June–October (Table A3),

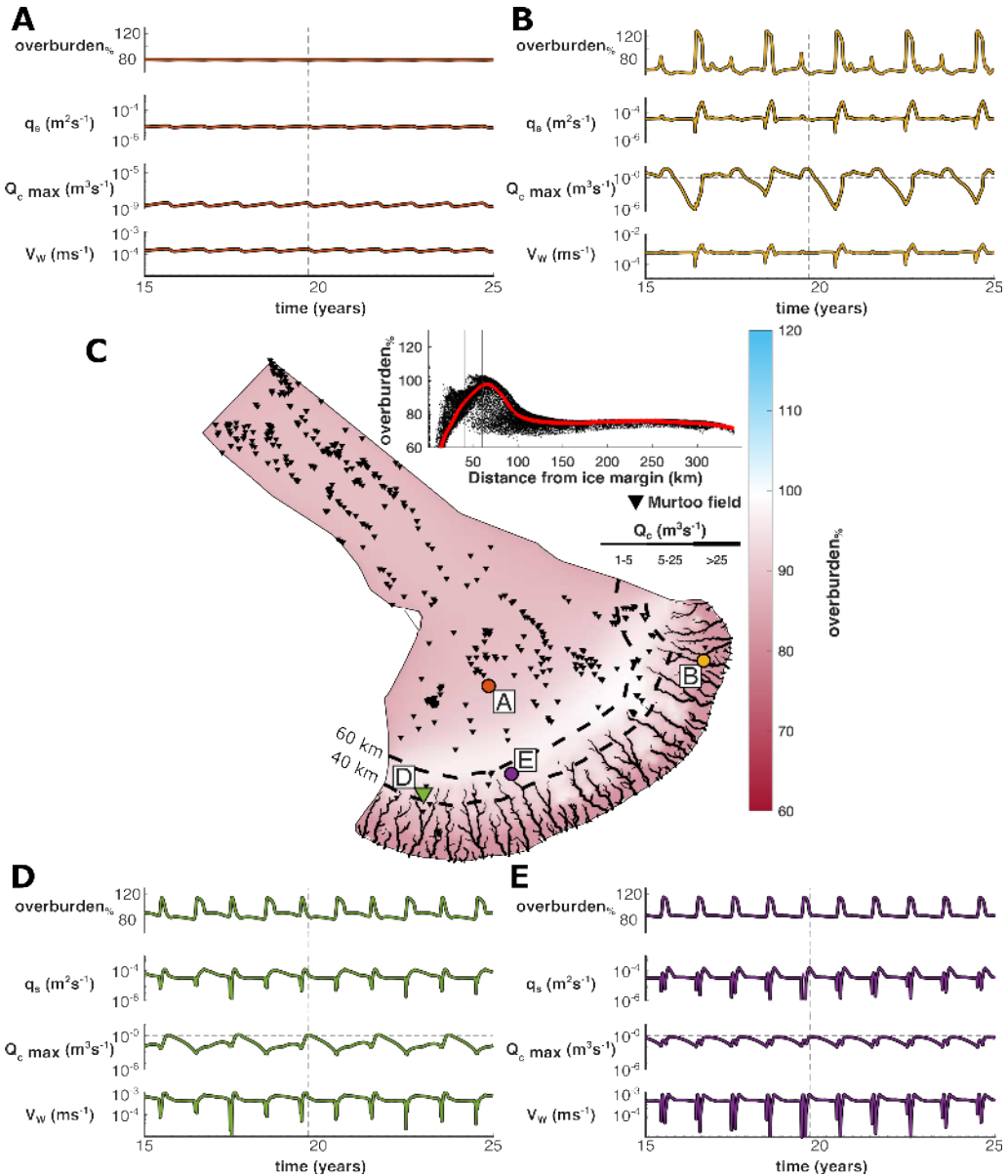


Figure 4. The evolution of water pressure as a percentage of overburden pressure (overburden% overburden%), sheet discharge (q_s), water velocity (V_W), and maximum channel discharge (Q_c $Q_{c\max}$) at four nodes during an arbitrarily chosen span over model years 15–25 in the baseline model run. **A)** Node No. 6,277 located ~120 km from the ice margin. **B)** Node No. 18,517 located ~17 km from the ice margin. **C)** Overburden at the end of the melt season in model year 19–19 (arbitrarily selected). Channels are represented as black lines, murtoos fields as inverted black triangles, and the location of panels A, B, D, and E as coloured points. Inset shows overburden at every node as a function of distance, D from the ice margin with a smoothing function shown in red and vertical lines at 40 and 60 km from the ice margin. **D)** Node No. 16,402 located 0.7 km from a murtoo field and ~45 km from the ice margin. **E)** Node No. 3,842 located ~54 km from the ice margin at the head of a channel system without an adjacent murtoo field. The time slice shown in panel C is represented as a vertical dashed line in panels A, B, D, and E. Note the logarithmic scale for q_s Q_c $Q_{c\max}$.

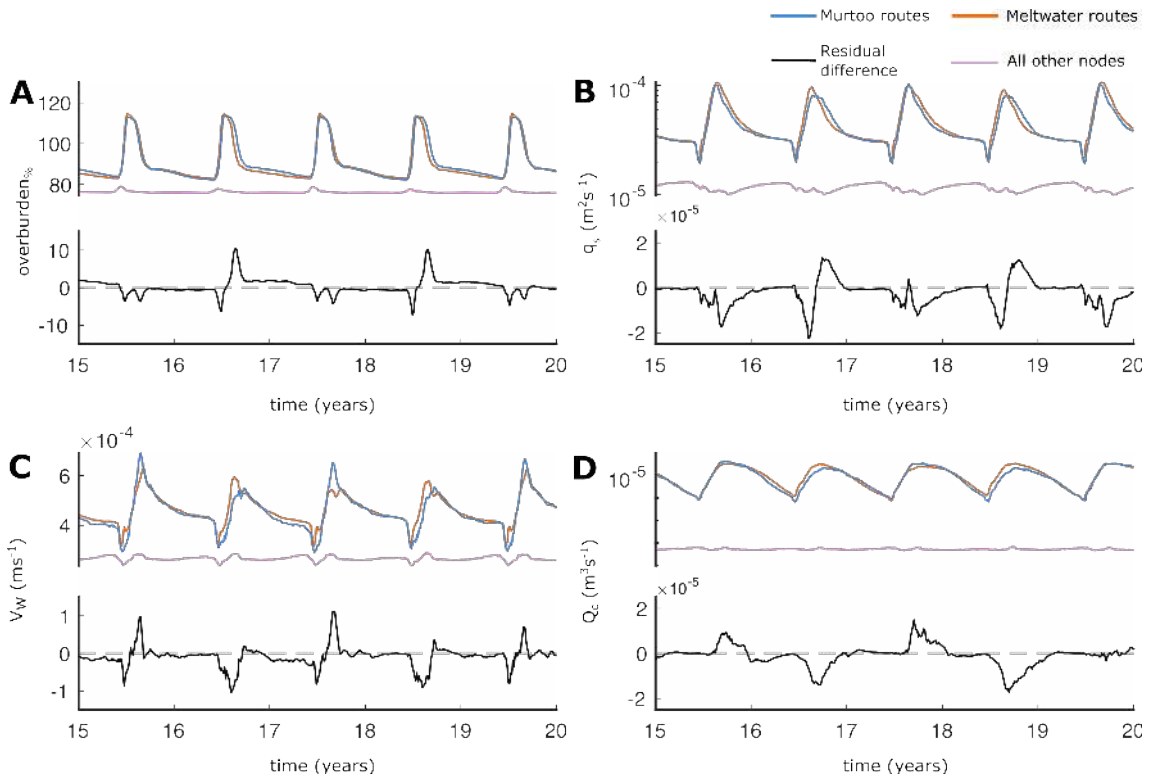


Figure 5. Median output during model years 15–20 at nodes between 40–60 km from the ice margin. In all panels, nodes ~~which fall~~ within ~~mapped~~ ~~meltwater~~ ~~routes~~ ~~that do not contain~~ ~~murtoo~~ ~~fields~~ (~~murtoo~~ ~~hosting~~) ~~routes~~ are shown in ~~orange~~ ~~blue~~, those ~~that~~ ~~which~~ fall within ~~meltwater~~ ~~routes~~ ~~which do host~~ ~~murtoos~~ (~~murtoo~~ ~~free~~ ~~without~~ ~~murtoos~~) are shown in ~~blue~~ ~~orange~~, and all other nodes are shown in ~~dashed~~ ~~purple~~. The ~~red~~ ~~black~~ line in each panel represents the residual difference between the median of murtoo ~~hosting~~ ~~meltwater~~ ~~routes~~ and ~~murtoo~~ ~~free~~ ~~meltwater~~ ~~routes~~. A positive residual indicates higher median values in murtoo ~~hosting~~ ~~meltwater~~ ~~routes~~, and vice versa for negative residual values. **A)** Water pressure expressed as a percentage of overburden, ~~overburden~~_%. **B)** Sheet discharge, q_s . **C)** Water velocity, V_w . **D)** Channel discharge, Q_c . Note panels B and D have logarithmic scales.

when ~~during~~ ~~which~~ Q_c is significantly higher ~~outside~~ ~~meltwater~~ ~~routes~~ ~~within~~ ~~murtoo~~ ~~and~~ ~~meltwater~~ ~~routes~~ ~~than~~ ~~beyond~~ by $\sim 1 \times 10^{-5} \text{ m}^3 \text{ s}^{-1}$. Finally, throughout the year, V_w is higher in ~~mapped~~ ~~murtoo~~ ~~and~~ ~~meltwater~~ ~~routes~~ ~~than~~ ~~beyond~~ them (Table A4) by $\sim 1 \times 10^{-3} \text{ m s}^{-1}$. In murtoo ~~hosting~~ ~~meltwater~~ ~~routes~~ V_w is significantly lower for each month than in murtoo free meltwater routes by $\sim 1 \times 10^{-4} \text{ m s}^{-1}$.

4.2 Sensitivity tests

The parameter sensitivity of basal drainage within GlaDS has already been extensively explored by Werder et al. (2013) and ~~others~~ (see Dow et al., 2018b, 2020, 2022; Indrigó et al., 2021; Scholzen et al., 2021) and as such we do not conduct a detailed review here. However, ~~in order to best apply the model to a palaeoglacial setting~~ because several parameters in GlaDS

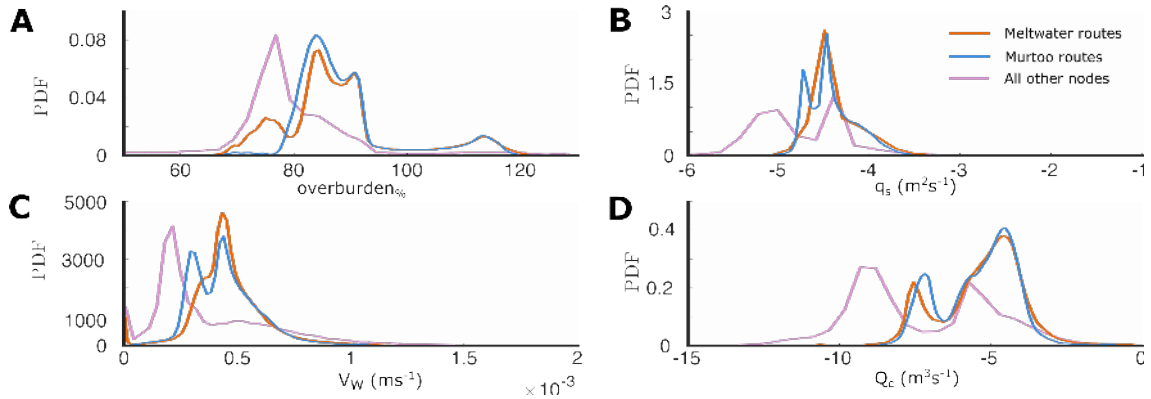


Figure 6. Probability density estimates from kernel smoothing of output parameters during all model years at nodes between 40–60 km from the ice margin. As in Figure 5, nodes ~~which that~~ fall within ~~mapped meltwater routes that do not contain murtoo fields~~ (~~Murtoo-hosting routes~~) are shown in ~~orange~~blue, those ~~that which~~ fall within meltwater routes ~~which do host murtoos~~ (~~Murtoo-free without murtoos~~) are shown in ~~blue~~orange, and all other nodes are shown in ~~dashed~~purple. **A)** Water pressure expressed as a percentage of overburden, ~~overburden%~~ **B)** Sheet discharge, q_s . **C)** Water velocity, V_W . **D)** Channel discharge, Q_c . Note panels B and D have logarithmic scales.

have uncertain physical values, we did explore the relevant parameter space test the robustness of our findings from the baseline scenario throughout the ranges indicated in Table 2 and describe the outcome of these changes below. In GlaDS, the spacing and lengths of channels, and in turn the influence of these channels on water pressure at the channel limits, is most sensitive to k_s and k_c , describing the sheet and channel conductivity respectively. At the highest sheet conductivity (615 $k_s = 10^{-2} \text{ m}^{7/4} \text{ kg}^{-1/2}$, Figure A3) no channels longer than ~~one~~1 km are formed and water pressure is efficiently evacuated is instead more readily transmitted through the distributed system at relatively low pressures (~~<60% of overburden~~water pressures (~~overburden% < 60%~~). With a lower sheet conductivity ($k_s = 10^{-3} \text{ m}^{7/4} \text{ kg}^{-1/2}$, Figure A4), around 60 channels were largely limited to within ~ 10 km of the ice margin, and an area of ~~low effective pressure high overburden%~~ 40–60 km of the ice margin was limited to a short one month period at the peak of the melt season. At a minimum sheet conductivity (620 ~~$Kk_s = 10^{-5}$ ($k_s = 10^{-5} \text{ m}^{7/4} \text{ kg}^{-1/2}$, Figure A5)~~) ~ 40 channels extend up to 50 km back from the ice margin. These channels appear more complex than those in the baseline run, with a more sinuous geometry and higher number of tributaries. Additionally, an extended area of ~~low high~~ (but not ~~zero~~) ~~effective pressure 100%~~ ~~overburden%~~ extends up to 150 km from the ice margin.

At the maximum channel conductivity (~~$K_C = 0.5$~~ $k_c = 5 \times 10^{-1} \text{ m}^{3/2} \text{ kg}^{-1/2}$, Figure A6), ~ 30 relatively linear channels extend up to 60 km from the ice margin. The area of ~~low pressure is similarly highest overburden%~~ is pushed back to between 60–80 km from the ice margin, ~~and these pressures remain however overburden% remains~~ consistently below $\sim 90\%$ ~~of overburden~~. At $k_c = 0.05$. At $k_c = 5 \times 10^{-2} \text{ m}^{3/2} \text{ kg}^{-1/2}$ (Figure A7) ~ 30 channels are limited to ~ 40 km of the ice margin. Within the 40–60 km distance from the ice margin, ~~water pressures are overburden%~~ is consistently in excess of 100% ~~of overburden~~ throughout summer. At the lowest value of channel conductivity tested here ($k_c = 10^{-3} \text{ m}^{3/2} \text{ kg}^{-1/2}$, Figure A8)

630 a number of high ~~pressure~~ ~~overburden%~~ channels are restricted to within 1 km of the ice boundary, with a zone of ~~high~~ ~~water~~ ~~pressure~~ ($>100\%$ of ~~overburden~~) ~~overburden% > 100%~~ extending 70 km from the ice margin. ~~Excessively long (>50 km) or short (<10 km) channels compared to contemporary channels in Greenland and major changes in system pressure at the tested limits of k_s and k_c suggest our baseline conductivity terms are the most plausible parameters.~~

635 Changing the moulin density also alters the density, length, and complexity of channels as well as ~~pressure~~ ~~overburden%~~ beyond the upper limit of channel length. At the minimum moulin density tested ($N_{moulins} = 1000$, Figure A9), approximately 25 channels extend up to 50 km from the ice margin, ~~the location of which~~. ~~The location of these channels~~ closely follow the position of high discharge moulins near to the glacier terminus. A consequence of this is that ~~high~~ ~~water~~ ~~pressure~~ ~~overburden%~~ is less spatially continuous 40–60 km from the ice margin, though ~~areas where overburden% ≈ 100% are~~ still in strong agreement with murtoo field location. A higher moulin density ($N_{moulins} = 4000$, Figure A10) with lower discharge has a 640 similar impact on the spatial distribution of channels as increasing the conductivity of the sheet, with ~60 channels reaching a maximum of 10–20 km from the ice margin, the location of which appears limited to the lowest elevation moulins closest to the margin at which higher discharges are prescribed. With lower discharge moulins also existing upglacier however, an area of high ~~water~~ ~~pressure~~ ~~overburden%~~ extends up to 70 km from the ice margin. Routing water directly to the bed at every node instead of concentrating discharge through moulins (Figure A11) increases the frequency of short channels (~5 km) but 645 does not alter the spacing of larger channels, which extend up to ~40 km from the ice margin. Without water input at specific moulins, the area of ~~low~~ ~~pressure~~ ~~high~~ ~~overburden%~~ associated with larger channels does extend further, with a clear pressure influence extending a further 10 km beyond each channel head. Two different random variations of the default moulin density (Figures A12 & A13) altered the exact location of channels and pressure around these channels, but did not alter the overall pattern of pressure or drainage.

650 Changing the basal melt rate between $1-7 \times 10^{-3}$ m yr⁻¹ (Figures A14 & A15) had little impact on the pattern of channelisation and on pressure 40–60 km of the ice margin, likewise neither did altering the basal bump height between 0.1–0.05 m (Figures A16 & A17). Changing the mesh characteristics by not refining the mesh with respect to elevation alters the absolute position and detailed expression of channels but does not alter their spacing, length, or drainage in terms of pressure and discharge (Figure A18). Using a coarser mesh (Figure A19) lengthens channels, but this likely reflects the accompanying change 655 in catchment areas and resultant drainage patterns through fewer moulins. Increasing the resolution within 80 km of the ice margin (Figure A20), results in major channels (those with a length longer than 20 km) extending up to 5 km further, but with a lower discharge over their full length, supplemented by more frequent small channels within 10 km of the margin. The absolute position of large channels changes compared to the default mesh, but their horizontal spacing remains consistent.

660 Modelling with a flat bed (Figure A21), using a modern bed (without removing Quaternary sediment thickness, Figure A22), and including the available lake bathymetry (Figure A23) has limited impact on channel density, length or drainage (Figure A23). Changing the terminus boundary conditions to approximate drainage into a shallow (~30 m deep) water body (Figure A24) also has limited influence on our results. Raising the englacial void ratio ($E_{vr} = 10^{-3}$, Figure A25) results in more complex channel geometry, and by increasing storage ~~englacially~~ ~~englacially~~, confines pressure variability nearer to channels. Lowering the englacial void ratio ($E_{vr} = 10^{-5}$, Figure A26) has no clear influence on channel geometry or pressure.

665 Finally, changing the basal ice velocity to a fixed value of 100 m yr^{-1} (Figure A27) lowers ~~the water pressure overburden~~ 40–60 km from the ice margin by $\sim 10\%$ but does not alter channel spacing or length, while raising the basal ice velocity to a fixed value of 200 m yr^{-1} (Figure A28) lowers ~~the water pressure of overburden% within~~ channels $< 40 \text{ km}$ from the ice margin. Introducing annual transient variability in velocity with a mean velocity of 150 m yr^{-1} (Figure A29) limits the maximum length channels attain to $\sim 40 \text{ km}$ from the ice margin relative to a fixed velocity ~~and more tightly constrains the~~ 670 ~~observed summer water pressure equal or exceeding overburden to within~~. ~~In addition, the transient velocity results in a spatial distribution of overburden% $\approx 100\%$ in stronger agreement with the contours of~~ 40–60 km from the ice margin ~~compared to the baseline scenario~~. A transient velocity with a mean of 100 m yr^{-1} (Figure A30) does not clearly impact channels or ~~pressure overburden% < 60 km from the ice margin but does lower the water pressure overburden%~~ further from the ice margin by $\sim 5\%$. A transient velocity with a mean of 200 m yr^{-1} (Figure A31) has the opposite influence on ~~water pressure overburden%~~ 675 $> 60 \text{ km}$ from the ice margin.

5 Discussion

5.1 Seasonal drainage in a palaeoglacial setting ~~Catchment-scale hydrological configuration~~

680 The potential for comparing records of palaeo basal hydrology to subglacial hydrology model was recently demonstrated by Kirkham et al. (2022) evaluating hypotheses of tunnel valley formation using an upstream area routing algorithm (Arnold, 2010) ~~, a sediment erosion rate model (Carter et al., 2017), and modelled reconstructions of the British and Irish Ice Sheet (Clark et al., 2021)~~. By comparison against seismic profiles of tunnel valleys in the North Sea, Kirkham et al. (2022) found their formation to be most consistent with seasonal fluxes of meltwater delivered to the bed, and not single event outburst floods as previously hypothesised (see Hooke and Jennings, 2006). However, because tunnel valleys and eskers likely represent episodic drainage over millennial timescales during ice sheet retreat (Clark and Walder, 1994; Mäkinen, 2003) the area routing algorithm used by 685 Kirkham et al. (2022), and similar algorithms used by other studies (e.g., Livingstone et al., 2013a, b, 2015; Karlsson and Dahl-Jensen, 2013), make several simplifying assumptions about the pressure at which water exists, typically assuming water is at or near overburden pressure everywhere. While this assumption greatly reduces the computational expense of modelling subglacial water flow, and has been shown to be a realistic representation of average pressure over an entire melt season in Greenland (e.g., Banwell et al., 2013), it neglects dynamics associated with conditions variable over seasonal–diurnal timescales. Further, 690 such area-routing algorithms are inherently channelised and do not capture any transition between drainage modes (Banwell et al., 2013) ~~.~~

695 Murtoos are unique amongst glaciofluvial landforms in both their geomorphology and hypothesised genesis (see; Mäkinen et al., 2017). In contrast to previously examined landforms such as eskers and tunnel valleys, ~~which as channelised features have been previously investigated with relatively simple and inherently channelised basal hydrology models (e.g., Livingstone et al., 2013a, b, 2015; Karlsson and Dahl-Jensen, 2013)~~ ~~murtoos are thought to form within a transitional drainage regime as semi-distributed, drainage regime where widespread distributed systems give way to efficient and channelised drainage (Ojala et al., 2019). In this way, their predicted genesis allow us to constrain and define a parameter space for basal hydrology models such as GlaDS.~~ The weak to moderate deformation of

murtoo sediments periodically evident within murtoo vertical exposures indicates that water pressure remained at or close to overburden for sustained periods of time during murtoo formation (Peterson Beeher and Johnson, 2021; Mäkinen et al., 2023; Hovikoski et al., 2023; Peterson Becher and Johnson, 2021; Vérité et al., 2022; Mäkinen et al., 2023; Hovikoski et al., 2023). The broad and low geomorphology of murtoos, together with internal horizons that are vertically areuate along a comparable path arcuate at a similar curvature to the surface slope, suggest that murtoo deposition occurred within a low and broad cavity reaching a maximum water depth of 1 m (Hovikoski et al., 2023; Mäkinen et al., 2023). As discharge increases through a melt season, the cavity enlarges and is able to accommodate more sediment and water flow before closing as water discharge decreases late in the melt season (Peterson Becher and Johnson, 2021; Mäkinen et al., 2023; Hovikoski et al., 2023). Crucially, the cavity never enlarges enough to form a channel of any appreciable size (Mäkinen et al., 2023). Instead murtoo formation is suggested to occur 40–60 km from the ice margin where modelling of the basal hydrology in Greenland indicates (Ahokangas et al., 2021). At similar distances from the ice margin in Greenland, shallow surface gradients limit the engender low hydraulic potential gradients, while low crevasse density limits meltwater input to the bed (Gagliardini and Werder, 2018), which together prevent the water supply necessary to grow low-pressure channels (Dow et al., 2015). These low ice surface gradients together with surface melt input instead permits only limited broad canals within a pressurised large, low water pressure channels (Dow et al., 2015; Bartholomew et al., 2011; Chandler et al., 2013; Ojala et al., 2019). Accordingly, murtoo formation is suggested to occur 40–60 km from the ice margin, within a high water pressure semi-efficient drainage system (e.g., Bartholomew et al., 2011; Chandler et al., 2013; Greenwood et al., 2016; Ojala et al., 2019; Hooke and Fasmer, 2023; Hovikoski et al., 2023; Mäkinen et al., 2023).

In our base model and The predicted conditions associated with murtoo genesis therefore provide a unique set of criteria against which we can test GlaDS, a model of basal hydrology capable of resolving the transition in drainage modes between distributed and channelised water flow (Werder et al., 2013). Our modelling output here, in both the baseline model (Section 4.1) and many of the sensitivity tests, at the edge of channelised drainage 40–60 km from the ice margin, GlaDS closely matches several predictions for murtoo genesis and their depositional environment. Across the full model domain <70 km upglacier from the ice margin, supporting the idea that murtoos form in the system exhibits a periodic spike in water pressure associated with the onset of transient moulin meltwater input up to and beyond 100% of overburden (Figure 4D–E) that is not evident further upglacier (transition in drainage from distributed systems to channelised systems (Ojala et al., 2019). During the melt season, modelled channels align well with murtoo fields in the southwest and northeast portions of the FLDIL (e.g., Figure 4A). However, within 40–70 km from the ice margin and at the limit of channelisation, water pressure is consistently at or near overburden resulting in a band of high water pressure when plotted as a summer average (Figure 3A). Elsewhere water pressure remains lower margin is 2.8 m² (equivalent to a semi-circle with radius of 1.3 m), close to the maximum cavity height of 1 m inferred from boulder distributions in the upper slope of murtoos (Hovikoski et al., 2023). In GlaDS, channels are assumed to be semi-circular R-channels, not broad and low canals (as described by Walder and Fowler, 1994). However, the close agreement in approximate radius suggests that the

limited cavity expansion or restricted channel floor width within which murtoo form is captured within our model. At the head of channels in our baseline model, our modelling also reproduces the expected window of high $overburden\% \approx 100\%$ within 40–60 km of the ice margin associated with the presence of a semi-distributed system during the melt season (Figures 3, 4 and A). If we accept the hypothesis that murtoos form where $overburden\% \approx 100\%$ our modelling supports the idea that the murtoos mapped >70 km from the ice margin postdate 12 cal. ka and that murtoo formation is time-transgressive (Ahokangas et al., 2021). Within 40 km of the ice margin, $overburden\%$ remains lower than 100% in both winter and summer, reflecting i) the presence of channelised drainage efficiently evacuating water close to the ice margin (<40 km) during summer and ii) the limited meltwater supply across the domain during winter. Further than 70 km from the ice margin, ~~water pressure remains high with low or zero atmospheric meltwater input, $overburden\%$ remains constant throughout the year, rarely dropping below 75% (Figure 4C–E)~~. We note that in the uncoupled configuration used here, GlaDS does not account for uplift of the overlying ice where water pressure exceeds 100% of overburden or the increase in cavity closure rates that would accompany the increase in basal velocity associated with such an uplift. In reality, sustained summer water pressure above and beyond overburden would result in the decoupling of the ice from the underlying bed necessary to explain the limited deformational structures within murtoo sediment exposures (e.g., Peterson Becher and Johnson, 2021; Mäkinen et al., 2023; Hovikoski et al., 2023).

The pattern of both channel discharge and sheet discharge within 40–60 km of the ice margin is also consistent with the development of the semi-efficient drainage system within which murtoos are hypothesised to form. Here, within meltwater routes (those both with and without murtoo fields), the median channel discharge approaches $\sim 10^0$ expression of modelled channels holds for most but not all of our sensitivity tests. At the upper and lower magnitude limit of the conductivity terms, the channel length changes as the efficiency with which either the distributed or channelised system could transmit water was limited so that either no channels formed or a high density ($n = 50$) of very short channels (5–10 (e.g., Figure 5D)), close to but never exceeding the critical discharge of channelisation as defined here ($Q_c = 1$). Channel discharge in these meltwater routes peaks months after the highest water pressure at km formed close to the onset of the melt season, as cavity expansion promotes lower pressure and more efficient discharge that, in turn, is able to redirect more water from the sheet elements along pressure gradients. Channel discharge remains relatively high throughout the meltwater season, dropping only as meltwater supply diminishes through the following winter ice margin. Similarly, when moulin density was highest, the reduced discharge associated with any one moulin resulted in a higher density of short channels. In each of these models, the pattern of $overburden\%$ reflects the length of channels and an area of high $overburden\%$ is either not present at all, or extends nearly the full extent of the FLDIL lobe where moulin density is extremely high and numerous low discharge moulins result in a highly pressurised distributed system. However, the pattern of $overburden\%$, channel length and spacing remains largely insensitive to all other parameter changes relative to the baseline model, suggesting our conclusions are largely robust to specific parameter choices and that the baseline model is a plausible representation of the FLDIL drainage system.

At several locations within the 40–60 Without extant ice in the FLDIL against which to test the validity of our model inputs and outputs, we are unable to fully determine the correct model parameters to describe our FLDIL domain. As a result, the baseline model was parameterised following existing work on contemporary ice sheets (see Section 3.1.2). As expected, the baseline model provides a range of seasonal water pressure and channel lengths that are similar to models of contemporary ice sheets validated with geophysical methods (e.g., Dow et al., 2020). At the catchment scale, our results closely match the apparent spatiotemporal expression of channelisation in land-terminating sectors of the Greenland Ice Sheets. Tracer transit times (e.g., Chandler et al., 2013) and basal hydrology modelling indicate efficient channelisation extends up to 40–50 km area of hypothesised murtoo formation, some element edges do pass the threshold discharge for channelisation throughout the melt season. Although GlaDS does not include a representation of broad and low canals (as described by Walder and Fowler, 1994) many of these low-discharge R-channels do align well with murtoo fields in the southwest and northeast portions of the FLDIL (e.g., Figure 4C). The median cross-sectional area of channels 40–60 from the margin is 2.8 ice margin in Greenland, transitioning between channelised and distributed drainage modes at ice where ice is ~900–1200 (equivalent to a semi-circle with radius of 1.3 m), which suggest the limited cavity expansion within which murtoo sediments can accumulate is captured within our model, even if the radial geometry differs. Modelled channels do not always coincide with murtoo fields, particularly within the centre of our domain, 40–60 from the ice margin. Here, our baseline scenario also reproduces apparent conditions for murtoo formation, including the termination of low-discharge channels and water pressures ≈100% over a broad area during summer (e.g., Figure 5E). Despite this, no murtoo fields have been mapped in this area (Ahokangas et al., 2021). The reason that murtoos are not present in an area of the FLDIL where our modelling suggests they should form may be due to limited sediment supply in and upglacier of this murtoo-free region. Sediment cover in this area is very thin, and thick (De Fleurian et al., 2016; Dow et al., 2015) as it does here. However, the large areas of exposed bedrock likely limited the supply of sediment from which murtoos could form (Figure A1B), an interaction not yet accounted for in our modelling pressure conditions within large channels close to the ice margin is notably different in our model results when compared to observations beneath the contemporary Greenland Ice Sheet (e.g., Van de Wal et al., 2015). In Greenland, subglacial channels form seasonally in response to meltwater discharge and exist at lower water pressures than the surrounding distributed system (Davison et al., 2019). The resultant hydraulic potential gradient forces large volumes of water from the surrounding distributed system towards channels, in turn lowering water pressure in the distributed system and increasing basal traction (Schoof, 2010). Even as meltwater delivery to the bed increases through the melt season, these channels can act to reduce ice velocity (Nienow et al., 2017) and reduce ice mass loss. In contrast, the channels modelled here remain at relatively high overburden% throughout the year (> 60%), with a lower hydraulic potential gradient between channelised and distributed systems. The FLDIL is relatively low-relief compared to the steep margins of the Greenland Ice Sheet (e.g., Wright et al., 2016), and the shallow topography may act to reduce the hydraulic gradient between distributed and channelised drainage. In a system such as the FLDIL, with low relief bed topography and high-pressure channels, it is likely that the influence of channelisation on velocity would be relatively limited, as lower rates of water exchange between distributed and channelised drainage permit more of the bed to remain closer to overburden% ≈ 100%, sustaining higher velocities for extended periods of time as a result (Dow et al., 2022).

More broadly, modelled channels also compare well to geomorphological evidence of channelised drainage pathways beneath the FLIDL. Northern hemisphere glaciated Pleistocene terrains preserve an extensive record of subglacial landforms, and in terrain formerly occupied by the Fennoscandian Ice Sheet (FIS) these landforms have been mapped and classified in detail (e.g., Ahokangas et al., 2021; Palmu et al., 2021; Dewald et al., 2021). In the FLIDL, besides numerous murtoo fields, large esker deposits also provide a useful means of evaluating model outputs

5.2 Comparison with glaciofluvial landforms

We can also evaluate our model outputs by making comparisons to other glaciofluvial landforms. Modelled channels in our baseline model (Figure 2) and many of the sensitivity tests have similar locations as eskers mapped by Palmu et al. (2021), particularly in terms of their lateral spacing, length, and the observation that smaller esker deposits are alternately found between large features (Figure 2). Although their exact mode of origin remains contentious (see Section 1), they are considered to largely represent deposition of sediment within subglacial channels beneath former ice sheets (Cofaigh, 1996; Greenwood et al., 2016). The location and characteristics of these landforms offer a useful means of evaluating model outputs from sensitivity tests. In The horizontal spacing (~ 15 km) of our channels is in close agreement with the theoretical spacing of eskers derived from the modelling results of Boulton et al. (2009) and Hewitt (2011). In the baseline model specifically, at several locations, modelled channel outputs in the baseline scenario closely track closely track the location of several particularly large esker deposits mapped by Palmu et al. (2021) (Figure 2). Further, the ~ 30 horizontal spacing of larger eskers agrees well with modelled channel placement, and the observation that smaller eskers are interspersed amongst longer more continuous features (variable preservation notwithstanding) is similarly reproduced. Operating on an unstructured mesh, GlaDS is not subject to the same directional bias as grid-based models. Nonetheless B–C). We caveat this by noting that because our model operates on a mesh, the resolution of which is a balance of suitable fidelity against the increased computational cost of resolving finer details, the exact location of these modelled channels is sensitive to mesh geometry. Altering the mesh does alter the exact placement of channels, however, the spacing Channels cannot form where no element edge exists. Differences in the exact channel location also arise because of moulin density and location, bed topography, velocity, and basal bump height. Nonetheless, the spacing and length of channels remains robust against the species of the various mesh geometries tested here (Figures A19, A20, A18). We also note that GlaDS successfully reproduces the distinction between meltwater routes (both with and without murtoos) and areas of the bed without any mapped meltwater routes (Figure 5). This, together with the similarity between mapped and modelled patterns of channelised drainage, suggest that parameters tested here, and compares favourably to previous work, suggesting GlaDS is faithfully capturing the broad patterns of drainage beneath the FLIDL.

Considered across the model domain, our results closely match the apparent spatiotemporal expression of channelisation in land-terminating sectors of the GrIS. In

5.3 Comparison between model outputs and mapped murtoo locations

In order to directly compare the model outputs and location of mapped murtoos we grouped nodes according to whether they fell within a murtoo/meltwater route (both mapped by Ahokangas et al., 2021, see Section 3.2). For this analysis, we isolated

835 nodes within 40–60 km of the base run Section 4.1, small channels ($1 \leq Q_c \leq 5$) ice margin. In doing so we accept the hypothesis that murtoos formed time-transgressively within 40–60 km extend up to a maximum of 60 km from the ice margin, where ice is between 1000–1100 m of the retreating ice margin (Ojala et al., 2019; Ahokangas et al., 2021) an assumption that our baseline model and sensitivity runs would suggest is valid (Section 5.1). A general pattern emerges within these murtoo and meltwater route nodes that is absent in other nodes (Figure 5), one which largely agrees with the timeline of murtoo formation in a
840 semi-distributed drainage system (Table 1, Peterson Becher and Johnson, 2021; Mäkinen et al., 2023; Hovikoski et al., 2023). At the onset of the melt season, *overburden%* and q_s sharply increases and peaks followed by peaks in Q_c and V_W . The peak in Q_c promotes a rapid drop in *overburden%* and q_s , as cavity expansion promotes lower water pressure and more efficient discharge that, in turn, is able to redirect more water from the sheet elements along pressure gradients. In comparison, Q_c drops more slowly, not reaching a minimum until the end of winter in the following year, at which point there is an
845 abrupt drop in V_W and q_s coinciding with the minimum Q_c . Although the seasonal evolution is consistent with the formation of a murtoo, we fail to reproduce the sharp drop in discharge at the end of the melt season or the rapidly changing flow regimes within a single melt season (see Mäkinen et al., 2023; Hovikoski et al., 2023, and Section 2). However, in GlaDS the subglacial system is assumed to be pervasively hydraulically connected, and there is no mechanism which can lead to the hydraulic isolation of specific areas of the bed (e.g., Rada and Schoof, 2018; Hoffman et al., 2016). As a result, we do not
850 expect to be able to reproduce the rapid changes in meltwater discharge necessary to form upper and lower flow regime deposits (e.g., Hovikoski et al., 2023, see Section 2) or laminated muds in marginal murtoo channels (e.g., Ojala et al., 2022). Nonetheless, the overall evolution of the system through time, and the sharp difference between murtoo/meltwater routes and areas of the bed without geomorphological evidence of meltwater suggests that the baseline model is successfully reproducing many of the expected conditions of murtoo formation.

855 Our baseline model also makes a statistically meaningful distinction between murtoo routes and every other meltwater route (Section 4.1.2). The differences in probability distribution functions are largely similar between murtoo routes and meltwater routes, with the exception of noticeable differences particularly at the lower end of the distribution (Figure 6). Murtoo routes in particular have a *overburden%* distribution with a more tightly constrained lower tail with fewer nodes dropping below *overburden% = 80%* and a more variable V_W than meltwater routes. Through time, the difference for each
860 parameter is statistically significant (Tables A1– A4) during the melt season and also variable biannually (Figure 5). In terms of *overburden%* this takes the form of higher water pressures within murtoo routes than in meltwater routes after the start of the melt season during even-numbered years. For the other outputs (q_s , Q_c , and V_W), every year, at the start of the year values are lower at the start of the melt season in murtoo routes. In odd-numbered years, this is followed by a brief peak in murtoo routes not replicated in meltwater routes. In the following, even-numbered years, the values in murtoo routes are lower, for
865 longer. This biannual signal can also be seen at individual nodes. Node No. 16.402, located 0.7 m thick, and larger channels reach a maximum of 40 km inland (from a murtoo field and ~850 m thick). Beneath the GrIS, tracer transit times indicate efficient channelisation reaches at least 41 km from the ice margin (Chandler et al., 2013). However, beyond this, thicker ice, which enhances creep closure, and shallower surface gradients which limit hydropotential gradients, likely inhibit channel growth (Röthlisberger, 1972; Davison et al., 2019). Previous modelling of the GrIS indicates the transition between channelised and

870 distributed drainage occurs between ice 900–1200 thick (Davison et al., 2019) with channelisation identified up to a maximum of 50 km from the ice margin, where ice is from the ice margin (Figure 4D), chosen to be representative of nodes in the immediate vicinity, undergoes an evolution through time similar to that within all meltwater routes and to the murtoo formation sequence, but only in odd-numbered years. In even-numbered years, *overburden%* peaks for longer and is elevated throughout the following winter, with much lower Q_c as a result. This is in contrast to the similarly located Node No. 3,842, ~90045 thick
875 (De Fleurian et al., 2016) but absent 70 km from the ice margin beneath ice 1200 thick (e.g., Dow et al., 2015).

On the GrIS, the upglacier propagation of rapid subglacial water velocities throughout the melt season (Chandler et al., 2013) and close correlation of proglacial discharge (Bartholomew et al., 2011) is linked to the development of channelised drainage (Davison et al., 2019). This process is considered analogous to that which occurs on Alpine glaciers (see Nienow et al., 1998) with meltwater delivered to the bed at high elevations initially encountering a distributed drainage system that becomes
880 increasingly channelised with sustained meltwater delivery to the bed (Bartholomew et al., 2011). Similarly, the growth and decay of modelled channels here largely matches the seasonal evolution of those modelled and observed beneath the GrIS. Channels propagate up-glacier throughout the melt season and coalesce into fewer, larger, channels as the melt season progresses (from the ice margin and not neighbouring any murtoo fields, which undergoes a repetitive evolution year on year (Figure 4E).

A notable difference between our model results and those beneath contemporary Greenland is the pressure conditions within
885 large channels close to the margin. Beneath Greenland, channels form seasonally in response to meltwater discharge and exist at lower pressures than the surrounding distributed system (Davison et al., 2019). Such a hydraulic potential gradient forces large volumes of water from the surrounding distributed system towards channels. It is difficult to say whether or not these differences are truly the model capturing subtle differences between water flow in meltwater routes and murtoo routes or if they arise due to our model setup. There is, for an example, a spatial component to the biannual signal in our murtoo route outputs,
890 potentially linked to the observation of winter channels persisting after the end of the melt season. Modelled channels, and the conditions at their headward extension do not always coincide with murtoo fields, particularly within the centre of our domain, 40–60 km from the ice margin. Here, our baseline scenario also reproduces apparent conditions for murtoo formation, including the termination of low-discharge channels and $overburden\% \approx 100\%$ over a broad area during summer (e.g., Figure 5E). Despite this, no murtoo fields have been mapped in this area (Ahokangas et al., 2021). Winter channels meanwhile follow a
895 pattern in which channels in the central third of the FLDIL lobe persist in alternating winters to those in the northernmost and southernmost outer thirds. The presence of these winter channels likely influences the nearby system through the following summer, in turn lowering water pressure in these systems and increasing basal traction (Schoof, 2010). As a result, despite increased meltwater delivery to the bed, these channels can act to reduce summer velocity (Nienow et al., 2017). In contrast, the channels modelled here remain at relatively high pressures throughout the year (> 60%), with a lower hydraulic potential
900 gradient between channelised and distributed systems. Although we run GlaDS here without any coupling to ice dynamics, it is likely that the influence of higher pressure channels on velocity would be more limited in such a system, with lower rates of exchange between distributed and channelised drainage permitting more of the bed to remain closer to overburden and sustaining higher velocities as a result (Dow et al., 2022) with preexisting channels dampening the influence of the initial melt input by providing an already established efficient drainage pathway. With an absence of murtoos in the central third

905 of the lobe, the significant biannual difference between murtoo routes and meltwater routes (distributed more evenly across the FLDIL, Figure A1A) may be an artefact of the spatial expression of winter channels. Murtoos appear to form within a semi-distributed drainage environment, and sedimentological studies indicate the movement of sediment is important in murtoo formation (Peterson Becher and Johnson, 2021; Mäkinen et al., 2023; Hovikoski et al., 2023). The reason that murtoos are not present in the centre of the FLDIL where our modelling suggests they should form may be a preservation issue or due to limited
910 sediment supply. Sediment cover in this area is very thin, and the large areas of exposed bedrock likely limited the upstream supply of sediment from which murtoos could form (Figure A1B), an interaction not yet accounted for in our modelling. Modern lakes are also abundant in the centre of the FLDIL and these may also act to mask murtoo routes.

Modelled channel location compared to esker deposits mapped by Palmu et al. (2021) at the ice margin of the FLDIL. **A**) Modelled channels in the baseline run (black lines) across the full width of the domain against compared to esker deposits (blue polygons). **B & C**) Detailed comparison of two large esker systems against model channels.

Finally, we observe a biannual signal in our results, manifesting as both channel persistence through winter, as well as a statistically significant difference in the modelled characteristics of murtoo routes and meltwater routes without murtoos. In Greenland However, the factors giving rise to the spatial pattern of winter channels themselves are more complex. On the Greenland Ice Sheet, winter slowdowns following high-melt summers have been linked to the sustained persistence of larger
920 and more extensive channels into winter months (Sole et al., 2013). In our model, a biannual signal is evident in both channel persistence (e. g., Figures 4 & 3) and overburden within murtoo hosting meltwater routes (Figure 5). A number of channels persist through winter months, broadly following a pattern in which channels in the central third of the lobe will persist through alternating winters compared to those in the adjacent thirds (and their existence alone in our baseline model is not necessarily surprising. There is a spatial variability to our meltwater inputs, arising from heterogeneity in the climate reanalysis used to
925 estimate the Younger Dryas climate (Section 3.1.1). However, our model forcing, though cyclical, has no interannual variability and no melt seasons are any more elevated than others. Additionally, as described in Section 3.1 and following Werder et al. (2013), a minimum threshold $Q \geq 1$ an arbitrary minimum threshold $Q_c \geq 1 \text{ m}^3 \text{ s}^{-1}$ was defined, above which Q_c along an element edge was classified as a channel meaningful 'channel'. Channels persisting through winter months tend to operate at very low discharges approaching 1×10^{-6} of $1-3 \text{ m}^3 \text{ s}^{-1}$. Additionally our model forcing is cyclical but fixed year on year, and
930 so this biannual pattern may arise due to internal model dynamics. A similarly repetitive biannual signal is considered unlikely in a system subject to more variable meltwater forcing. The observations that murtoo routes are generally absent from the centre of, and would not be categorised as channels with a higher threshold. Nonetheless, despite their low discharge and our fixed cyclical forcing, these channels do have a discontinuous spatial distribution with a biannual signal, which together with their winter persistence must arise, at least in part, for reasons besides our choice of external climate forcing or our choice of Q_c threshold.

We anticipate that the FLDIL lobe and the alternating pattern of winter channel persistence between the central third and adjacent thirds of the lobe likely explains the lobate geometry of our model domain, chosen to be representative of the extent of the FLDIL ~ 12 cal. ka may in part control the spatial expression of winter channels in our baseline model, in turn contributing to the significant difference in water pressure, discharge, and velocity between murtoo routes (confined to the outer margins of

940 the ice lobe) the drainage characteristics of murtoo and meltwater routes without murtoos (distributed more evenly across the FLDIL, Figure A1A).

945 Although the biannual pattern of channel growth is likely driven by internal model dynamics and our fixed annual forcing, murtoos are observed to occur in discrete clusters along otherwise continuous meltwater routes (Ahokangas et al., 2021). Differential rates of feature preservation notwithstanding, such a discrete spatial expression may suggest the conditions necessary for murtoo formation were not met continuously throughout the retreat of the Fennoscandian Ice Sheet, rather they may occur periodically during or following extreme melt years. With a consistent rate of meltwater delivery between each model year, our modelling suggests that periodically elevated pressures can arise as a result of internal model dynamics alone, without any temporally variable forcing. Such internal model dynamics may include localised divergences in ice flow in our model. The divergence of ice flow vectors within the lobe appear to act as an initial perturbation which, together with spatial variability in the climate signal, results in an initially non-uniform concentration of meltwater within the lobe. We hypothesise that this local concentration of meltwater promotes large enough channels in portions of our model that are able to resist closure during winter, which subsequently act to more efficiently remove meltwater and lead to an earlier peak discharge the following summer, and an earlier closure in the following winter. Such a repetitive biannual signal, and with it the resulting significant difference between murtoo routes and meltwater routes, is unlikely to persist in a more realistic model setup in which basal 950 velocity can change in response to water pressure and subject to more realistic variability in meltwater forcing. Nonetheless, the landform record in the FLDIL does suggest that the divergence of flow in the ice lobe is an important control on glaciofluvial landform generation. In the FLDIL, flow parallel lineations indicate a largely uniform flow direction within the primary trunk (e.g., Figure 1D-E) indicate a largely uniform flow direction within the primary trunk that diverges radially within the lobe. As a result, the FLDIL is landforms within the FLDIL have previously been divided into three sub-lobes, with the boundary 955 between each. The boundaries between these three sub-lobes are demarcated by particularly large esker deposits suggesting a concentration of meltwater here (Palmu et al., 2021). These eskers and the sub-lobes they bound align approximately with the distinct alternating pattern of over-winter channel persistence, with channels persisting in years following the over-winter persistence of central channels. Local deviation in ice flow direction may act as an initial perturbation which results in an initially enhanced meltwater delivery in the outer sub-lobes. We hypothesise that this locally enhanced discharge encourages 960 the growth of channels large enough to resist the subsequent viscous creep closure in the following winter. In the following summer, more discharge is concentrated in these overwinter channels and water is more efficiently evacuated. Peak discharge is therefore met earlier in the season and these channels are subsequently exposed to longer periods in which creep closure exceeds channel growth. Simultaneously, because no channels persisted overwinter in the centre of the lobe, peak discharge is later in this region which results in late season discharge routed to the central channels and their persistence as these channels 965 grow large enough to resist viscous creep closure overwinter. This initial perturbation and formation of overwinter channels creates an interannual cycle feedback that persists despite temporally fixed input. In our current model setup, without ice dynamics coupled to basal hydrology and with an annually fixed meltwater input, we cannot fully test this hypothesis further though it would be an interesting avenue for future study.

5.4 Limitations and future work

975 We make a number of simplifying assumptions to ensure models could run to completion ~~within with a walltime of~~ 1–2 days while remaining numerically stable across the range of parameters tested for model sensitivity. These include smoothing of the bed topography below the maximum resolution available, and using a relatively large mesh. However, sensitivity testing indicates our conclusions are largely insensitive to topography, including its absence, and that the ice surface gradient instead imposes the dominant control on basal hydrology. Similarly, changing the mesh resolution also appears to have limited impact
980 on our conclusions. We did not account for changes in elevation due to glacial isostatic adjustment (GIA) since 12 cal. ka. Accounting for an anticipated uplift and tilting in this area ~~reaching a maximum~~ of \sim 100 m (Ojala et al., 2013; Rosentau et al., 2021) is likely to increase the volume of melt delivered to the bed by elevating the mean annual air temperature by ~~up to~~ 0.75°C ~~near to the ice margin where uplift rates are highest~~, which will result in higher discharge channels that persist further upglacier. ~~However, we do not anticipate this will significantly alter our conclusions, of those high-uplift areas.~~ Additional uncertainty arises from our estimated (and constant) meltwater and basal melt inputs, ~~lack of diurnal forcing~~, fixed basal velocity, 985 fixed conductivity parameters (in both space and time), ~~lack of ice deformation in response to negative effective pressures~~ ~~fixed semi-circular channel geometry~~, assumed water turbulence, ~~pervasive hydraulic connectivity~~, lack of water flux ~~input~~ from abutting ice, and randomly seeded moulin inputs. ~~Future work will~~ Changes in geometry are known to be important in synthetic experiments of GlaDS (see Hayden and Dow, 2023) whereas we kept ice geometry fixed here. Finally, we note that in its
990 uncoupled configuration, GlaDS does not account for a reduction in the frictional resistance to ice flow where ~~overburden~~ exceeds 100% or the increase in cavity closure rates that would accompany the increase in basal velocity associated with such a change in friction. In reality, sustained summer ~~overburden~~ \geq 100% would result in the decoupling of the ice from the underlying bed as is suggested to be the reason for the limited observations of deformational structures within murto sediment exposures (e.g., Peterson Becher and Johnson, 2021; Mäkinen et al., 2023; Hovikoski et al., 2023). Future work should seek to
995 address some of these limitations by including, for example, ~~a more variable climate or~~ coupled ice dynamics ~~which are~~ whereby the frictional resistance to ice flow is allowed to vary in response to ~~effective pressure changes~~ ~~overburden~~ (e.g., as in Ehrenfeucht et al., 2023). Initial sensitivity testing of velocity forced to change seasonally does indicate that changes in velocity throughout the year is important for repressurising the system each winter to more closely match borehole records (e.g., Doyle et al., 2018, 2022). ~~Considering each of these limitations our results therefore describe the seasonal evolution of channelised and distributed drainage system beneath a necessarily idealised representation of our study site in the FLDIL. However, we emphasise that our results suggest that the approach of examining palaeo basal topography alongside subglacial hydrology model outputs holds promise for mutually beneficial analyses of palaeo and contemporary ice sheets to assess the controls of hydrology on ice dynamics and subglacial landform evolution.~~

1000

6 Conclusions

1005 ~~We successfully reproduce the macro conditions associated with murto formation by applying GlaDS, a dynamic model of basal hydrology, to the palaeo-~~

In this paper we present the first application of the Glacier Drainage System model (GlaDS)—a dynamic basal hydrology model capable of resolving transitions between distributed and channelised drainage—to the palaeo setting. In doing so, we compared model outputs against the predicted conditions associated with murtoo genesis. Murtoos are a unique glaciofluvial landform, identified throughout Finland and Sweden in terrain formerly occupied by the Fennoscandian Ice Sheet (FIS). The alternating sequence of upper and lower flow regimes preserved within murtoos suggest that they formed amongst a network of small channels and cavities subject to rapid changes in water discharge and where water pressure met or exceeded ice overburden pressure. Further, their spatial distribution, rarely found closer than 40 km from the ice margin and often found downstream of ribbed moraines and upstream of eskers, suggests that murtoos represent the glaciofluvial imprint of a spatial and/or temporal transition between distributed and channelised drainage. We modelled this system using a setup representative of the Finnish Lake District Ice Lobe (FLDIL) forced by a positive degree-day model. Our model was parameterised using high-resolution digital elevation models, modified to approximate the terrain during the end of the Younger Dryas, ~12 cal. ka, together with a model representation of. Our model was forced with a positive degree model representative of the palaeo climate, as well as a modified digital elevation model and reconstructed ice surface elevation for representative of the same time period. By sensitivity testing a range of parameters difficult to measure, including conductivity and moulin density, we demonstrate that murtoo genesis is consistent with their formation

Our model outputs reproduce many of the conditions predicted for murtoo genesis including:

- i. An extensive area of water pressure at or equal to ice overburden pressure 40–60 km from the ice margin at the onset of channelisation, where water pressure is consistently at or near overburden pressure during summer. Our modelling reproduces the concentration of meltwater into discrete channels, matching the approximate spacing and characteristics of geomorphology such as eskers. The spatial distribution of murtoos, which are present in discontinuous fields within otherwise continuous meltwater routes, may arise following consecutive years of elevated meltwater volumes, largely robust to the range of parameters tested here.
- ii. The annual evolution of a semi-distributed drainage system, which matches many of the anticipated conditions for murtoo genesis.
- iii. The limited expansion of small cavities within the area of high water pressure to a maximum diameter of ~1 m.
- iv. Modelled channels which extend 40–50 km from the ice margin extending headward into the hypothesised transitional drainage zone associated with murtoo formation. These channels also have a similar spacing and geometry to mapped eskers in the region.
- v. A statistically meaningful difference between areas of the bed without any indication of meltwater flow and areas of the bed with meltwater routes or murtoo routes.

Murtoo fields are not universally present where the conditions for their formation are predicted in our model, particularly within the centre of the FLDIL lobe, and we interpret this as a lack of upstream sediment supply further compounded by the

1040 high-density of terrain-obscuring lakes in this area. Additionally, we also find a statistically meaningful difference in water pressure, velocity, and discharge, between meltwater routes and murtoo routes, we interpret this as a combination of patchy murtoo distribution and internal model dynamics relating to the radial geometry of the lobe. Nonetheless, many of our model outcomes from the baseline model, in particular the area of high water pressure 40–60 km from the ice margin, are robust across the majority of 29 additional sensitivity tests carried out here, in which various values for model parameters and boundary conditions were tested within a range of numerical stability. At extremely high and low values of conductivity, parameters 1045 controlling how readily water flows through the distributed or channelised system, water was evacuated from the system too easily or slowly to form meaningful channels. However, across all other tests, including random mesh geometries, alternate bed topographies, changing ice velocity, and changing moulin density, similar patterns of modelled channels and water pressures emerge. Although our system is necessarily an idealised representation of the study site, not area—not including adjacent and abutting ice lobes, an upstream catchment area, or a coupled representation of ice dynamics and basal hydrology, this 1050 hydrology—this work nonetheless demonstrates the potential for basal hydrology modelling in application of state of the art basal hydrology models to the palaeo setting, where model outputs can be directly compared to geomorphology and specific models of landform genesis.

1055 *Code and data availability.* All geophysical data used to parameterise the modelling (e.g., Quaternary sediment thickness, geothermal heat flux, lake bathymetry) is available from Finnish Geological Survey's 'Hakku' service (<https://hakku GTK.fi/?locale=en>, last accessed on 06-09-2023). The Copernicus DEM used as basal elevation is available from: <https://spacedata.copernicus.eu/collections/copernicus-digital-elevation-model> (last accessed on 06-09-2023). For our modelling we used the Ice-sheet and Sea-level System Model (Larour et al., 2012) revision 27448 available from: <https://issm.jpl.nasa.gov/> (last accessed on 06-09-2023). Murtoo field locations from Ahokangas et al. (2021), glacial landforms shapefile data from Palmu et al. (2021), model results, and example input scripts used to produce and plot those results are available at the repository linked to this manuscript (<https://doi.org/10.5281/zenodo.8344208>, Hepburn et al., 2023)

1060 *Video supplement.* Movie A1 is available at the online repository linked to this article (<https://doi.org/10.5281/zenodo.8344208>, Hepburn et al., 2023).

Author contributions. A.O, J.M, and C.F.D conceived the study, A.J.H designed and carried out the study and wrote the manuscript, all authors commented on the writing and helped with the analysis and interpretation.

Competing interests. The authors declare that no competing interests are present

1065 *Acknowledgements.* This work forms part of the RewarD project (MUST consortium, University of Turku), funded by the Academy of
Finland (grant numbers 322243/J.M and 322252/A.O). A.J.H is funded by the European Space Agency Internal Fellowship program, C.F.D
is funded by the Canada Research Chair program (950-231237). All simulations were run on the Digital Research Alliance of Canada
compute cluster, and we thank the European Union and the Finnish Geological Survey for enabling access to the data used to parameterise
our model. We thank M.Werder for making the GlaDS model available, and we also thank M. Morlighem, J. Quinn, and J. Cuzzone for their
1070 help with ISSM.

References

Abatzoglou, J. T., Dobrowski, S. Z., Parks, S. A., and Hegewisch, K. C.: TerraClimate, a high-resolution global dataset of monthly climate and climatic water balance from 1958–2015, *Scientific data*, 5, 1–12, 2018.

Ahokangas, E., Ojala, A. E., Tuunainen, A., Valkama, M., Palmu, J.-P., Kajuutti, K., and Mäkinen, J.: The distribution of glacial meltwater routes and associated murtoo fields in Finland, *Geomorphology*, 389, 107 854, 2021.

1075 Åkesson, H., Morlighem, M., Nisancioglu, K. H., Svendsen, J. I., and Mangerud, J.: Atmosphere-driven ice sheet mass loss paced by topography: Insights from modelling the south-western Scandinavian Ice Sheet, *Quaternary Science Reviews*, 195, 32–47, 2018.

Amon, L., Wagner-Cremer, F., Vassiljev, J., and Veski, S.: Spring onset and seasonality patterns during the Late Glacial period in the eastern Baltic region, *Climate of the Past*, 18, 2143–2153, 2022.

1080 Arnold, N.: A new approach for dealing with depressions in digital elevation models when calculating flow accumulation values, *Progress in Physical Geography*, 34, 781–809, 2010.

Banwell, A. F., Willis, I. C., and Arnold, N. S.: Modeling subglacial water routing at Paakitsoq, W Greenland, *Journal of Geophysical Research: Earth Surface*, 118, 1282–1295, 2013.

Bartholomew, I., Nienow, P., Sole, A., Mair, D., Cowton, T., Palmer, S., and Wadham, J.: Supraglacial forcing of subglacial drainage in the 1085 ablation zone of the Greenland ice sheet, *Geophysical Research Letters*, 38, 2011.

Bartholomew, I., Nienow, P., Sole, A., Mair, D., Cowton, T., and King, M. A.: Short-term variability in Greenland Ice Sheet motion forced by time-varying meltwater drainage: Implications for the relationship between subglacial drainage system behavior and ice velocity, *Journal of Geophysical Research: Earth Surface*, 117, 2012.

Beaud, F., Flowers, G. E., and Venditti, J. G.: Modeling sediment transport in ice-walled subglacial channels and its implications for esker 1090 formation and proglacial sediment yields, *Journal of Geophysical Research: Earth Surface*, 123, 3206–3227, 2018.

Boswell, S. M., Toucanne, S., Pitel-Roudaut, M., Creyts, T. T., Eynaud, F., and Bayon, G.: Enhanced surface melting of the Fennoscandian Ice Sheet during periods of North Atlantic cooling, *Geology*, 47, 664–668, 2019.

Boulton, G. and Jones, A.: Stability of temperate ice caps and ice sheets resting on beds of deformable sediment, *Journal of Glaciology*, 24, 29–43, 1979.

1095 Boulton, G., Lunn, R., Vidstrand, P., and Zatsepин, S.: Subglacial drainage by groundwater-channel coupling, and the origin of esker systems: part 1—glaciological observations, *Quaternary Science Reviews*, 26, 1067–1090, 2007a.

Boulton, G., Lunn, R., Vidstrand, P., and Zatsepин, S.: Subglacial drainage by groundwater-channel coupling, and the origin of esker systems: part II—theory and simulation of a modern system, *Quaternary Science Reviews*, 26, 1091–1105, 2007b.

Boulton, G., Haggdorn, M., Maillot, P., and Zatsepин, S.: Drainage beneath ice sheets: groundwater-channel coupling, and the origin of esker 1100 systems from former ice sheets, *Quaternary Science Reviews*, 28, 621–638, 2009.

Boulton, G. S., Dongelmans, P., Punkari, M., and Broadgate, M.: Palaeoglaciology of an ice sheet through a glacial cycle: the European ice sheet through the Weichselian, *Quaternary Science Reviews*, 20, 591–625, 2001.

Braithwaite, R. J. and Olesen, O. B.: Calculation of glacier ablation from air temperature, West Greenland, in: *Glacier Fluctuations and Climatic Change: Proceedings of the Symposium on Glacier Fluctuations and Climatic Change, held in Amsterdam, 1–5 June 1987*, pp. 219–233, Springer, 1989.

1105 Brennand, T. A.: Deglacial meltwater drainage and glaciodynamics: inferences from Laurentide eskers, Canada, *Geomorphology*, 32, 263–293, 2000.

Budd, W., Keage, P., and Blundy, N.: Empirical studies of ice sliding, *Journal of glaciology*, 23, 157–170, 1979.

Carter, S. P., Fricker, H. A., and Siegfried, M. R.: Antarctic subglacial lakes drain through sediment-floored canals: theory and model testing
1110 on real and idealized domains, *The Cryosphere*, 11, 381–405, 2017.

Chandler, D., Wadham, J., Lis, G., Cowton, T., Sole, A., Bartholomew, I., Telling, J., Nienow, P., Bagshaw, E., Mair, D., et al.: Evolution of
the subglacial drainage system beneath the Greenland Ice Sheet revealed by tracers, *Nature Geoscience*, 6, 195–198, 2013.

Chandler, D. M., Wadham, J. L., Nienow, P. W., Doyle, S. H., Tedstone, A. J., Telling, J., Hawkings, J., Alcock, J. D., Linhoff, B., and
Hubbard, A.: Rapid development and persistence of efficient subglacial drainage under 900 m-thick ice in Greenland, *Earth and Planetary
1115 Science Letters*, 566, 116 982, 2021.

Chapwanya, M., Clark, C. D., and Fowler, A. C.: Numerical computations of a theoretical model of ribbed moraine formation, *Earth Surface
Processes and Landforms*, 36, 1105–1112, 2011.

Chu, V. W.: Greenland ice sheet hydrology: A review, *Progress in Physical Geography*, 38, 19–54, 2014.

Chu, W., Creyts, T. T., and Bell, R. E.: Rerouting of subglacial water flow between neighboring glaciers in West Greenland, *Journal of
1120 Geophysical Research: Earth Surface*, 121, 925–938, 2016.

Clark, C. D., Knight, J. K., and Gray, J. T.: Geomorphological reconstruction of the Labrador sector of the Laurentide Ice Sheet, *Quaternary
Science Reviews*, 19, 1343–1366, 2000.

Clark, C. D., Chiverrell, R. C., Fabel, D., Hindmarsh, R. C., Ó Cofaigh, C., and Scourse, J. D.: Timing, pace and controls on ice sheet
retreat: an introduction to the BRITICE-CHRONO transect reconstructions of the British–Irish Ice Sheet, *Journal of Quaternary Science*,
1125 36, 673–680, 2021.

Clark, P. U. and Walder, J. S.: Subglacial drainage, eskers, and deforming beds beneath the Laurentide and Eurasian ice sheets, *Geological
Society of America Bulletin*, 106, 304–314, 1994.

Cofaigh, C. Ó.: Tunnel valley genesis, *Progress in physical geography*, 20, 1–19, 1996.

Cook, S., Christoffersen, P., Todd, J., Slater, D., and Chauché, N.: Integrated investigation of subglacial hydrology and convective plume
1130 melting using a 3D full-Stokes model of Store Glacier, West Greenland., in: *Geophysical Research Abstracts*, vol. 21, 2019.

Cook, S. J., Christoffersen, P., Todd, J., Slater, D., and Chauché, N.: Coupled modelling of subglacial hydrology and calving-front melting
at Store Glacier, West Greenland, *The Cryosphere*, 14, 905–924, 2020.

Cook, S. J., Christoffersen, P., and Todd, J.: A fully-coupled 3D model of a large Greenlandic outlet glacier with evolving subglacial hydrology,
frontal plume melting and calving, *Journal of Glaciology*, 68, 486–502, 2022.

1135 Coughlan, M., Tóth, Z., Van Landeghem, K. J., Mccarron, S., and Wheeler, A. J.: Formational history of the Wicklow Trough: a marine-
transgressed tunnel valley revealing ice flow velocity and retreat rates for the largest ice stream draining the late-Devensian British–Irish
Ice Sheet, *Journal of Quaternary Science*, 35, 907–919, 2020.

Cowton, T., Nienow, P., Sole, A., Wadham, J., Lis, G., Bartholomew, I., Mair, D., and Chandler, D.: Evolution of drainage system morphology
at a land-terminating Greenlandic outlet glacier, *Journal of Geophysical Research: Earth Surface*, 118, 29–41, 2013.

1140 Cuffey, K. M. and Paterson, W. S. B.: *The physics of glaciers*, Academic Press, 2010.

Cuzzone, J. K., Schlegel, N.-J., Morlighem, M., Larour, E., Briner, J. P., Seroussi, H., and Caron, L.: The impact of model resolution on
the simulated Holocene retreat of the southwestern Greenland ice sheet using the Ice Sheet System Model (ISSM), *The Cryosphere*, 13,
879–893, 2019.

Davison, B. J., Sole, A. J., Livingstone, S. J., Cowton, T. R., and Nienow, P. W.: The influence of hydrology on the dynamics of land-
1145 terminating sectors of the Greenland ice sheet, *Frontiers in Earth Science*, 7, 10, 2019.

De Fleurian, B., Morlighem, M., Seroussi, H., Rignot, E., van den Broeke, M. R., Kuipers Munneke, P., Mouginot, J., Smeets, P. C., and Tedstone, A. J.: A modeling study of the effect of runoff variability on the effective pressure beneath Russell Glacier, West Greenland, *Journal of Geophysical Research: Earth Surface*, 121, 1834–1848, 2016.

Dewald, N., Lewington, E. L., Livingstone, S. J., Clark, C. D., and Storrar, R. D.: Distribution, characteristics and formation of esker 1150 enlargements, *Geomorphology*, 392, 107919, 2021.

Dewald, N., Livingstone, S. J., and Clark, C. D.: Subglacial meltwater routes of the Fennoscandian Ice Sheet, *Journal of Maps*, 18, 382–396, 2022.

Donner, J.: The Younger Dryas age of the Salpausselkä moraines in Finland, *Bulletin of the Geological Society of Finland*, 82, 69–80, 2010.

Dow, C., Werder, M., Nowicki, S., and Walker, R.: Modeling Antarctic subglacial lake filling and drainage cycles., *Cryosphere Discussions*, 1155 9, 2015.

Dow, C., McCormack, F., Young, D., Greenbaum, J., Roberts, J., and Blankenship, D.: Totten Glacier subglacial hydrology determined from geophysics and modeling, *Earth and Planetary Science Letters*, 531, 115961, 2020.

Dow, C., Ross, N., Jeofry, H., Siu, K., and Siegert, M.: Antarctic basal environment shaped by high-pressure flow through a subglacial river system, *Nature Geoscience*, 15, 892–898, 2022.

Dow, C. F.: The role of subglacial hydrology in Antarctic ice sheet dynamics and stability: a modelling perspective, *Annals of Glaciology*, 1160 pp. 1–6, 2023.

Dow, C. F., Karlsson, N. B., and Werder, M. A.: Limited impact of subglacial supercooling freeze-on for Greenland ice sheet stratigraphy, *Geophysical Research Letters*, 45, 1481–1489, 2018a.

Dow, C. F., Lee, W. S., Greenbaum, J. S., Greene, C. A., Blankenship, D. D., Poinar, K., Forrest, A. L., Young, D. A., and Zappa, C. J.: Basal 1165 channels drive active surface hydrology and transverse ice shelf fracture, *Science Advances*, 4, eaao7212, 2018b.

Dow, C. F., Werder, M., Babonis, G., Nowicki, S., Walker, R. T., Csathó, B., and Morlighem, M.: Dynamics of active subglacial lakes in Recovery Ice Stream, *Journal of Geophysical Research: Earth Surface*, 123, 837–850, 2018c.

Doyle, S. H., Hubbard, B., Christoffersen, P., Young, T. J., Hofstede, C., Bougamont, M., Box, J., and Hubbard, A.: Physical conditions of 1170 fast glacier flow: 1. Measurements from boreholes drilled to the bed of Store Glacier, West Greenland, *Journal of Geophysical Research: Earth Surface*, 123, 324–348, 2018.

Doyle, S. H., Hubbard, B., Christoffersen, P., Law, R., Hewitt, D. R., Neufeld, J. A., Schoonman, C. M., Chudley, T. R., and Bougamont, M.: Water flow through sediments and at the ice-sediment interface beneath Sermeq Kujalleq (Store Glacier), Greenland, *Journal of Glaciology*, 68, 665–684, 2022.

Ehrenfeucht, S., Morlighem, M., Rignot, E., Dow, C. F., and Mouginot, J.: Seasonal acceleration of Petermann Glacier, Greenland, from 1175 changes in subglacial hydrology, *Geophysical Research Letters*, 50, e2022GL098009, 2023.

Fausto, R. S., Ahlstrøm, A. P., Van As, D., and Steffen, K.: Present-day temperature standard deviation parameterization for Greenland, *Journal of Glaciology*, 57, 1181–1183, 2011.

Flowers, G. E.: Hydrology and the future of the Greenland Ice Sheet, *Nature communications*, 9, 2729, 2018.

Fowler, A.: The formation of subglacial streams and mega-scale glacial lineations, *Proceedings of the Royal Society A: Mathematical, 1180 Physical and Engineering Sciences*, 466, 3181–3201, 2010.

Fowler, A. C. and Chapwanya, M.: An instability theory for the formation of ribbed moraine, drumlins and mega-scale glacial lineations, *Proceedings of the Royal Society A: Mathematical, Physical and Engineering Sciences*, 470, 20140185, 2014.

Gagliardini, O. and Werder, M. A.: Influence of increasing surface melt over decadal timescales on land-terminating Greenland-type outlet glaciers, *Journal of Glaciology*, 64, 700–710, 2018.

1185 Gardner, A. S., Sharp, M. J., Koerner, R. M., Labine, C., Boon, S., Marshall, S. J., Burgess, D. O., and Lewis, D.: Near-surface temperature lapse rates over Arctic glaciers and their implications for temperature downscaling, *Journal of Climate*, 22, 4281–4298, 2009.

Greenwood, S. L., Clason, C. C., Helanow, C., and Margold, M.: Theoretical, contemporary observational and palaeo-perspectives on ice sheet hydrology: processes and products, *Earth-Science Reviews*, 155, 1–27, 2016.

Greenwood, S. L., Clason, C. C., Nyberg, J., Jakobsson, M., and Holmlund, P.: The Bothnian Sea ice stream: early Holocene retreat dynamics of the south-central Fennoscandian Ice Sheet, *Boreas*, 46, 346–362, 2017.

1190 GTK, Finland: Superficial deposits of Finland 1:200 000 (sediment polygons), https://tupa GTK.fi/paikkatieto/meta/maapera_200k.html#tun_nistamistiedo, 2010.

Hager, A. O., Hoffman, M. J., Price, S. F., and Schroeder, D. M.: Persistent, extensive channelized drainage modeled beneath Thwaites Glacier, West Antarctica, *The Cryosphere*, 16, 3575–3599, 2022.

1195 Harper, J., Meierbacholt, T., Humphrey, N., Saito, J., and Stansberry, A.: Generation and fate of basal meltwater during winter, western Greenland Ice Sheet, *The Cryosphere*, 15, 5409–5421, 2021.

Hayden, A.-M. and Dow, C. F.: Examining the effect of ice dynamic changes on subglacial hydrology through modelling of a synthetic Antarctic glacier, *Journal of Glaciology*, pp. 1–14, 2023.

Hepburn, A., Dow, C., Ojala, A., Mäkinen, J., Ahokangas, E., Hovikoski, J., Jukka-Pekka, P., and Kajuutti, K.: Supplementary material for 'Reorganisation of subglacial drainage processes during rapid melting of the Fennoscandian Ice Sheet', <https://doi.org/10.5281/zenodo.8344208>, 2023.

1200 Hewitt, I. J.: Modelling distributed and channelized subglacial drainage: the spacing of channels, *Journal of Glaciology*, 57, 302–314, 2011.

Hewitt, I. J. and Creyts, T. T.: A model for the formation of eskers, *Geophysical Research Letters*, 46, 6673–6680, 2019.

Hoffman, M. J., Andrews, L. C., Price, S. F., Catania, G. A., Neumann, T. A., Lüthi, M. P., Gulley, J., Ryser, C., Hawley, R. L., and Morris, B.: Greenland subglacial drainage evolution regulated by weakly connected regions of the bed, *Nature communications*, 7, 13 903, 2016.

1205 Hooke, R. L.: Englacial and subglacial hydrology: a qualitative review, *Arctic and Alpine Research*, 21, 221–233, 1989.

Hooke, R. L. and Fastook, J.: Thermal conditions at the bed of the Laurentide ice sheet in Maine during deglaciation: implications for esker formation, *Journal of Glaciology*, 53, 646–658, 2007.

Hooke, R. L. and Jennings, C. E.: On the formation of the tunnel valleys of the southern Laurentide ice sheet, *Quaternary Science Reviews*, 25, 1364–1372, 2006.

1210 Hovikoski, J., Mäkinen, J., Winsemann, J., Soini, S., Kajuutti, K., Hepburn, A., and Ojala, A.: Upper-flow regime bedforms in a subglacial triangular-shaped landform (murtoo), late Pleistocene, SW Finland: Implications for flow dynamics and sediment transport in (semi-) distributed subglacial meltwater drainage systems, *Sedimentary Geology*, p. 106448, 2023.

Hubbard, B., Sharp, M., Willis, I., Nielsen, M., and Smart, C.: Borehole water-level variations and the structure of the subglacial hydrological system of Haut Glacier d'Arolla, Valais, Switzerland, *Journal of Glaciology*, 41, 572–583, 1995.

1215 Hughes, A. L., Gyllencreutz, R., Lohne, Ø. S., Mangerud, J., and Svendsen, J. I.: The last Eurasian ice sheets—a chronological database and time-slice reconstruction, DATED-1, *Boreas*, 45, 1–45, 2016.

Iken, A. and Bindschadler, R. A.: Combined measurements of subglacial water pressure and surface velocity of Findelengletscher, Switzerland: conclusions about drainage system and sliding mechanism, *Journal of Glaciology*, 32, 101–119, 1986.

1220 Indrigo, C., Dow, C. F., Greenbaum, J. S., and Morlighem, M.: Drygalski Ice Tongue stability influenced by rift formation and ice morphology, *Journal of Glaciology*, 67, 243–252, 2021.

1225 Iverson, N. R., Baker, R. W., Hooke, R. L., Hanson, B., and Jansson, P.: Coupling between a glacier and a soft bed: I. A relation between effective pressure and local shear stress determined from till elasticity, *Journal of Glaciology*, 45, 31–40, 1999.

Johansson, P., Kujansuu, R., Eriksson, B., Grönlund, T., Johansson, P., Kejonen, A., Kujansuu, R., Maunu, M., Mäkinen, K., Saarnisto, M., et al.: Pohjois-Suomen maaperä: maaperäkarttojen 1: 400 000 selitys, Summary: Quaternary deposits of Northern Finland—Explanation to the maps of Quaternary deposits, 1, 000, 2005.

Johnsen, S. J., Clausen, H. B., Dansgaard, W., Gundestrup, N. S., Hammer, C. U., Andersen, U., Andersen, K. K., Hvidberg, C. S., Dahl-Jensen, D., Steffensen, J. P., et al.: The $\delta^{18}\text{O}$ record along the Greenland Ice Core Project deep ice core and the problem of possible Eemian climatic instability, *Journal of Geophysical Research: Oceans*, 102, 26 397–26 410, 1997.

1230 Joughin, I., Das, S. B., King, M. A., Smith, B. E., Howat, I. M., and Moon, T.: Seasonal speedup along the western flank of the Greenland Ice Sheet, *Science*, 320, 781–783, 2008.

Kamb, B.: Glacier surge mechanism based on linked cavity configuration of the basal water conduit system, *Journal of Geophysical Research: Solid Earth*, 92, 9083–9100, 1987.

1235 Karlsson, N. B. and Dahl-Jensen, D.: Response of the large-scale subglacial drainage system of Northeast Greenland to surface elevation changes, *The Cryosphere*, 9, 1465–1479, 2015.

Karlsson, N. B., Solgaard, A. M., Mankoff, K. D., Gillet-Chaulet, F., MacGregor, J. A., Box, J. E., Citterio, M., Colgan, W. T., Larsen, S. H., Kjeldsen, K. K., et al.: A first constraint on basal melt-water production of the Greenland ice sheet, *Nature Communications*, 12, 3461, 2021.

1240 Killingbeck, S. F., Booth, A. D., Livermore, P. W., Bates, C. R., and West, L. J.: Characterisation of subglacial water using a constrained transdimensional Bayesian transient electromagnetic inversion, *Solid Earth*, 11, 75–94, 2020.

Kirkham, J. D., Hogan, K. A., Larter, R. D., Arnold, N. S., Ely, J. C., Clark, C. D., Self, E., Games, K., Huuse, M., Stewart, M. A., et al.: Tunnel valley formation beneath deglaciating mid-latitude ice sheets: Observations and modelling, *Quaternary Science Reviews*, p. 107680, 2022.

1245 Kleman, J., Hättestrand, C., Borgström, I., and Stroeven, A.: Fennoscandian palaeoglaciology reconstructed using a glacial geological inversion model, *Journal of glaciology*, 43, 283–299, 1997.

Larour, E., Seroussi, H., Morlighem, M., and Rignot, E.: Continental scale, high order, high spatial resolution, ice sheet modeling using the Ice Sheet System Model (ISSM), *Journal of Geophysical Research: Earth Surface*, 117, 2012.

Lehtinen, M., Nurmi, P. A., and Ramo, O.: *Precambrian Geology of Finland*, Elsevier, 2005.

1250 Lewington, E. L., Livingstone, S. J., Sole, A. J., Clark, C. D., and Ng, F. S.: An automated method for mapping geomorphological expressions of former subglacial meltwater pathways (hummock corridors) from high resolution digital elevation data, *Geomorphology*, 339, 70–86, 2019.

Lewington, E. L., Livingstone, S. J., Clark, C. D., Sole, A. J., and Storrar, R. D.: A model for interaction between conduits and surrounding hydraulically connected distributed drainage based on geomorphological evidence from Keewatin, Canada, *The Cryosphere*, 14, 2949–2976, 2020.

1255 Livingstone, S., Clark, C., Woodward, J., and Kingslake, J.: Potential subglacial lakes and meltwater drainage pathways beneath the Antarctic and Greenland ice sheets, *The Cryosphere*, 7, 1721–1740, 2013a.

Livingstone, S. J., Clark, C. D., and Tarasov, L.: Modelling North American palaeo-subglacial lakes and their meltwater drainage pathways, *Earth and Planetary Science Letters*, 375, 13–33, 2013b.

Livingstone, S. J., Storrar, R. D., Hillier, J. K., Stokes, C. R., Clark, C. D., and Tarasov, L.: An ice-sheet scale comparison of eskers with 1260 modelled subglacial drainage routes, *Geomorphology*, 246, 104–112, 2015.

Lunkka, J. P. and Erikkilä, A.: Behaviour of the lake district ice lobe of the Scandinavian ice sheet during the younger dryas chronozone (ca. 12 800–11 500 years ago), *Tech. rep.*, Posiva Oy, 2012.

Lunkka, J. P., Johansson, P., Saarnisto, M., and Sallasmaa, O.: Glaciation of Finland, in: *Developments in Quaternary Sciences*, vol. 2, pp. 93–100, Elsevier, 2004.

1265 Lunkka, J. P., Palmu, J.-P., and Seppänen, A.: Deglaciation dynamics of the Scandinavian Ice Sheet in the Salpausselkä zone, southern Finland, *Boreas*, 50, 404–418, 2021.

MacAyeal, D. R.: Large-scale ice flow over a viscous basal sediment: Theory and application to ice stream B, Antarctica, *Journal of Geophysical Research: Solid Earth*, 94, 4071–4087, 1989.

Mair, D., Nienow, P., Sharp, M., Wohlleben, T., and Willis, I.: Influence of subglacial drainage system evolution on glacier surface motion: 1270 Haut Glacier d’Arolla, Switzerland, *Journal of Geophysical Research: Solid Earth*, 107, EPM–8, 2002.

Mair, D., Willis, I., Fischer, U. H., Hubbard, B., Nienow, P., and Hubbard, A.: Hydrological controls on patterns of surface, internal and basal motion during three “spring events”: Haut Glacier d’Arolla, Switzerland, *Journal of Glaciology*, 49, 555–567, 2003.

Mäkinen, J.: Time-transgressive deposits of repeated depositional sequences within interlobate glaciofluvial (esker) sediments in Köyliö, SW Finland, *Sedimentology*, 50, 327–360, 2003.

1275 Mäkinen, J., Kajuutti, K., Palmu, J.-P., Ojala, A., and Ahokangas, E.: Triangular-shaped landforms reveal subglacial drainage routes in SW Finland, *Quaternary Science Reviews*, 164, 37–53, 2017.

Mäkinen, J., Kajuutti, K., Ojala, A. E., Ahokangas, E., Tuunainen, A., Valkama, M., and Palmu, J.-P.: Genesis of subglacial triangular-shaped landforms (murtoos) formed by the Fennoscandian Ice Sheet, *Earth Surface Processes and Landforms*, 2023.

Mangerud, J., Hughes, A. L., Johnson, M. D., and Lunkka, J. P.: The Fennoscandian Ice Sheet during the Younger Dryas Stadial, in: *European 1280 Glacial landscapes*, pp. 437–452, Elsevier, 2023.

Marshall, S. J. and Sharp, M. J.: Temperature and melt modeling on the Prince of Wales ice field, Canadian High Arctic, *Journal of Climate*, 22, 1454–1468, 2009.

McArthur, K., McCormack, F. S., and Dow, C. F.: Basal conditions of Denman Glacier from glacier hydrology and ice dynamics modeling, *The Cryosphere Discussions*, pp. 1–29, 2023.

1285 Meierbachtol, T., Harper, J., and Humphrey, N.: Basal drainage system response to increasing surface melt on the Greenland ice sheet, *Science*, 341, 777–779, 2013.

Moon, T., Joughin, I., Smith, B., Van Den Broeke, M. R., Van De Berg, W. J., Noël, B., and Usher, M.: Distinct patterns of seasonal Greenland glacier velocity, *Geophysical research letters*, 41, 7209–7216, 2014.

Morlighem, M., Williams, C. N., Rignot, E., An, L., Arndt, J. E., Bamber, J. L., Catania, G., Chauché, N., Dowdeswell, J. A., Dorschel, B., 1290 et al.: BedMachine v3: Complete bed topography and ocean bathymetry mapping of Greenland from multibeam echo sounding combined with mass conservation, *Geophysical research letters*, 44, 11–051, 2017.

Morlighem, M., Rignot, E., Binder, T., Blankenship, D., Drews, R., Eagles, G., Eisen, O., Ferraccioli, F., Forsberg, R., Fretwell, P., et al.: Deep glacial troughs and stabilizing ridges unveiled beneath the margins of the Antarctic ice sheet, *Nature Geoscience*, 13, 132–137, 2020.

1295 Nick, F. M., Vieli, A., Andersen, M. L., Joughin, I., Payne, A., Edwards, T. L., Pattyn, F., and van de Wal, R. S.: Future sea-level rise from Greenland's main outlet glaciers in a warming climate, *Nature*, 497, 235–238, 2013.

Nienow, P., Sharp, M., and Willis, I.: Seasonal changes in the morphology of the subglacial drainage system, *Haut Glacier d'Arolla*, Switzerland, *Earth Surface Processes and Landforms: The Journal of the British Geomorphological Group*, 23, 825–843, 1998.

Nienow, P., Sole, A., Slater, D. A., and Cowton, T.: Recent advances in our understanding of the role of meltwater in the Greenland Ice Sheet system, *Current Climate Change Reports*, 3, 330–344, 2017.

1300 Nye, J.: Water at the bed of a glacier, in: *International Glaciological Society*, pp. 189–194, 1972.

Ojala, A. E., Palmu, J.-P., Åberg, A., Åberg, S., and Virkki, H.: Development of an ancient shoreline database to reconstruct the Litorina Sea maximum extension and the highest shoreline of the Baltic Sea basin in Finland, *Bulletin of the Geological Society of Finland*, 2013.

Ojala, A. E., Peterson Becher, G., Mäkinen, J., Johnson, M. D., Kajuutti, K., Palmu, J.-P., Ahokangas, E., and Öhrling, C.: Ice-sheet scale distribution and morphometry of triangular-shaped hummocks (murtoos): a subglacial landform produced during rapid retreat of the 1305 Scandinavian Ice Sheet, *Annals of Glaciology*, 60, 115–126, 2019.

Ojala, A. E., Mäkinen, J., Ahokangas, E., Kajuutti, K., Valkama, M., Tuunainen, A., and Palmu, J.-P.: Diversity of murtoos and murtoo-related subglacial landforms in the Finnish area of the Fennoscandian Ice Sheet, *Boreas*, 50, 1095–1115, 2021.

Ojala, A. E., Mäkinen, J., Kajuutti, K., Ahokangas, E., and Palmu, J.-P.: Subglacial evolution from distributed to channelized drainage: evidence from the Lake Murtoo area in SW Finland, *Earth Surface Processes and Landforms*, 47, 2877–2896, 2022.

1310 Palmu, J.-P., Ojala, A. E., Virtasalo, J., Putkinen, N., Kohonen, J., and Sarala, P.: Classification system of superficial (quaternary) geological units in Finland, *Developments in Map Data Management and Geological Unit Nomenclature in Finland*, 412, 115–169, 2021.

Patton, H., Hubbard, A., Andreassen, K., Auriac, A., Whitehouse, P. L., Stroeven, A. P., Shackleton, C., Winsborrow, M., Heyman, J., and Hall, A. M.: Deglaciation of the Eurasian ice sheet complex, *Quaternary Science Reviews*, 169, 148–172, 2017.

Peterson Becher, G. and Johnson, M. D.: Sedimentology and internal structure of murtoos-V-shaped landforms indicative of a dynamic 1315 subglacial hydrological system, *Geomorphology*, 380, 107 644, 2021.

Peterson Becher, G., Johnson, M. D., and Smith, C. A.: Glacial geomorphology of the south Swedish uplands—focus on the spatial distribution of hummock tracts, *Journal of Maps*, 13, 534–544, 2017.

Poinar, K., Dow, C. F., and Andrews, L. C.: Long-term support of an active subglacial hydrologic system in Southeast Greenland by firn aquifers, *Geophysical Research Letters*, 46, 4772–4781, 2019.

1320 Punkari, M.: The ice lobes of the Scandinavian ice sheet during the deglaciation in Finland., *Boreas*, 9, 307–310, 1980.

Punkari, M.: Subglacial processes of the Scandinavian Ice Sheet in Fennoscandia inferred from flow-parallel features and lithostratigraphy, *Sedimentary Geology*, 111, 263–283, 1997.

Putkinen, N., Eyles, N., Putkinen, S., Ojala, A. E., Palmu, J.-P., Sarala, P., Väänänen, T., Räisänen, J., Saarelainen, J., Ahtonen, N., et al.: High-resolution LiDAR mapping of glacial landforms and ice stream lobes in Finland., *Bulletin of the Geological Society of Finland*, 89, 1325 2017.

Rada, C. and Schoof, C.: Channelized, distributed, and disconnected: subglacial drainage under a valley glacier in the Yukon, *The Cryosphere*, 12, 2609–2636, 2018.

Rampton, V.: Large-scale effects of subglacial meltwater flow in the southern Slave Province, Northwest Territories, Canada, *Canadian Journal of Earth Sciences*, 37, 81–93, 2000.

1330 Regnell, C., Mangerud, J., and Svendsen, J. I.: Tracing the last remnants of the Scandinavian Ice Sheet: Ice-dammed lakes and a catastrophic outburst flood in northern Sweden, *Quaternary Science Reviews*, 221, 105 862, 2019.

Rosentau, A., Klemann, V., Bennike, O., Steffen, H., Wehr, J., Latinović, M., Bagge, M., Ojala, A., Berglund, M., Peterson Becher, G., et al.: A Holocene relative sea-level database for the Baltic Sea, *Quaternary Science Reviews*, 266, 107 071, 2021.

Röthlisberger, H.: Water pressure in intra-and subglacial channels, *Journal of Glaciology*, 11, 177–203, 1972.

1335 Salonen, V.-P.: Glacial transport distance distributions of surface boulders in Finland, *Bulletin-Geological survey of Finland*, 1986.

Schenk, F., Välimäki, M., Muschitiello, F., Tarasov, L., Heikkilä, M., Björck, S., Brandefelt, J., Johansson, A. V., Näslund, J.-O., and Wohlfarth, B.: Warm summers during the Younger Dryas cold reversal, *Nature Communications*, 9, 1634, 2018.

Scholzen, C., Schuler, T. V., and Gilbert, A.: Sensitivity of subglacial drainage to water supply distribution at the Kongsfjord basin, Svalbard, *The Cryosphere*, 15, 2719–2738, 2021.

1340 Schoof, C.: The effect of cavitation on glacier sliding, *Proceedings of the Royal Society A: Mathematical, Physical and Engineering Sciences*, 461, 609–627, 2005.

Schoof, C.: Ice-sheet acceleration driven by melt supply variability, *Nature*, 468, 803–806, 2010.

Shackleton, C., Patton, H., Hubbard, A., Winsborrow, M., Kingslake, J., Esteves, M., Andreassen, K., and Greenwood, S. L.: Subglacial water storage and drainage beneath the Fennoscandian and Barents Sea ice sheets, *Quaternary Science Reviews*, 201, 13–28, 2018.

1345 Sole, A., Nienow, P., Bartholomew, I., Mair, D., Cowton, T., Tedstone, A., and King, M. A.: Winter motion mediates dynamic response of the Greenland Ice Sheet to warmer summers, *Geophysical Research Letters*, 40, 3940–3944, 2013.

Sole, A. J., Mair, D. W. F., Nienow, P. W., Bartholomew, I., King, M., Burke, M. J., and Joughin, I.: Seasonal speedup of a Greenland marine-terminating outlet glacier forced by surface melt-induced changes in subglacial hydrology, *Journal of Geophysical Research: Earth Surface*, 116, 2011.

1350 Sommers, A., Rajaram, H., and Morlighem, M.: SHAKTI: subglacial hydrology and kinetic, transient interactions v1. 0, *Geoscientific Model Development*, 11, 2955–2974, 2018.

Sommers, A., Meyer, C., Morlighem, M., Rajaram, H., Poinar, K., Chu, W., and Mejia, J.: Subglacial hydrology modeling predicts high winter water pressure and spatially variable transmissivity at Helheim Glacier, Greenland, *Journal of Glaciology*, pp. 1–13, 2022.

Stokes, C. R., Fowler, A. C., Clark, C. D., Hindmarsh, R. C., and Spagnolo, M.: The instability theory of drumlin formation and its explanation 1355 of their varied composition and internal structure, *Quaternary Science Reviews*, 62, 77–96, 2013.

Storrar, R. D. and Livingstone, S. J.: Glacial geomorphology of the northern Kivalliq region, Nunavut, Canada, with an emphasis on meltwater drainage systems, *Journal of Maps*, 13, 153–164, 2017.

Storrar, R. D., Stokes, C. R., and Evans, D. J.: Increased channelization of subglacial drainage during deglaciation of the Laurentide Ice Sheet, *Geology*, 42, 239–242, 2014.

1360 Stroeven, A. P., Hättestrand, C., Kleman, J., Heyman, J., Fabel, D., Fredin, O., Goodfellow, B. W., Harbor, J. M., Jansen, J. D., Olsen, L., et al.: Deglaciation of fennoscandia, *Quaternary Science Reviews*, 147, 91–121, 2016.

Tedstone, A. J., Nienow, P. W., Gourmelen, N., Dehecq, A., Goldberg, D., and Hanna, E.: Decadal slowdown of a land-terminating sector of the Greenland Ice Sheet despite warming, *Nature*, 526, 692–695, 2015.

Tuckett, P. A., Ely, J. C., Sole, A. J., Livingstone, S. J., Davison, B. J., Melchior van Wessem, J., and Howard, J.: Rapid accelerations of 1365 Antarctic Peninsula outlet glaciers driven by surface melt, *Nature Communications*, 10, 4311, 2019.

Utting, D. J., Ward, B. C., and Little, E. C.: Genesis of hummocks in glaciofluvial corridors near the Keewatin Ice Divide, Canada, *Boreas*, 38, 471–481, 2009.

Van Boeckel, M., Van Boeckel, T., and Hall, A. M.: Late erosion pulse triggered by rapid melt in the cold-based interior of the last Fennoscandian Ice Sheet, an example from Rogen, *Earth Surface Processes and Landforms*, 47, 3376–3394, 2022.

1370 Van de Wal, R., Smeets, C., Boot, W., Stoffelen, M., Van Kampen, R., Doyle, S. H., Wilhelms, F., van den Broeke, M. R., Reijmer, C., Oerlemans, J., et al.: Self-regulation of ice flow varies across the ablation area in south-west Greenland, *The Cryosphere*, 9, 603–611, 2015.

van den Broeke, M., Bus, C., Ettema, J., and Smeets, P.: Temperature thresholds for degree-day modelling of Greenland ice sheet melt rates, *Geophysical Research Letters*, 37, 2010.

1375 van den Broeke, M. R., Kuipers Munneke, P., Noël, B., Reijmer, C., Smeets, P., van de Berg, W. J., and van Wessem, J. M.: Contrasting current and future surface melt rates on the ice sheets of Greenland and Antarctica: Lessons from in situ observations and climate models, *PLOS Climate*, 2, e0000 203, 2023.

Vérité, J., Ravier, É., Bourgeois, O., Bessin, P., Livingstone, S. J., Clark, C. D., Pochat, S., and Mourges, R.: Formation of murtoos by repeated flooding of ribbed bedforms along subglacial meltwater corridors, *Geomorphology*, 408, 108 248, 2022.

1380 Vijay, S., King, M. D., Howat, I. M., Solgaard, A. M., Khan, S. A., and Noël, B.: Greenland ice-sheet wide glacier classification based on two distinct seasonal ice velocity behaviors, *Journal of Glaciology*, 67, 1241–1248, 2021.

Wake, L. and Marshall, S.: Assessment of current methods of positive degree-day calculation using in situ observations from glaciated regions, *Journal of Glaciology*, 61, 329–344, 2015.

Walder, J. S.: Hydraulics of subglacial cavities, *Journal of Glaciology*, 32, 439–445, 1986.

1385 Walder, J. S. and Fowler, A.: Channelized subglacial drainage over a deformable bed, *Journal of glaciology*, 40, 3–15, 1994.

Wallis, B. J., Hogg, A. E., van Wessem, J. M., Davison, B. J., and van den Broeke, M. R.: Widespread seasonal speed-up of west Antarctic Peninsula glaciers from 2014 to 2021, *Nature Geoscience*, 16, 231–237, 2023.

Weertman, J.: General theory of water flow at the base of a glacier or ice sheet, *Reviews of Geophysics*, 10, 287–333, 1972.

Werder, M. A., Hewitt, I. J., Schoof, C. G., and Flowers, G. E.: Modeling channelized and distributed subglacial drainage in two dimensions, *Journal of Geophysical Research: Earth Surface*, 118, 2140–2158, 2013.

1390 Willis, I. C., Richards, K. S., and Sharp, M. J.: Links between proglacial stream suspended sediment dynamics, glacier hydrology and glacier motion at Midtdalsbreen, Norway, *Hydrological Processes*, 10, 629–648, 1996.

Wright, P. J., Harper, J. T., Humphrey, N. F., and Meierbachtol, T. W.: Measured basal water pressure variability of the western Greenland Ice Sheet: Implications for hydraulic potential, *Journal of Geophysical Research: Earth Surface*, 121, 1134–1147, 2016.

1395 Yang, K. and Smith, L. C.: Internally drained catchments dominate supraglacial hydrology of the southwest Greenland Ice Sheet, *Journal of Geophysical Research: Earth Surface*, 121, 1891–1910, 2016.

Appendix A: Contents

This file contains supplementary information for ‘*Reorganisation of subglacial drainage processes during rapid melting of the Fennoscandian Ice Sheet*’

1400 **Movie A1.** Evolution of the system with respect to ~~overburden~~overburden% through time in the baseline model run. Model years 15–17 were arbitrarily chosen to illustrate the transient state of the system through several melt season cycles. Channels are shown as black lines where ~~discharge~~ Q_c exceeds $1 \text{ m}^3 \text{ s}^{-1}$.

Figure A1. The distribution of meltwater routes, murtoo routes, and sediment in the Finnish Lake District Ice Lobe. **A)** Meltwater routes and murtoo routes as mapped by Ahokangas et al. (2021). There is a general absence of murtoos in the 1405 centre of the lobe 40–60 km from the ice margin. **B)** Sediment cover (GTK, Finland, 2010) showing thin sediment thickness in the terrain from which murtoos appear absent.

Figure A2. Median ~~overburden~~overburden%, channel discharge, Q_c , and sheet discharge, q_s per timestep over the full length of the baseline model run.

Figure A3–A31. Comparison of the median summer system for the range of sensitivity parameters against the baseline model 1410 run. **A)** Water pressure expressed as a percentage of overburden pressure, ~~overburden~~overburden%. Channels are shown as black lines where median discharge exceeds $1 \text{ m}^3 \text{ s}^{-1}$. **B)** Baseline median summer ~~overburden~~overburden% minus the tested median summer ~~overburden~~overburden%. The same figure caption applies for Figures A3–A31.

Figure A32. Boxplots of model parameters grouped by month for overburden (~~overburden~~overburden%, **A**), sheet discharge (q_s , **B**), water velocity (V_w , **C**), and channel discharge (Q_c , **D**) during all model years at nodes between 40–60 km from 1415 the ice margin. As in Figure 5, nodes that fall within meltwater routes which do host murtoos (~~Murtoo-free MRs~~Murtoo routes) are shown in blue, nodes which fall within mapped meltwater routes that do not contain murtoo fields (~~Murtoo-hosting MRs~~meltwater routes) are shown in orange, and all other nodes are shown in purple. Medians for each group are shown as black circles, and ‘outliers’—defined as points more than 150% of the interquartile range away from the upper and lower quartile—are shown as crosses.

1420 **Tables A1–A4.** Tukey-Kramer HSD test results for ~~overburden~~overburden% (Table A1), q_s (Table A2), Q_c (Table A3), and V_w (Table A4) in meltwater routes, murtoo routes, and non-meltwater routes between 40–60 km from the ice margin. The upper and lower limits describe the 95% confidence intervals for the true mean difference, A–B is the difference between group means.

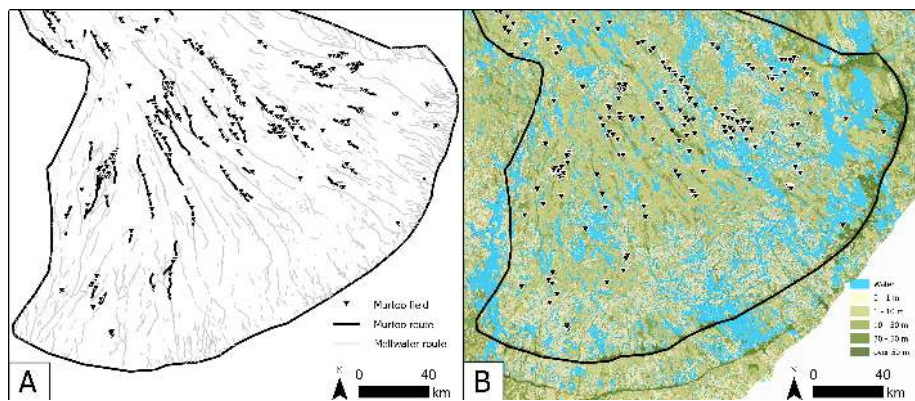


Figure A1. The distribution of meltwater routes, murto routes, and sediment in the Finnish Lake District Ice Lobe. **A)** Meltwater routes and murto routes as mapped by Ahokangas et al. (2021). There is a general absence of murtoos in the centre of the lobe 40–60 km from the ice margin. **B)** Sediment cover (GTK, Finland, 2010) showing thin sediment thickness in the terrain from which murtoos appear absent.

Table 1. Murtoo developmental stages (see Figure 10 in Hovikoski et al., 2023), their sedimentological signature, and anticipated model outcomes

Murtoo developmental stage	Sedimentological evidence and interpretation	Expected model outcomes
1	Sorted sediment core within rapidly enlarging cavity, partial ice contact	Sharp increases in g_s , increase in overburden%
2	Onset of spring melt, cavity continuing to enlarge, with deposition of sinusoidal stratification and cobbles	Peak in overburden%, continued increase in Q_c
3	Increasing grain size indicates high water velocity and boulder deposition indicates maximum cavity size	Peak in V_w , drop in overburden%, peak in Q_c approaching 1^2 within southern Finland, the FLDIL consists of a main trunk upstream of a lobate expansion. The lobate portion of the FLDIL is bound at its easternmost margin by the first and second Salpausselkäs (Figure 1A) large ice marginal complexes, which mark the Younger Dryas extent of the FIS in the region (Donner, 2010; Lunkka et al., 2021). Laterally the main trunk of the FLDIL abuts the Näsijärvi-Jyväskylä ice lobe to the southwest and the Oulu-North-Karelian ice lobe province to the northeast, as well as both the Päijänne and Middle Ostrobothnian interlobate regions (Putkinen et al., 2017; Palmu et al., 2021). The bedrock within the FLDIL and the wider FIS comprises predominantly crystalline bedrock, dominated by Precambrian schists, gneisses, and granitoids (Lehtinen et al., 2005) with a thin Quaternary overburden (Lunkka et al., 2021). Systematic mapping using LiDAR-derived digital elevation models (e.g., Putkinen et al., 2017) has revealed a high density of drumlins, mega-scale glacial lineations (MSGL), eskers and hummocky moraines in

Table 2. List of input values, values highlighted in bold indicate those used for sensitivity testing and a range of values is provided. List of input values for GlaDS, values highlighted in bold indicate those used for sensitivity testing and a range of values is provided. Note, in all instances *sheet* refers to the subglacial drainage system.

Symbol	Description	Default value	Tested range	Units
ρ_i	ice density	918		kg m^{-3}
ρ_w	water density	1000		kg m^{-3}
g	gravitational acceleration	9.81		m s^{-2}
n	Glen's flow law exponent	3		
a	basal friction coefficient	0–120		$(\text{Pa a}^{-1})^{1/2}$
A	rate factor	1.7×10^{-24}		$\text{s}^{-1} \text{Pa}^{-3}$
L	latent heat	3.34×10^5		J kg^{-1}
c_t	pressure melt coefficient	7.5×10^{-8}		KPa^{-1}
c_w	heat capacity of water	4.22×10^3		$\text{J kg}^{-1} \text{K}^{-1}$
α	first sheet flow exponent	$5/4$		
β	second sheet flow exponent	$3/2$		
α_c	first channel flow exponent	$5/4$		
β_c	second channel flow exponent	$3/2$		
k_s	sheet conductivity	10^{-4}	10^{-2} – 10^{-5}	$\text{m}^{7/4} \text{kg}^{-1/2}$
k_c	channel conductivity	0.1 – 10^{-1}	0.5 – 0.05 5×10^{-1} – 10^{-3}	$\text{m}^{3/2} \text{kg}^{-1/2}$
E_{vr}	englacial void ratio	10^{-4}	10^{-3} – 10^{-5}	
l_c	sheet width below channel	2		m
A_m	moulin cross-sectional area	10		m^2
l_r	cavity spacing	2		m
h_r	basal bump height	0.085	0.05–0.1	m
b_{melt}	basal melt rate	5×10^{-3}	1 – 7×10^{-3}	m yr^{-1}
U_b	mean annual velocity [†]	150	100–200	m yr^{-1}
N_{moulin}	number of moulin [*]	2500	1000–4000	

[†] We tested both a transient and temporally constant velocity within these given ranges for mean annual velocity

^{*} We also ran an experiment in which melt was routed directly to the bed at each node (SHEET)

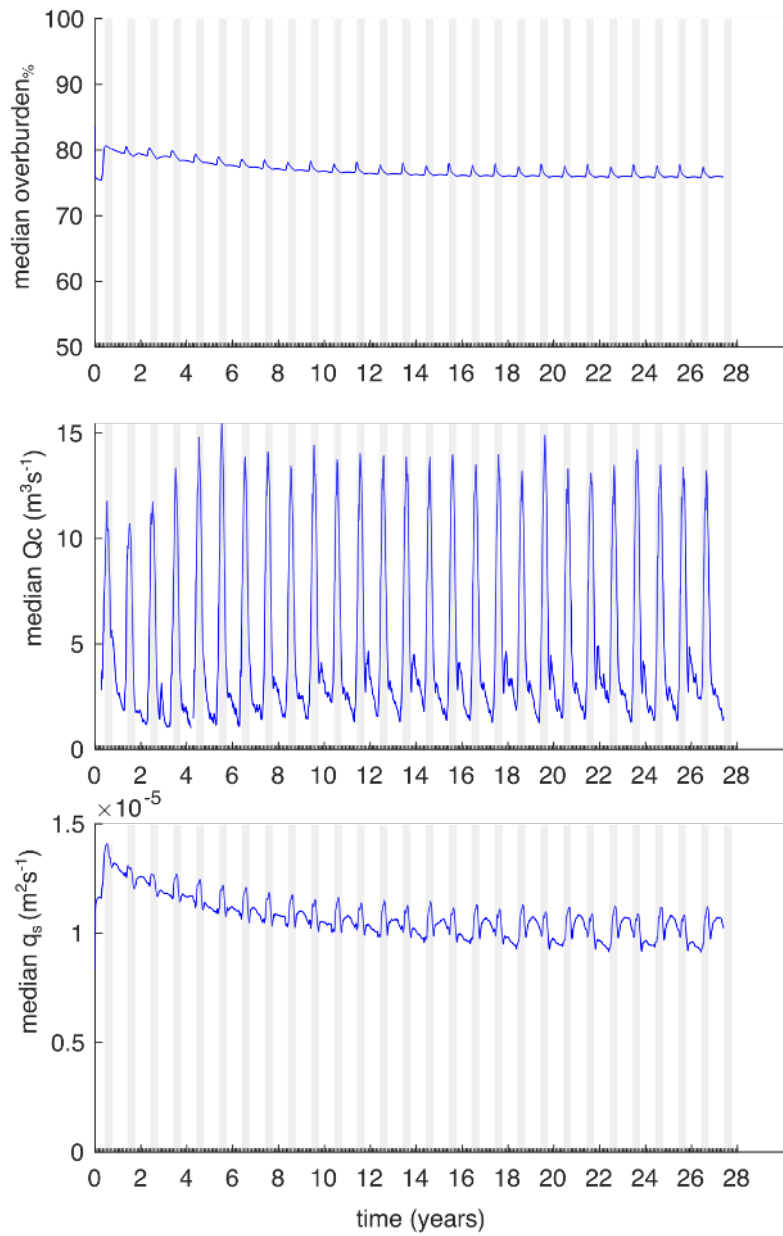


Figure A2. Median ~~overburden~~^{overburden}, channel discharge, Q_c , and sheet discharge, q_s over the full length of the baseline model run.

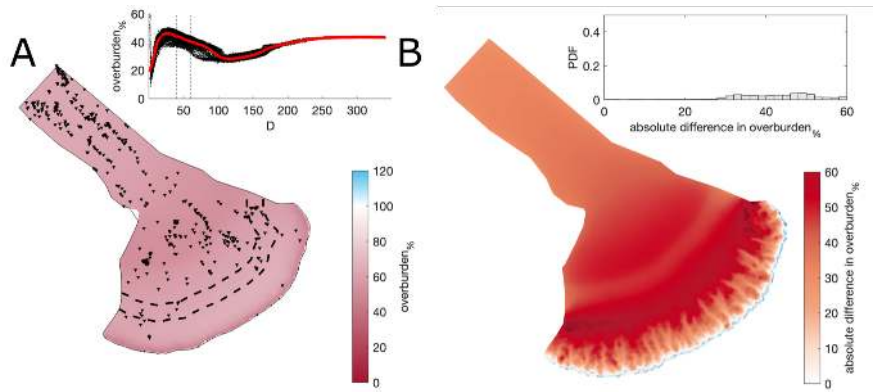


Figure A3. Comparison of the median summer system for sheet conductivity, $k_s = 10^{-2} \text{ m}^{7/4} \text{ kg}^{-1/2}$ against the baseline model run ($k_s = 10^{-4} \text{ m}^{7/4} \text{ kg}^{-1/2}$). **A**) Water pressure expressed as a percentage of overburden pressure, overburden%. **B**) Baseline median summer overburden% minus the $k_s = 10^{-2} \text{ m}^{7/4} \text{ kg}^{-1/2}$ median summer overburden%. The same figure caption applies for Figures A3–A31

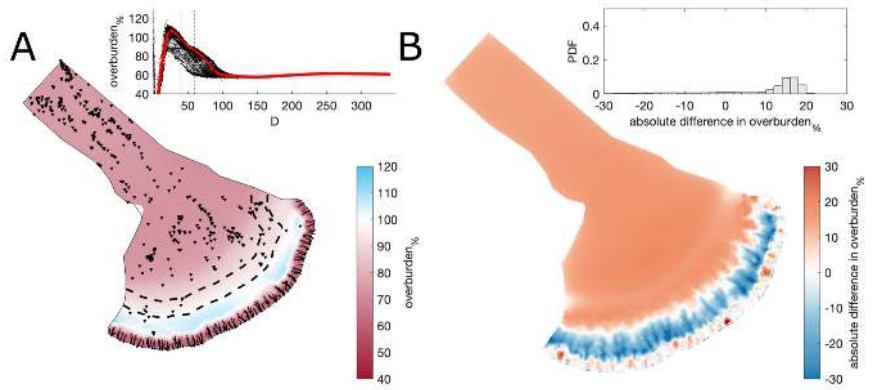


Figure A4. Comparison of the median summer system for sheet conductivity, $k_s = 10^{-3} \text{ m}^{7/4} \text{ kg}^{-1/2}$ against the baseline model run ($k_s = 10^{-4} \text{ m}^{7/4} \text{ kg}^{-1/2}$). The same figure caption as Figure A3 applies.

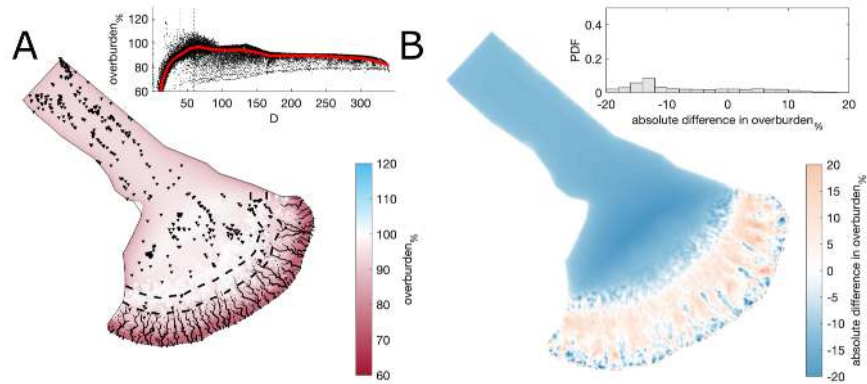


Figure A5. Comparison of the median summer system for sheet conductivity, $k_s = 10^{-5} \text{ m}^{7/4} \text{ kg}^{-1/2}$ against the baseline model run ($k_s = 10^{-4} \text{ m}^{7/4} \text{ kg}^{-1/2}$). The same figure caption as Figure A3 applies.

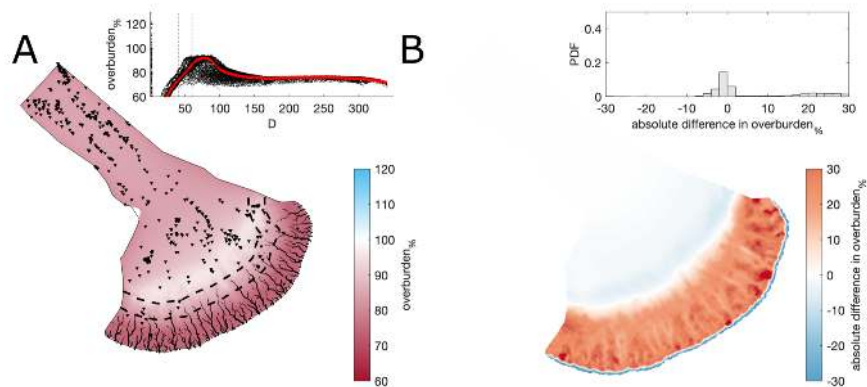


Figure A6. Comparison of the median summer system for channel conductivity, $k_c = 5 \times 10^{-1} \text{ m}^{3/2} \text{ kg}^{-1/2}$ against the baseline model run ($k_c = 10^{-1} \text{ m}^{3/2} \text{ kg}^{-1/2}$). The same figure caption as Figure A3 applies.

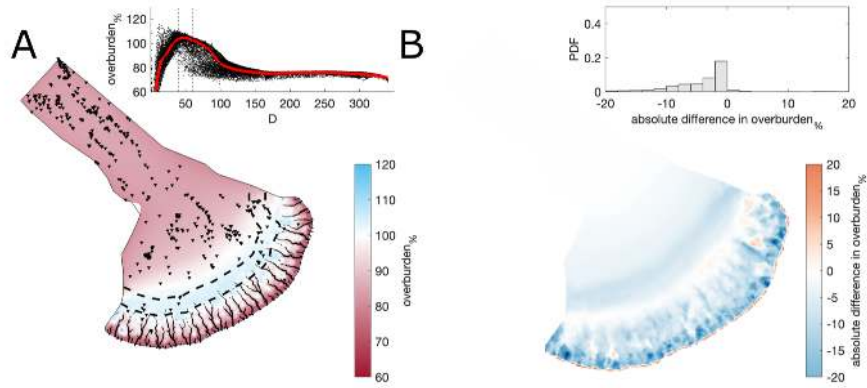


Figure A7. Comparison of the median summer system for channel conductivity, $k_c = 5 \times 10^{-2} \text{ m}^{3/2} \text{ kg}^{-1/2}$ against the baseline model run ($k_c = 10^{-1} \text{ m}^{3/2} \text{ kg}^{-1/2}$). The same figure caption as Figure A3 applies.

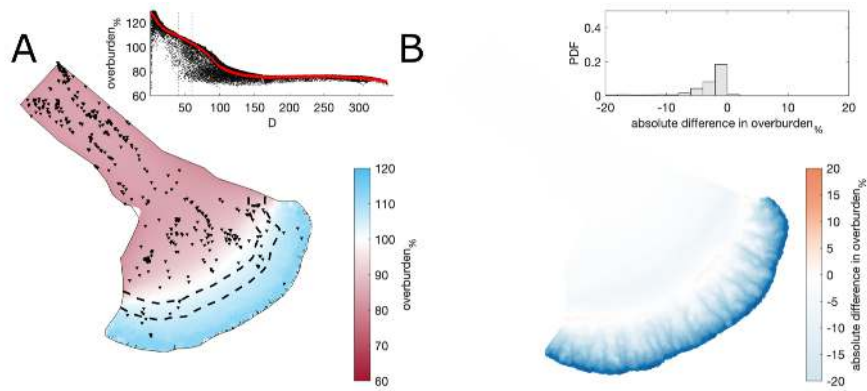


Figure A8. Comparison of the median summer system for channel conductivity, $k_c = 10^{-3} \text{ m}^{3/2} \text{ kg}^{-1/2}$ against the baseline model run ($k_c = 10^{-1} \text{ m}^{3/2} \text{ kg}^{-1/2}$). The same figure caption as Figure A3 applies.

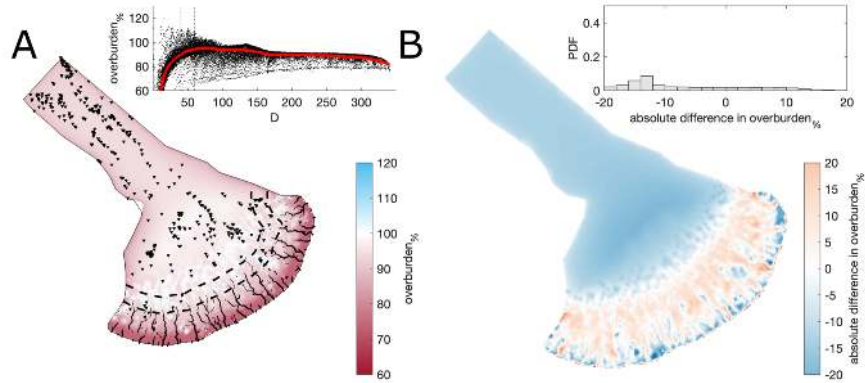


Figure A9. Comparison of the median summer system for moulin frequency, $N_{moulin} = 1000$ against the baseline model run ($N_{moulin} = 2500$). The same figure caption as Figure A3 applies.

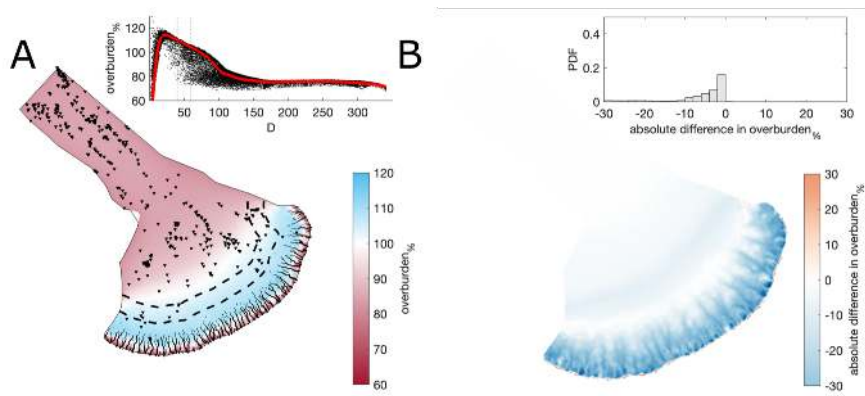


Figure A10. Comparison of the median summer system for moulin frequency, $N_{moulin} = 4000$ against the baseline model run ($N_{moulin} = 2500$). The same figure caption as Figure A3 applies.

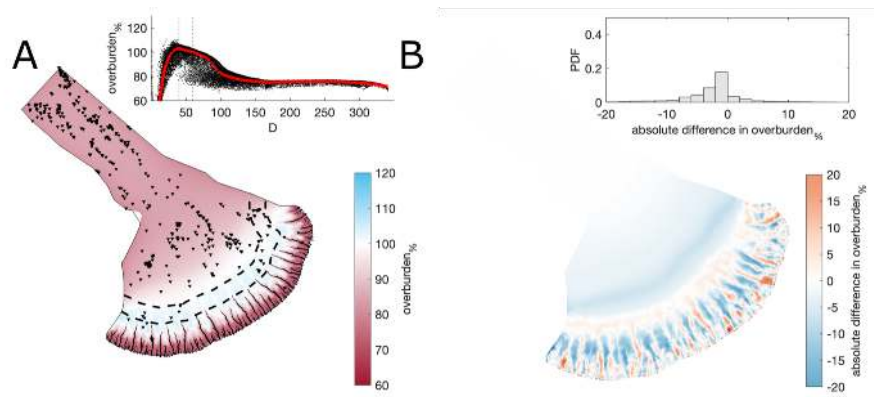


Figure A11. Comparison of the median summer system for where water was directly input at every nodes against the baseline model run ($N_{moulin} = 2500$). The same figure caption as Figure A3 applies.

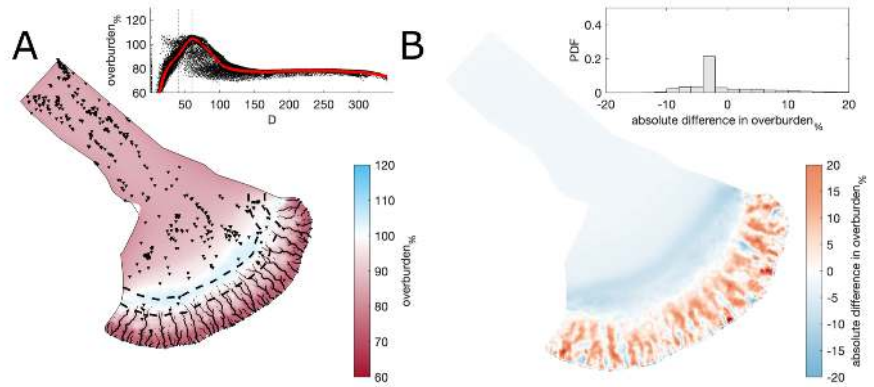


Figure A12. Comparison of the median summer system for a second random distribution of moulin frequency, $N_{moulin} = 2500$ against the baseline model run ($N_{moulin} = 2500$). The same figure caption as Figure A3 applies.

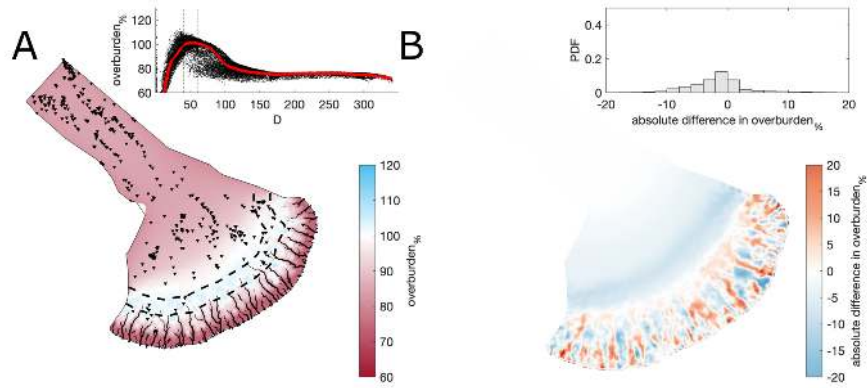


Figure A13. Comparison of the median summer system for a third random distribution of moulin frequency, $N_{moulin} = 2500$ against the baseline model run ($N_{moulin} = 2500$). The same figure caption as Figure A3 applies.

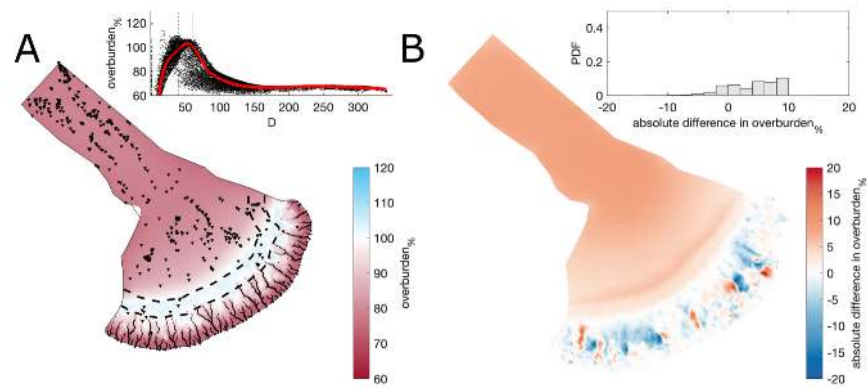


Figure A14. Comparison of the median summer system for basal melt rate, $b_{melt} = 1 \times 10^{-3} \text{ m yr}^{-1}$ against the baseline model run ($b_{melt} = 1 \times 10^{-3} \text{ m yr}^{-1}$). The same figure caption as Figure A3 applies.

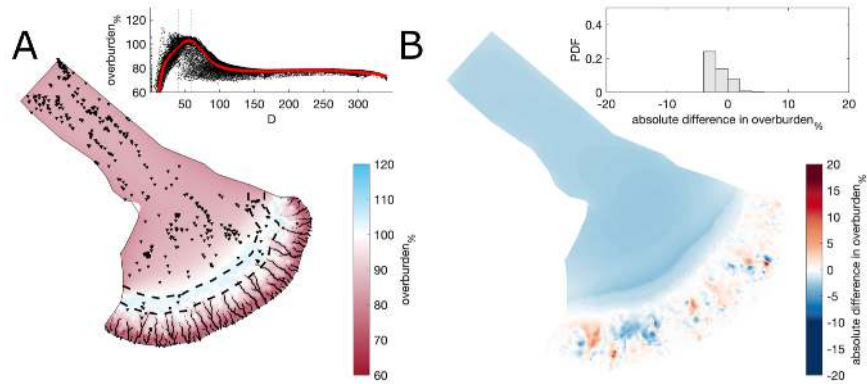


Figure A15. Comparison of the median summer system for basal melt rate, $b_{melt} = 1 \times 10^{-3} \text{ m yr}^{-1}$ against the baseline model run ($b_{melt} = 7 \times 10^{-3} \text{ m yr}^{-1}$). The same figure caption as Figure A3 applies.

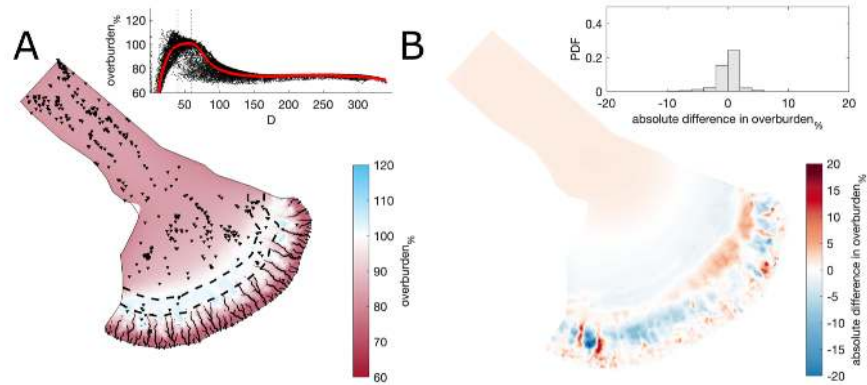


Figure A16. Comparison of the median summer system for basal bump height, $h_r = 0.1 \text{ m}$ against the baseline model run ($h_r = 0.085 \text{ m}$). The same figure caption as Figure A3 applies.

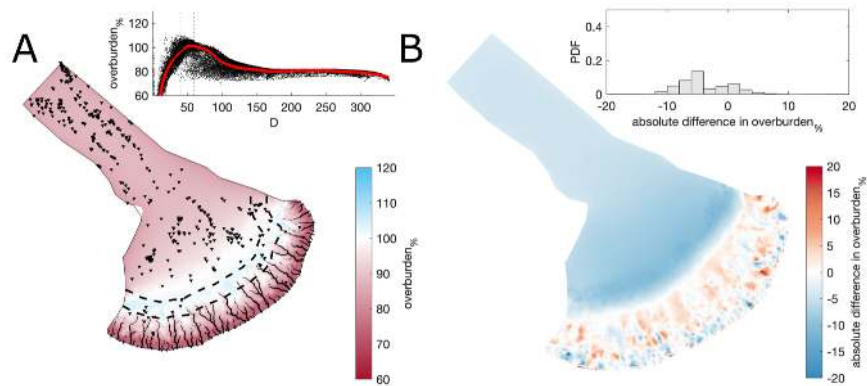


Figure A17. Comparison of the median summer system for basal bump height, $h_r = 0.05$ m against the baseline model run ($h_r = 0.085$ m). The same figure caption as Figure A3 applies.

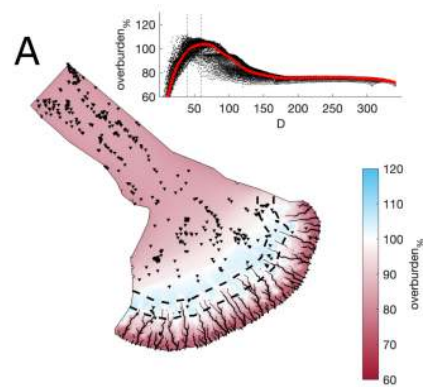


Figure A18. Comparison of a mesh that is not refined with respect to elevation against the baseline model run. The same figure caption as Figure A3 applies.

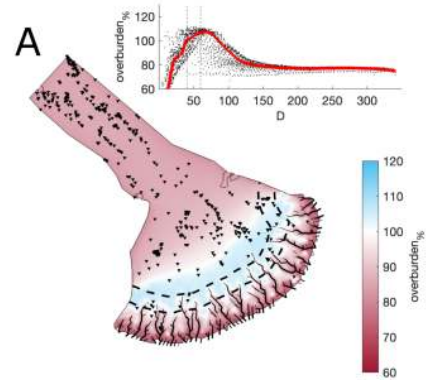


Figure A19. Comparison of a coarser mesh (edge length ~ 5 km) against the baseline model run. The same figure caption as Figure A3 applies.

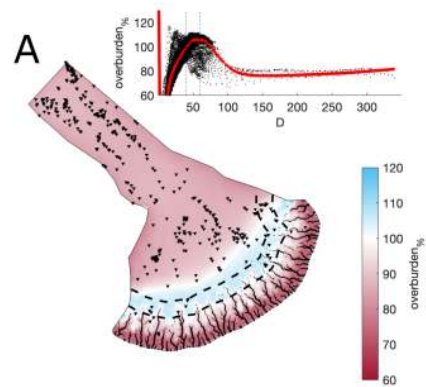


Figure A20. Comparison of a refined mesh (minimum edge length ≈ 300 m) < 80 km from the ice margin against the baseline model run. The same figure caption as Figure A3 applies.

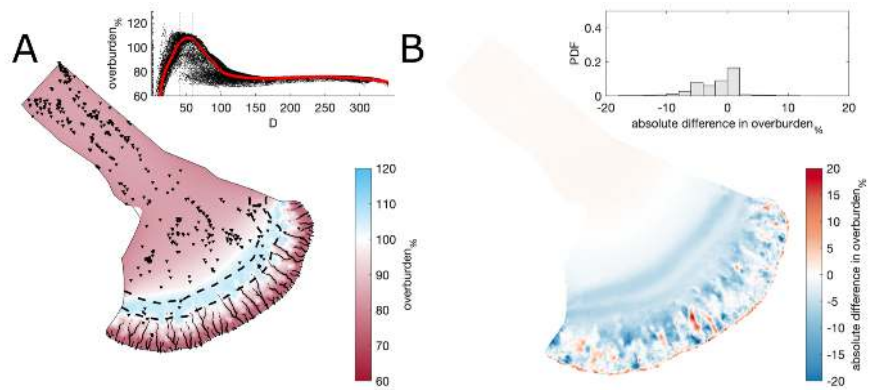


Figure A21. Comparison of a flat bed against the baseline model run. The same figure caption as Figure A3 applies.



Figure A22. Comparison of a modern mesh (without subtracting Quaternary sediment thickness) against the baseline model run. The same figure caption as Figure A3 applies.

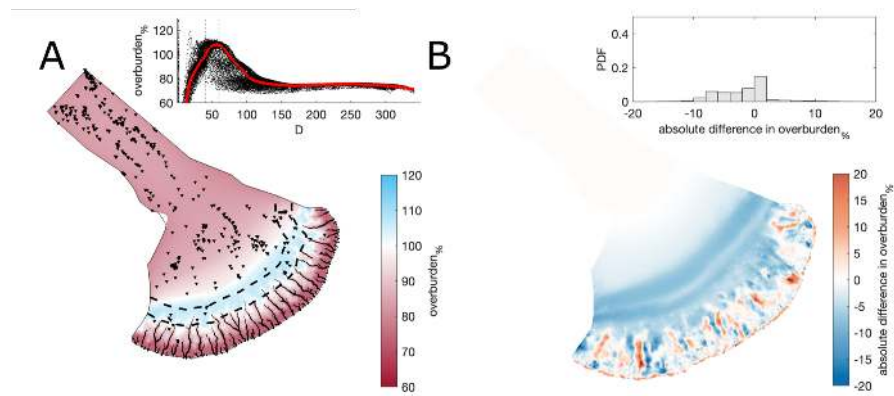


Figure A23. Comparison including lake bathymetry against the baseline model run. The same figure caption as Figure A3 applies.

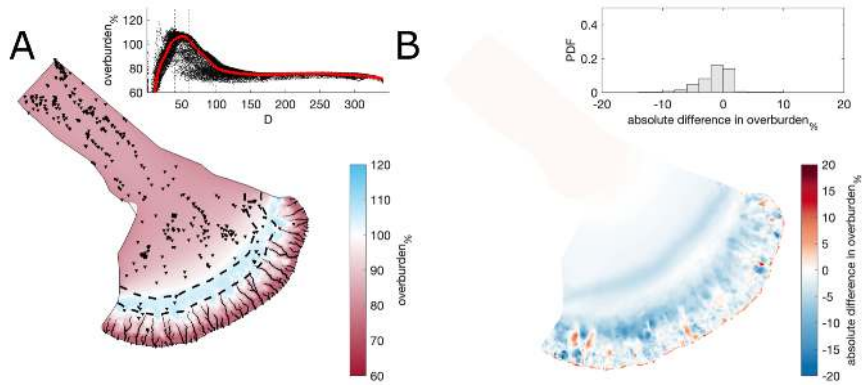


Figure A24. Comparison of a 30 m deep water body at the ice margin boundary against the baseline model run (land-terminating). The same figure caption as Figure A3 applies.

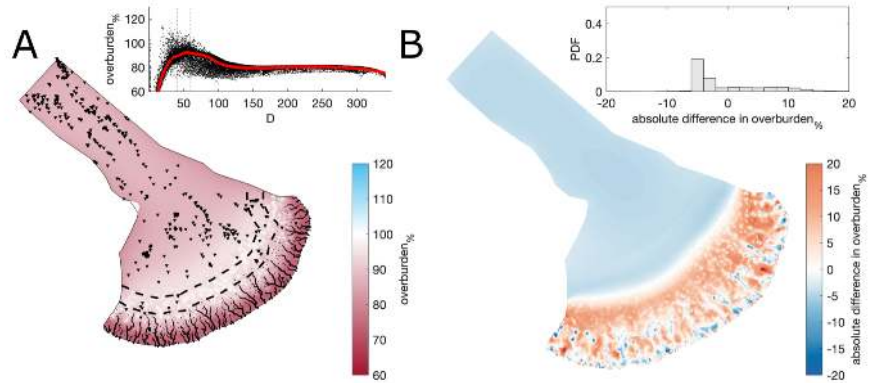


Figure A25. Comparison of the median summer system for an englacial void ratio, $E_{vr} = 10^{-3}$ against the baseline model run ($E_{vr} = 10^{-4}$). The same figure caption as Figure A3 applies.

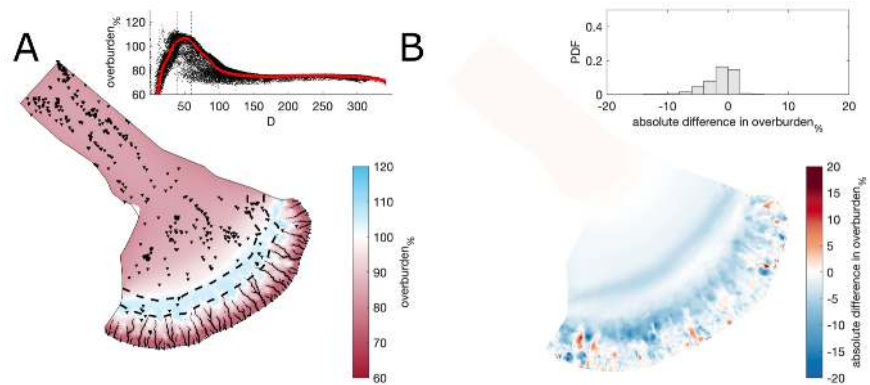


Figure A26. Comparison of the median summer system for an englacial void ratio, $E_{vr} = 10^{-5}$ against the baseline model run ($E_{vr} = 10^{-4}$). The same figure caption as Figure A3 applies.

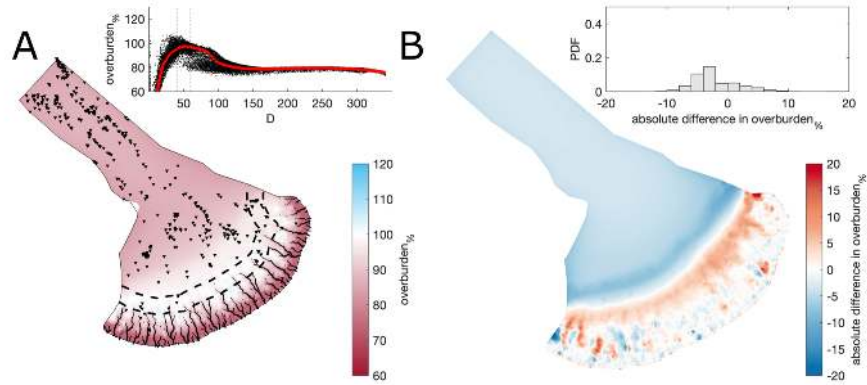


Figure A27. Comparison of the median summer system for a fixed velocity, $U_b = 100 \text{ m yr}^{-1}$ against the baseline model run ($U_b = 150 \text{ m yr}^{-1}$). The same figure caption as Figure A3 applies.

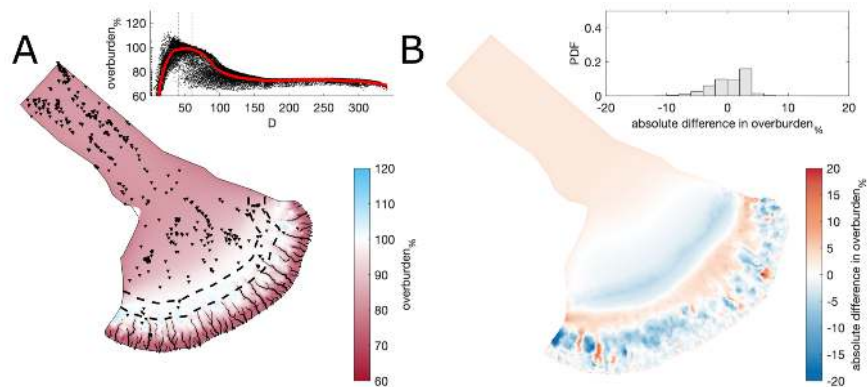


Figure A28. Comparison of the median summer system for a fixed velocity, $U_b = 200 \text{ m yr}^{-1}$ against the baseline model run ($U_b = 150 \text{ m yr}^{-1}$). The same figure caption as Figure A3 applies.

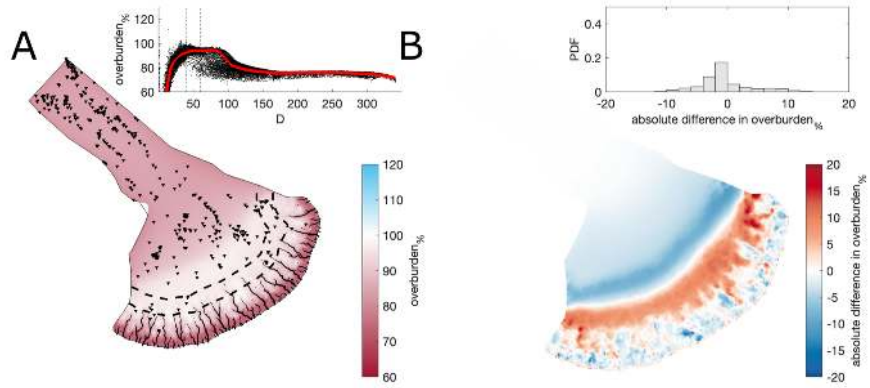


Figure A29. Comparison of the median summer system for a transient velocity, U_b with a median $U_b = 150 \text{ m yr}^{-1}$ against the fixed baseline model run ($U_b = 150 \text{ m yr}^{-1}$). The same figure caption as Figure A3 applies.

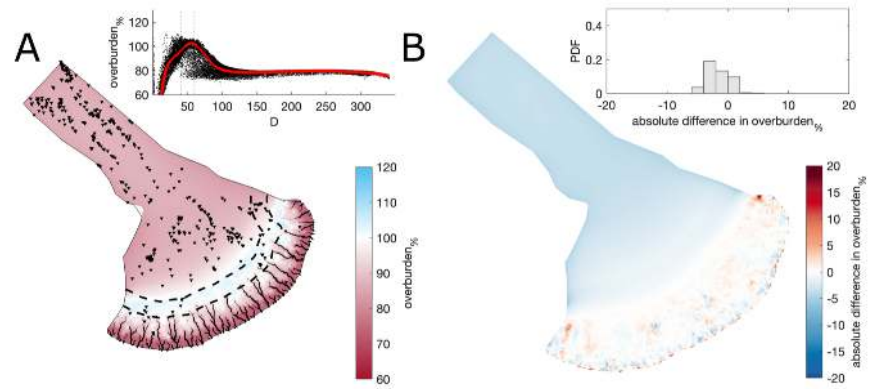


Figure A30. Comparison of the median summer system for a transient velocity, U_b with a median $U_b = 100 \text{ m yr}^{-1}$ against the fixed baseline model run ($U_b = 150 \text{ m yr}^{-1}$). The same figure caption as Figure A3 applies.

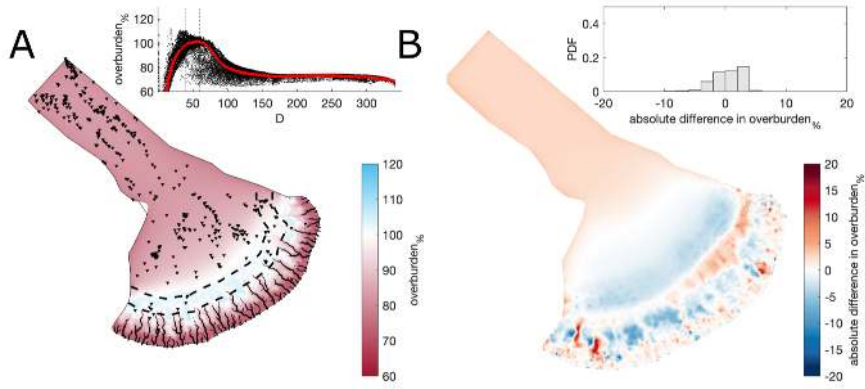


Figure A31. Comparison of the median summer system for a transient velocity, U_b with a median $U_b = 200 \text{ m yr}^{-1}$ against the fixed baseline model run ($U_b = 150 \text{ m yr}^{-1}$). The same figure caption as Figure A3 applies.

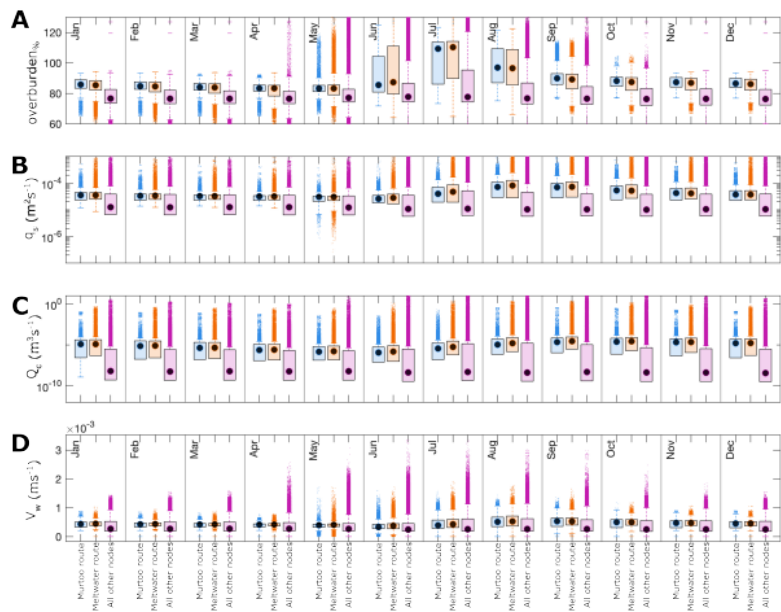


Figure A32. Boxplots of model parameters grouped by month for overburden (overburden%, **A**), sheet discharge (q_s , **B**), water velocity (V_w , **C**), and channel discharge (Q_c , **D**) during all model years at nodes between 40–60 km from the ice margin. As in Figure 5, nodes that fall within meltwater routes which do host murtoos (Murtoo free MRs) are shown in blue, nodes which fall within mapped meltwater routes that do not contain murtoos (Murtoo hosting MRs) are shown in orange, and all other nodes are shown in purple. Medians for each group are shown as black circles, and ‘outliers’—defined as points more than 150% of the interquartile range away from the upper and lower quartile—are shown as crosses.

Table A1. Tukey-Kramer HSD test of ~~overburden%~~ overburden% in meltwater routes, murtoo routes, and non-meltwater routes between 40–60 km from the ice margin. The upper and lower limits describe the 95% confidence intervals for the true mean difference, A-B is the difference between group means.

Month	Group A	Group B	Lower Limit	A-B	Upper limit	P-Value
January	meltwater route	murtoo route	-1.71	-1.30	-0.89	0.00
	non meltwater route <ins>all other nodes</ins>	murtoo route	-10.49	-10.12	-9.75	0.00
February	meltwater route	non meltwater route <ins>all other nodes</ins>	8.58	8.82	9.06	0.00
	non meltwater route <ins>all other nodes</ins>	murtoo route	-9.87	-9.50	-9.12	0.00
March	meltwater route	murtoo route	-1.58	-1.17	-0.76	0.00
	non meltwater route <ins>all other nodes</ins>	murtoo route	-9.30	-8.93	-8.55	0.00
	meltwater route	non meltwater route <ins>all other nodes</ins>	7.52	7.75	7.99	0.00
April	meltwater route	murtoo route	-1.55	-1.14	-0.73	0.00
	non meltwater route <ins>all other nodes</ins>	murtoo route	-8.33	-7.96	-7.58	0.00
	meltwater route	non meltwater route <ins>all other nodes</ins>	6.58	6.82	7.06	0.00
May	meltwater route	murtoo route	-1.10	-0.69	-0.28	0.00
	non meltwater route <ins>all other nodes</ins>	murtoo route	-5.26	-4.89	-4.51	0.00
	meltwater route	non meltwater route <ins>all other nodes</ins>	3.96	4.20	4.43	0.00
June	meltwater route	murtoo route	0.70	1.12	1.54	0.00
	non meltwater route <ins>all other nodes</ins>	murtoo route	-8.56	-8.17	-7.79	0.00
	meltwater route	non meltwater route <ins>all other nodes</ins>	9.05	9.30	9.54	0.00
July	meltwater route	murtoo route	0.10	0.52	0.93	0.00
	non meltwater route <ins>all other nodes</ins>	murtoo route	-18.72	-18.34	-17.96	0.00
	meltwater route	non meltwater route <ins>all other nodes</ins>	18.61	18.85	19.10	0.00
August	meltwater route	murtoo route	-2.01	-1.59	-1.18	0.00
	non meltwater route <ins>all other nodes</ins>	murtoo route	-18.81	-18.43	-18.04	0.00
	meltwater route	non meltwater route <ins>all other nodes</ins>	16.59	16.83	17.08	0.00
September	meltwater route	murtoo route	-2.30	-1.88	-1.47	0.00
	non meltwater route <ins>all other nodes</ins>	murtoo route	-14.47	-14.09	-13.71	0.00
	meltwater route	non meltwater route <ins>all other nodes</ins>	11.97	12.21	12.45	0.00
October	meltwater route	murtoo route	-2.14	-1.72	-1.31	0.00
	non meltwater route <ins>all other nodes</ins>	murtoo route	-12.49	-12.11	-11.73	0.00
	meltwater route	non meltwater route <ins>all other nodes</ins>	10.15	10.39	10.63	0.00
November	meltwater route	murtoo route	-1.99	-1.57	-1.15	0.00
	non meltwater route <ins>all other nodes</ins>	murtoo route	-12.06	-11.68	-11.30	0.00
	meltwater route	non meltwater route <ins>all other nodes</ins>	9.87	10.11	10.36	0.00
December	meltwater route	murtoo route	-1.88	-1.46	-1.04	0.00
	non meltwater route <ins>all other nodes</ins>	murtoo route	-11.56	-11.17	-10.79	0.00
	meltwater route	non meltwater route <ins>all other nodes</ins>	9.47	9.72	9.96	0.00

Table A2. Tukey-Kramer HSD test of q_s in meltwater routes, murtoo routes, and non-meltwater routes between 40–60 km from the ice margin. The upper and lower limits describe the 95% confidence intervals for the true mean difference, A-B is the difference between group means.

Month	Group A	Group B	Lower Limit	A-B	Upper limit	P-Value
January	meltwater route	murtoo route	-5.07×10^{-7}	2.89×10^{-6}	6.28×10^{-6}	0.27
	non meltwater route all other nodes	murtoo route	-1.57×10^{-5}	-1.26×10^{-5}	-9.54×10^{-7}	0.00
February	meltwater route	non meltwater route all other nodes	1.36×10^{-5}	1.55×10^{-5}	1.75×10^{-5}	0.00
	non meltwater route all other nodes	murtoo route	-1.23×10^{-6}	2.19×10^{-6}	5.6×10^{-6}	0.88
March	meltwater route	murtoo route	-1.39×10^{-5}	-1.08×10^{-5}	-7.69×10^{-6}	0.00
	non meltwater route all other nodes	non meltwater route all other nodes	1.1×10^{-5}	1.3×10^{-5}	1.5×10^{-5}	0.00
April	meltwater route	murtoo route	-2.05×10^{-6}	1.36×10^{-6}	4.77×10^{-6}	0.99
	non meltwater route all other nodes	murtoo route	-1.26×10^{-5}	-9.49×10^{-6}	-6.37×10^{-6}	0.00
May	meltwater route	non meltwater route all other nodes	8.86×10^{-6}	1.08×10^{-5}	1.28×10^{-5}	0.00
	non meltwater route all other nodes	murtoo route	-2.66×10^{-6}	7.6×10^{-7}	4.18×10^{-6}	0.99
June	meltwater route	murtoo route	-1.14×10^{-5}	-8.28×10^{-6}	-5.15×10^{-6}	0.00
	non meltwater route all other nodes	non meltwater route all other nodes	7.05×10^{-6}	9.04×10^{-6}	1.10×10^{-5}	0.00
July	meltwater route	murtoo route	-2.92×10^{-6}	4.99×10^{-7}	3.92×10^{-6}	0.99
	non meltwater route all other nodes	murtoo route	-7.11×10^{-6}	-3.98×10^{-6}	-8.53×10^{-5}	0.00
August	meltwater route	non meltwater route all other nodes	2.49×10^{-6}	4.48×10^{-6}	6.47×10^{-6}	0.00
	non meltwater route all other nodes	murtoo route	9.57×10^{-7}	4.46×10^{-6}	7.97×10^{-6}	0.00
September	meltwater route	murtoo route	6.04×10^{-6}	9.25×10^{-6}	1.25×10^{-5}	0.00
	non meltwater route all other nodes	non meltwater route all other nodes	-6.83×10^{-6}	-4.79×10^{-6}	-2.75×10^{-6}	0.00
October	meltwater route	murtoo route	1.36×10^{-5}	1.7×10^{-5}	2.05×10^{-5}	0.00
	non meltwater route all other nodes	murtoo route	9.95×10^{-6}	1.31×10^{-5}	1.63×10^{-5}	0.00
November	meltwater route	non meltwater route all other nodes	1.89×10^{-6}	3.9×10^{-6}	5.91×10^{-6}	0.00
	non meltwater route all other nodes	murtoo route	1.82×10^{-5}	2.17×10^{-5}	2.52×10^{-5}	0.00
December	meltwater route	murtoo route	-9.99×10^{-6}	-6.79×10^{-6}	-3.59×10^{-6}	0.00
	non meltwater route all other nodes	non meltwater route all other nodes	2.65×10^{-5}	2.85×10^{-5}	3.05×10^{-5}	0.00
	meltwater route	murtoo route	1.06×10^{-5}	1.41×10^{-5}	1.75×10^{-5}	0.00
	non meltwater route all other nodes	murtoo route	-2.33×10^{-5}	-2.02×10^{-5}	1.7×10^{-5}	0.00
	meltwater route	non meltwater route all other nodes	3.22×10^{-5}	3.42×10^{-5}	3.62×10^{-5}	0.00
	non meltwater route all other nodes	murtoo route	5.67×10^{-6}	9.15×10^{-6}	1.26×10^{-5}	0.00
	meltwater route	murtoo route	-2.44×10^{-5}	-2.12×10^{-5}	-1.8×10^{-5}	0.00
	non meltwater route all other nodes	non meltwater route all other nodes	2.84×10^{-5}	3.04×10^{-5}	3.24×10^{-5}	0.00
	meltwater route	murtoo route	2.52×10^{-6}	6×10^{-6}	9.48×10^{-6}	0.00
	non meltwater route all other nodes	murtoo route	-2.14×10^{-5}	-1.82×10^{-5}	-1.50×10^{-5}	0.00
	meltwater route	non meltwater route all other nodes	2.22×10^{-5}	2.42×10^{-5}	2.62×10^{-5}	0.00
	non meltwater route all other nodes	murtoo route	7.23×10^{-7}	4.22×10^{-6}	7.71×10^{-6}	0.00
	meltwater route	murtoo route	-1.87×10^{-5}	-1.55×10^{-5}	1.23×10^{-5}	0.00
	non meltwater route all other nodes	non meltwater route all other nodes	1.77×10^{-5}	1.97×10^{-5}	2.18×10^{-5}	0.00

Table A3. Tukey-Kramer HSD test of Q_c in meltwater routes, murtoo routes, and non-meltwater routes between 40–60 km from the ice margin. The upper and lower limits describe the 95% confidence intervals for the true mean difference, A-B is the difference between group means.

Month	Group A	Group B	Lower Limit	A-B	Upper limit	P-Value
January	meltwater route	murtoo route	-7.57×10^{-3}	6.51×10^{-4}	8.87×10^{-3}	0.99
	non-meltwater route <u>all other nodes</u>	murtoo route	-6.19×10^{-3}	1.34×10^{-3}	8.86×10^{-3}	0.99
February	meltwater route	non-meltwater route <u>all other nodes</u>	-5.47×10^{-3}	-6.86×10^{-4}	4.1×10^{-3}	0.99
	non-meltwater route <u>all other nodes</u>	murtoo route	-7.78×10^{-3}	5.08×10^{-4}	8.79×10^{-3}	0.99
March	meltwater route	murtoo route	-6.72×10^{-3}	5.08×10^{-4}	8.44×10^{-3}	0.99
	non-meltwater route <u>all other nodes</u>	non-meltwater route <u>all other nodes</u>	-5.18×10^{-3}	-3.53×10^{-4}	4.47×10^{-3}	0.99
April	meltwater route	murtoo route	-7.86×10^{-3}	4.06×10^{-4}	8.677×10^{-3}	0.99
	non-meltwater route <u>all other nodes</u>	murtoo route	-6.93×10^{-3}	6.3×10^{-4}	8.19×10^{-3}	0.99
May	meltwater route	non-meltwater route <u>all other nodes</u>	-5.04×10^{-3}	-2.24×10^{-4}	4.59×10^{-5}	0.99
	non-meltwater route <u>all other nodes</u>	murtoo route	-7.98×10^{-3}	3.07×10^{-4}	8.59×10^{-3}	0.99
June	meltwater route	murtoo route	-7.10×10^{-3}	4.83×10^{-4}	8.06×10^{-3}	0.99
	non-meltwater route <u>all other nodes</u>	non-meltwater route <u>all other nodes</u>	-5×10^{-3}	-1.76×10^{-4}	4.65×10^{-3}	0.99
July	meltwater route	murtoo route	-8.02×10^{-3}	2.60×10^{-4}	8.54×10^{-3}	0.99
	non-meltwater route <u>all other nodes</u>	murtoo route	-5.58×10^{-3}	2.01×10^{-3}	9.59×10^{-3}	0.99
August	meltwater route	non-meltwater route <u>all other nodes</u>	-6.57×10^{-3}	-1.75×10^{-3}	3.08×10^{-3}	0.99
	non-meltwater route <u>all other nodes</u>	murtoo route	-7.93×10^{-3}	5.65×10^{-4}	9.06×10^{-3}	0.99
September	meltwater route	murtoo route	7.28×10^{-3}	1.51×10^{-2}	2.28×10^{-2}	0.00
	non-meltwater route <u>all other nodes</u>	non-meltwater route <u>all other nodes</u>	-1.94×10^{-2}	-1.45×10^{-2}	-9.54×10^{-3}	0.00
October	meltwater route	murtoo route	-6.22×10^{-3}	2.14×10^{-3}	1.05×10^{-2}	0.99
	non-meltwater route <u>all other nodes</u>	murtoo route	3.20×10^{-2}	3.97×10^{-2}	4.73×10^{-2}	0.00
November	meltwater route	non-meltwater route <u>all other nodes</u>	-4.24×10^{-2}	-3.75×10^{-2}	-3.27×10^{-2}	0.00
	non-meltwater route <u>all other nodes</u>	murtoo route	-4.45×10^{-3}	4.02×10^{-3}	1.25×10^{-2}	0.99
December	meltwater route	murtoo route	3.97×10^{-2}	4.74×10^{-2}	5.52×10^{-2}	0.00
	non-meltwater route <u>all other nodes</u>	non-meltwater route <u>all other nodes</u>	-4.84×10^{-2}	-4.34×10^{-2}	-3.85×10^{-2}	0.00
	meltwater route	murtoo route	-4.64×10^{-3}	3.75×10^{-3}	1.21×10^{-2}	0.99
	non-meltwater route <u>all other nodes</u>	murtoo route	2.24×10^{-2}	3.01×10^{-2}	3.78×10^{-2}	0.00
	meltwater route	non-meltwater route <u>all other nodes</u>	-3.12×10^{-2}	-2.63×10^{-2}	-2.15×10^{-2}	0.00
	non-meltwater route <u>all other nodes</u>	murtoo route	-6.24×10^{-3}	2.19×10^{-3}	1.06×10^{-2}	0.99
	meltwater route	murtoo route	2.22×10^{-3}	9.94×10^{-3}	1.77×10^{-2}	0.00
	non-meltwater route <u>all other nodes</u>	non-meltwater route <u>all other nodes</u>	-1.27×10^{-2}	-7.75×10^{-3}	-2.84×10^{-3}	0.00
	meltwater route	murtoo route	-7.16×10^{-3}	1.27×10^{-3}	9.70×10^{-3}	0.99
	non-meltwater route <u>all other nodes</u>	murtoo route	-4.08×10^{-3}	3.63×10^{-3}	1.13×10^{-2}	0.99
	meltwater route	non-meltwater route <u>all other nodes</u>	-7.27×10^{-3}	-2.36×10^{-3}	2.55×10^{-3}	0.99
	non-meltwater route <u>all other nodes</u>	murtoo route	-7.56×10^{-3}	9.10×10^{-4}	9.38×10^{-3}	0.99
	meltwater route	murtoo route	-5.57×10^{-3}	2.18×10^{-3}	9.94×10^{-3}	0.99
	non-meltwater route <u>all other nodes</u>	non-meltwater route <u>all other nodes</u>	-6.21×10^{-3}	-1.27×10^{-3}	3.66×10^{-3}	0.99

Table A4. Tukey-Kramer HSD test of V_W in meltwater routes, murtoo routes, and non-meltwater routes between 40–60 km from the ice margin. The upper and lower limits describe the 95% confidence intervals for the true mean difference, A-B is the difference between group means.

Month	Group A	Group B	Lower Limit	A-B	Upper limit	P-Value
January	meltwater route	murtoo route	1.41×10^{-6}	7.42×10^{-6}	1.34×10^{-5}	0.00
	non meltwater route <u>all other nodes</u>	murtoo route	-5.63×10^{-5}	-5.08×10^{-5}	-4.53×10^{-5}	0.00
February	meltwater route	non meltwater route <u>all other nodes</u>	5.47×10^{-5}	5.82×10^{-5}	6.17×10^{-5}	0.00
	non meltwater route <u>all other nodes</u>	murtoo route	1.11×10^{-6}	7.17×10^{-6}	1.32×10^{-5}	0.00
March	meltwater route	murtoo route	-4.63×10^{-5}	-4.08×10^{-5}	-3.53×10^{-5}	0.00
	non meltwater route <u>all other nodes</u>	non meltwater route <u>all other nodes</u>	4.44×10^{-5}	4.80×10^{-5}	5.15×10^{-5}	0.00
April	meltwater route	murtoo route	7.90×10^{-7}	6.83×10^{-6}	1.29×10^{-5}	0.01
	non meltwater route <u>all other nodes</u>	murtoo route	-3.88×10^{-5}	-3.32×10^{-5}	-2.77×10^{-5}	0.00
May	meltwater route	non meltwater route <u>all other nodes</u>	3.65×10^{-5}	4.01×10^{-5}	4.36×10^{-5}	0.00
	non meltwater route <u>all other nodes</u>	murtoo route	1.06×10^{-6}	7.11×10^{-6}	1.32×10^{-5}	0.00
June	meltwater route	murtoo route	-3.26×10^{-5}	-2.71×10^{-5}	-2.16×10^{-5}	0.00
	non meltwater route <u>all other nodes</u>	non meltwater route <u>all other nodes</u>	3.07×10^{-5}	3.42×10^{-5}	3.77×10^{-5}	0.00
July	meltwater route	murtoo route	1.73×10^{-6}	7.78×10^{-6}	1.38×10^{-5}	0.00
	non meltwater route <u>all other nodes</u>	murtoo route	-6.47×10^{-6}	-9.33×10^{-7}	4.61×10^{-6}	1.00
August	meltwater route	non meltwater route <u>all other nodes</u>	5.19×10^{-6}	8.72×10^{-6}	1.22×10^{-5}	0.00
	non meltwater route <u>all other nodes</u>	murtoo route	1.22×10^{-5}	1.84×10^{-5}	2.46×10^{-5}	0.00
September	meltwater route	murtoo route	4.12×10^{-5}	4.69×10^{-5}	5.26×10^{-5}	0.00
	non meltwater route <u>all other nodes</u>	non meltwater route <u>all other nodes</u>	-3.21×10^{-5}	-2.85×10^{-5}	-2.48×10^{-5}	0.00
October	meltwater route	murtoo route	2.47×10^{-5}	3.09×10^{-5}	3.70×10^{-5}	0.00
	non meltwater route <u>all other nodes</u>	murtoo route	7.34×10^{-7}	6.33×10^{-6}	1.19×10^{-5}	0.01
November	meltwater route	non meltwater route <u>all other nodes</u>	2.10×10^{-5}	2.45×10^{-5}	2.81×10^{-5}	0.00
	non meltwater route <u>all other nodes</u>	murtoo route	1.46×10^{-5}	2.08×10^{-5}	2.70×10^{-5}	0.00
December	meltwater route	murtoo route	-1.05×10^{-4}	-9.90×10^{-5}	-9.34×10^{-5}	0.00
	non meltwater route <u>all other nodes</u>	non meltwater route <u>all other nodes</u>	1.16×10^{-4}	1.20×10^{-4}	1.23×10^{-4}	0.00
	meltwater route	murtoo route	2.52×10^{-6}	8.65×10^{-6}	1.48×10^{-5}	0.00
	non meltwater route <u>all other nodes</u>	murtoo route	-1.19×10^{-4}	-1.14×10^{-4}	-1.08×10^{-4}	0.00
	meltwater route	non meltwater route <u>all other nodes</u>	1.19×10^{-4}	1.22×10^{-4}	1.26×10^{-4}	0.00
	non meltwater route <u>all other nodes</u>	murtoo route	8.15×10^{-6}	1.43×10^{-5}	2.05×10^{-5}	0.00
	meltwater route	murtoo route	-9.90×10^{-5}	-9.34×10^{-5}	-8.77×10^{-5}	0.00
	non meltwater route <u>all other nodes</u>	non meltwater route <u>all other nodes</u>	1.04×10^{-4}	1.08×10^{-4}	1.11×10^{-4}	0.00
	meltwater route	murtoo route	6.68×10^{-6}	1.28×10^{-5}	1.90×10^{-5}	0.00
	non meltwater route <u>all other nodes</u>	murtoo route	-8.03×10^{-5}	-7.46×10^{-5}	-6.90×10^{-5}	0.00
	meltwater route	non meltwater route <u>all other nodes</u>	8.39×10^{-5}	8.75×10^{-5}	9.10×10^{-5}	0.00
	non meltwater route <u>all other nodes</u>	murtoo route	3.95×10^{-6}	1.01×10^{-5}	1.63×10^{-5}	0.00
	meltwater route	murtoo route	-6.79×10^{-5}	-6.22×10^{-5}	-5.65×10^{-5}	0.00
	non meltwater route <u>all other nodes</u>	non meltwater route <u>all other nodes</u>	6.87×10^{-5}	7.23×10^{-5}	7.59×10^{-5}	0.00